High Temperature and Pressure Measurements from TDLAS Through the Application of 2nd Derivative Fitting and the Aggregate Boltzmann Method

by

Jacob France

A dissertation submitted in partial fulfillment
of the requirements for the degree of
Doctor of Philosophy
(Aerospace Engineering)
in The University of Michigan
2019

Doctoral Committee:

Associate Professor Mirko Gamba, Chair
Professor James Driscoll
Professor John Foster
Assistant Professor Benjamin Jorns

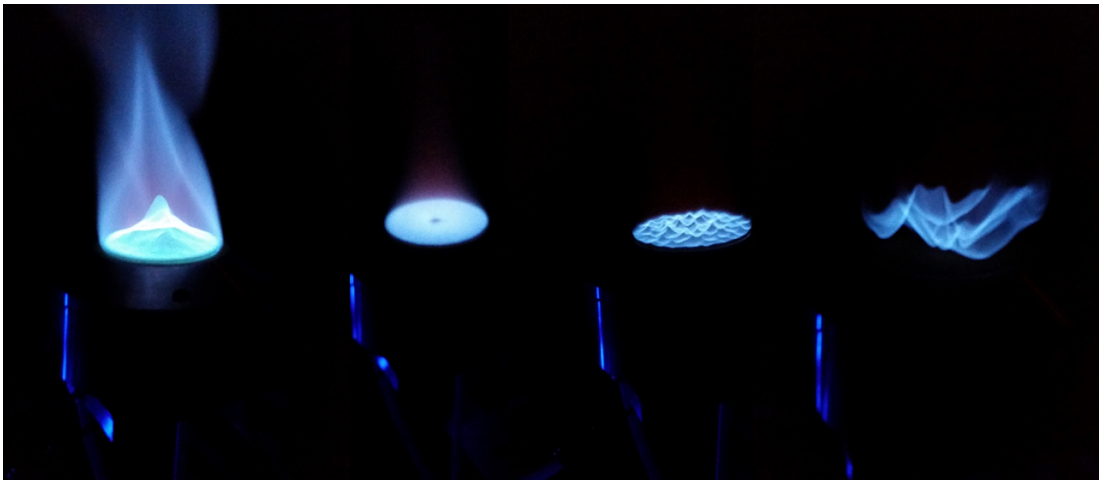

Jacob J. France

jjfrance@umich.edu

ORCID iD: 0000-0002-5753-739X

© Jacob J. France 2019

To my family and friends, both here and gone, who have helped me along the way.

ACKNOWLEDGEMENTS

This dissertation, and all the work leading up to it, would not have been possible without the help and guidance of countless people throughout my life. I would like to extend my gratitude to my advisor, Professor Mirko Gamba, who took a chance and offered me a position in his lab. He has guided me throughout my time here at Michigan, mentoring me, teaching me, and helping me learn not only about aerospace, but also what it means to be a researcher. I would not have made it through this trial without your help. I would also like to thank my committee members, Professor James Driscoll, Professor John Foster, and Professor Benjamin Jorns, for your input and questions, which helped me to focus this dissertation and make it the best that I could. Thank you for your time and help in this process.

The students and researchers would not be able to function without the assistance and efforts of the office and technical staff present at this University. Thank you to Denise Phelps, who kept me sane, up to date, and helped with any question that I might have had. Thank you to Linda Weiss, who was a great help in organizing my efforts in booking rooms for prelims, office hours, and meetings, and who helped keep my review sessions well attended through the organization of food and soft drinks. Thanks to Terry Larrow for his ceaseless help in both flawless producing my project pieces and his input on how to make them better, to Aaron Borgman for helping with the countless electrical systems questions and pieces I had, to Chris Chartier for the assistance in the laboratories, to David McLean for keeping my computer up and running through several research crippling systems crashes, to Thomas Griffin

for help with anything technical related at all, both in and out of the lab, and to the late Martin Stenzel, for helping me mount the infrastructure to make my experiments possible. My work would not have been completed without all of your help.

I would also like to thank the researchers at AFRL, who took me in on the AFOSR SFFP and worked with me throughout my time here at Michigan. Your guidance and mentoring have helped me to advance both my understanding of research outside of academia as well as futhering my technical understanding of laser diagnostics. Thank you to Dr. Chiping Li, the technical monitor for my NDSEG fellowship, who helped fund my project and allowed me to continue to work here at the University.

To all my friends that have helped in innumerable ways both in the lab and outside of it, I offer my sincerest thanks. Thank you to my office mates, Yasin Abul-Huda, Fabian Chacon, Andrew Caswell, and James Duvall, thanks for all the help over the years. To The rest of my lab, Robin Hunt, Abhinav Dasari, Logan White, Rohan Morajkar, Louis Edelman and Alex Feleo, thank you all for making my time here more enjoyable and I wish you all the best. For the rest of my FXB friends and their SOs, Chukwuka Mbagwu, Yukiko Shimizu, Kai Ding, Lauren Mackey Astrid Raisanen, Chris Marley, Jose Munoz, Nicholas Arnold-Medabalimi, Samuel Chen, Devina Sanjaya, Brittany Essink, Krystal Acosta, Christopher Wentland, Ayoub Gouasmi, Frans and Margeaux Ebersohn, Tim and Amalie Collard, and any others I may have missed, thank you all for making my time at the University of Michigan a great one. Lastly to my other assorted Michigan friends, Andrew Nalepa, Patrick and Melissa Carrol, Evan Hilgemann, Kirsten Hansen, and Emmamarie Haasl, thank you all for supporting me throughout my time here. I am fortunate to have met you all and I would have starved and/or gone insane long ago without all of your help. From bouncing research ideas off of, to the barbeques and game nights, to forcing me to eat whenever I had a deadline coming up, to letting me vent when things were heading south, without your help, I can confidently say I would not have made it through

this. Thank you all for making this time here not only fruitful, but fun as well.

To my girlfriend, Iris Vipperman, and her family, Sally and Robert Vipperman and Nicholas and Eileen Vipperman. Thank you for being there for me in my time away from my own family. From holidays, to birthdays, from weddings o simple dinners, you have been a surrogate family here in Michigan. Thank you for being there for me, supporting me, and loving me in my time here.

Lastly, I would like to thank my family, without whose constant support I would not have even made it to Michigan, much less completed my PhD. To my parents, Damian and Tanya France, who raised me, supported me, and loved me, teaching me not only to work hard and strive for excellence, but also the value in enjoying life and having fun. Thank you for allowing me to learn and supporting me in all of my efforts. I would not be where I am, or who I am today were it not for you. Thank you to my siblings, Jared, Sarah and Joshua France, who provided support, encouragement, and entertainment throughout. Even when we are all in different states, y'all are always up to hang out online and visit and laugh. Thank you for being there for me. To my grandparents, both here and gone, thank you for everything. I am truly grateful for the time and love you have shown me. You always believed in me, without fail. Lastly, to all my aunts, uncles and cousins, who always are there for me, welcome me when I come home to visit, and are genuinely interested in how my life is going. I am truly grateful to have a family who sticks together, loves each other, and cares as much as you all do. Thank you for everything.

Without all of your contributions this work would never have been completed. I owe each and every one of you a great debt, one which I can never truly repay. you have helped me accomplish my childhood dream, a rare gift, one which not many people are lucky enough to have the opportunity to obtain. Thank you for your time, effort, and generosity.

TABLE OF CONTENTS

DEDICATION ii

ACKNOWLEDGEMENTS iii

LIST OF FIGURES ix

LIST OF TABLES xvii

LIST OF APPENDICES xix

ABSTRACT xx

CHAPTER

I. Introduction and Background 1

1.1 Motivation 2
1.2 Overview of Tunable Diode Laser Absorption Spectroscopy 3
1.3 Lineshape Functions 7
1.3.1 Gaussian Lineshape Function 7
1.3.2 Lorentzian Lineshape Function 8
1.3.3 Voigt Lishape Function 9
1.4 Wavelength Centerline Shifting 10
1.4.1 Doppler Shifting 11
1.5 Pressure Shifting 12
1.6 Common TDLAS Data Acquisition Techniques and Processing Methods 13
1.6.1 Fixed Wavelength Direct Absorption Spectroscopy . 13
1.6.2 Scanned Wavelength Direct Absorption Spectroscopy 15
1.6.3 Wavelength Modulation Spectroscopy 25
1.7 Gaps in the Current Knowledge 27
1.8 Thesis Objectives and Novel Contributions 31

II. Description of a Linear Array Camera for Planar Absorption Measurements 37

2.1 Linear Array Camera 37
2.2 The LAC Optical Setup and Operation 38
2.3 Common Problems and Corrections with the LAC 42
2.3.1 Etalon Interference 42
2.3.2 Vibrational Noise 48
2.3.3 Beamsteering 55
2.3.4 Experimental Setup 57
2.4 Demonstration Measurements 58
2.4.1 Statistics on Corrections 59
2.5 Structural Vibrational Analysis 66
2.6 LAC Conclusions 70

III. Baseline Error Rejection through Second Derivative Curve Fitting 71

3.1 Baseline Measurement Experiments 72
3.2 Comparison of Second Derivative Spectroscopy with WMS 73
3.3 Effects of Baseline Errors 75
3.4 Analysis of Highly Resolved 2nd Derivative Spectroscopy . . . 77
3.5 Demonstration Experiments 81
3.5.1 Low Pressure Validation Experimental Setup 81
3.5.2 Low Pressure Cell Data 82
3.5.3 Low Pressure Cell Conclusions 85
3.5.4 McKenna Flat Flame Burner Experimental Setup . 85
3.5.5 McKenna Flat Flame Burner Conclusions 88
3.6 Line Selection 89
3.7 Second Derivative Fitting Conclusions 91

IV. Extension of the Boltzmann Plot Method for Application with Blended Spectra 92

4.1 The Boltzmann Plot Equations 93
4.2 The Modified Equations 95
4.3 Algorithm of the Aggregate Boltzmann Plot Method 97
4.4 Sensitivity and Error Analysis 100
4.4.1 Formulation 100
4.4.2 Monte Carlo Analysis 106
4.5 Low Pressure Cell Measurements 108
4.6 McKenna Burner Measurements 112
4.7 Aggregate Line Selections 114
4.7.1 Aggregate Line Selection Theory 114

4.7.2 Aggregate Line Selection Results 116
4.7.3 Low Pressure Cell 116
4.7.4 McKenna Burner 120

V. A Robust Sensing Technique Combining Second Derivative Fitting and the Aggregate Boltzmann Plot Method 124

5.1 Description of the Algorithm 125
5.2 Low Pressure Cell Validation 127
5.3 Improvements over the Individual Methods Over the McKenna Flat Flame Burner 129
5.4 Conclusions 136

VI. Conclusions and Future Work 138

6.1 Conclusions 138
6.1.1 The LAC Description and Analysis 138
6.1.2 Second Derivative Fitting and the Aggregate Boltzmann Plot Method 140
6.1.3 The Robust Combination Algorithm of the Second Derivative Fitting Method and the Aggregate Boltzmann Plot Method 143
6.2 Future Work 144
6.2.1 The LAC 144
6.2.2 Second Derivative Fitting Method 145
6.2.3 The Aggregate Boltzmann Plot Method 145
6.2.4 The combined Algorithm for the Second Derivative Fitting and the Aggregate Boltzmann Plot Methods 146

APPENDICES 147

BIBLIOGRAPHY 158

LIST OF FIGURES

Figure

1.1 Raw image (a) and shift needed for correction (b) of the in plane vibrational noise. 4

1.2 Examples of absorption profiles for water vapor at 300 K and 2000 K over a portion of the spectrum accessible by instrumentation used in this study. Due to the temperature dependence of the population of different states, it can be seen that different transitional lines become active in the 300 K and 2000 K spectra. 6

1.3 Example of a transition shifting off of its centerline wavenumber. . . 11

1.4 Example of an absorbance Spectrum measured for a centerline frequency of 7185.5 cm^{-1}. 16

1.5 Representative Boltzmann Plot with the contribution of several isolated transitional lines plotted for two measurement cases with different temperatures and partial pressures. The slope is directly relatable to the temperature, while the y-intercept gives the partial pressure once the temperature is obtained. 23

2.1 The SU1024LDH2 Linear Array Camera usind in the spectral imaging experiments. 39

2.2 Raw image (a) and shift needed for correction (b) of the in plane vibrational noise. 40

2.3 Example of an image captured by the LAC, where the x-axis is location and the y-axis is wavenumber. The image is rendered through acquiring single spatially resolved line images and "stacking" them to form the LAC image, where each pixel gives a time trace of the laser scan, and time is converted to a change in wavenumber. 41

2.4 Example of the spectral image corresponding the image taken by the LAC in Fig. 2.3. The average absorbance of all the pixels is seen at the right hand side. 42

2.5 Scan of room air taken with and without etalon interference in the signal. The etalon peaks are on the order of magnitude of the absorption signal, causing large errors in the measure properties. The loss in the signal is due mainly to the introduction of the windows which are inducing the etalon effects. 43

2.6 Anamorphic prism pair setup in order to generate an etalon free laser sheet. The angles of the anamorphic prisms both act as sheet forming optics as well as completely removing back reflections within the sheet forming optical setup. 46

2.7 Schematic of an etalon interference region due to reflections of the laser sheet off of the windows. 48

2.8 Schematic demonstrating the various vibrational motions observed in the LAC data. The motions are in plane, where the pitch angle changes in the plane of the laser sheet, out of plane, where the pitch angle varies out of plane, and rotation. 49

2.9 Raw image (a) and shift needed for correction (b) of the in plane vibrational noise. 50

2.10 Image corrected for the in plane motion. the resulting image is left with the out of plane intensity variations, seen in (b) 51

2.11 Gaussian distribution of light for an unexpanded laser sheet (a) and for an expanded laser sheet (b). 52

2.12 Corrected image (a) and amplitude oscillation (b) demonstrating the out of plane vibrational noise for an expanded laser sheet. 54

2.13 Single shot image taken above a McKenna flat flame burner (a) an an average of 30 such images (b). 57

2.14 Example measurements taken in the low pressure cell with (a) taken at ambient pressure conditions (roughly 99 kPa), and (b) taken at 30 kPa. The effect of the lower pressure is seen in the spectral images as the absorbance regions become narrower and more peaked. 59

2.15 Images taken before and after the corrections were made to the LAC system. The etalon effect is seen in image 2.15(a), while there are no extra noises present in image 2.15(b). 61

2.16 Standard deviation taken across the pixels in space. The effect of the etalon noise is seen in the higher standard deviation values for the original optical configuration for the LAC. 62

2.17 Standard deviation taken across the array in time. The effect of the etalon noise is seen in the higher standard deviation values for the original optical configuration for the LAC, as well as the variation in the deviation. The standard deviations vary in time due to the etalon signals which can vary in both time and space as seen in Fig. 2.15 63

2.18 Temperature reconstructed from (a) the original optical setup and (b) the new optical setup. It is readily apparent that the etalon negatively impacts the solutions. The standard deviations are (a) 13 K and (b) 2 degrees K. 64

2.19 Pressure reconstructed from (a) the original optical setup and (b) the new optical setup. It is readily apparent that the etalon negatively impacts the solutions. The standard deviations are (a) 1.22 kPa and (b) 0.28 kPa. 64

2.20 Mole Fraction reconstructed from (a) the original optical setup and (b) the new optical setup. It is readily apparent that the etalon negatively impacts the solutions. The standard deviations are (a) 4.86 e-04 and (b) 1.57 e-04. 65

2.21 Comparison of the standard deviation across all pixels for the uncorrected in plane vibrational mode versus after the correction. 68

2.22 Comparison of the standard deviation across all pixels for the cases described. As the thickness of the laser sheet increases, the standard deviation in intensity decreases. 68

2.23 The mean standard deviation of the pixels in time compared to the thickness of the laser sheet for each measurement taken. As can be seen, the curve asymptotes to a specific values of about five counts, the inherent noise within the system. The specific values are tabulated in Table 2.3. 69

3.1 Demonstration of variation due to windows in the optical setup. Several scans were taken through the optical windows of the purge tube and referenced to a single line. The curvatures of these lines arise from the intensity variation with wavenumber of a scan when referenced to the intensity variation with the wavenumber of the reference scan. If no variation existed, these lines would be flat single value ratios, rather than curves. 74

3.2 Demonstration of three absorbance curves, the first representing the actual measurement, the second representing a poor fit to the wings of a scan inducing an error in the curvature of the baseline, and the third representing an error induced by offsetting the baseline. These present as errors in the reconstructed properties in the solutions, when a solution can be obtained at all. 76

3.3 Ratios of the second derivative to the zeroth derivative of the solution and error terms in Eq. 3.4 are demonstrated over a representative sample of the flow property space expected in the experiments performed in this work. The B values cancel out of the ratios leaving the solution terms as (a) $M^{(2)}/M^{(0)}$, (b) $\Omega^{(2)}/\Omega^{(0)}$, (c) $\Gamma^{(2)}/\Gamma^{(0)}$, and (d) $Z^{(2)}/Z^{(0)}$. It should be noted that as the derivative order is increased, the solutions terms grow rapidly, while the error terms either remain constant for the Ω case or are reduced as in the Γ case. 80

3.4 Example second derivative measurement shape of a transitional line compared to the traditional spectral fitting algorithm with baseline noise. . 81

3.5 Representative measurements in the low pressure cell for zeroth and second order derivatives measured at 99 kPa and 30 kPa respectively. It is evident that the fitting is much more accurate in the second derivative case for the higher pressure where the wings of the baseline are harder to fit for the zeroth order derivative fitting. In the lower pressure case, the fitting is about even for both the zeroth order and the second order derivative fits. 83

3.6 Measured values for the zeroth order derivative and the second order derivative compared to the external reference measurements. The second order derivative technique provides much more accurate solutions as the pressure continues to rise. 84

3.7 The McKenna flat flame burner setup with the laser inserted into a nitrogen sheath, with the center emitting a premixed fuel/oxidizer mixture of air and a test fuel. The experiments completed in this work used methane as a test gas due to its low flame speed and well known exhaust components. 86

3.8 Representative fits of the second derivative of the absorbance spectrum for two transitional lines. It is seen that the fit to the lines is quite accurate although the reconstructed temperature values are fairly erroneous. This is due to the presence of exhaust species in the measurement for which HITRAN has no data. 87

4.1 Example of a pair of aggregate lines contained entirely within the spectral range ($j \in \Omega$) denoted by the blue region of the spectrum. . 95

4.2 The algorithm for the Aggregate Boltzmann Plot method which takes into account the dependence on the temperature of the aggregate lower state energy. 98

4.3 The mean offset of the reconstructed temperature from the actual temperature using (a) $\sigma_\epsilon = 0.03$ and (b) $\sigma_\epsilon = 0.06$. As expected, the more lines used in the reconstruction, the lower the difference in the reconstructed temperatures. Additionally, the higher the error, the larger the skewing of the average temperature due to the non-linearity of the $\ln(1+\epsilon)$ term. 108

4.4 Standard deviation of the temperatures obtained through the Aggregate Boltzmann Plot for (a) $\sigma_\epsilon = 0.03$ and (b) $\sigma_\epsilon = 0.06$. As with the mean offset, the higher the initial error standard deviations, the larger standard deviation of the reconstructed temperatuer. 109

4.5 Four aggregate clusters used to determine the temperature of the low pressure cell using the Aggregate Boltzmann Plot. Conditions in the cell at the time of recording were approximately 295 K and 30 kPa. 109

4.6 Aggregate Boltzmann Plot through the four aggregate lines demonstrated in Fig. 4.5. Note the very high aggregate lower state energy obtained through L1a, reducing the sensitivity of the measurement to errors introduced in the integrated absorbance. 111

4.7 Aggregate Boltzmann Plot taken through the McKenna flat flame burner using four aggregate lines. The ΔE_a is large, reducing the sensitivity of the measurement to errors. 113

4.8 Repeated measurements taken through the McKenna flat flame burner and compared to the simulated Cantera temperature at the height above the burner measured. 113

4.9 Demonstration of the running value for the aggregate lower state energy as a function of location in the spectrum for a temperature of 300 K and scan width of 0.5 cm^{-1}. The absorption spectrum at the given temperature, used to visualize the strengths of the transition lines, as well as the running aggregate lower state energy is seen in (a). These running aggregate values are generated into matrices and subtracted, giving (b). The bright regions are areas where the aggregate lower state energies are widely spread indicating a potentially useful pair of aggregate spectra. . 117

4.10 The same setup as Fig. 4.9, but with a window size that is 5 times larger, 2.5 cm^{-1}. There is an evident smoothing effect on the running value of the aggregate lower state energy. 118

4.11 Demonstration of the running value for the aggregate lower state energy as a function of location in the spectrum for a temperature of 2000 K and scan width of 0.5 cm^{-1}. The absorption spectrum at the given temperature, used to visualize the strengths of the transition lines, as well as the running aggregate lower state energy is seen in (a). These running aggregate values are generated into matrices and subtracted, giving (b). The bright regions are areas where the aggregate lower state energies are widely spread indicating a potentially useful pair of aggregate spectra. . 121

4.12 The same setup as Fig. 4.9, but with a window size hat is 5 times larger. It is evident that there is a smoothing effect on the running value of the aggregate lower state energy. 122

5.1 Algorithm for the robust sensing method that combines the second derivative fitting and the Aggregate Boltzmann plot method. The resulting method is insensitive to both baseline fitting errors and spectral database errors. 126

5.2 Computationally constructed absorbance features created with the reconstructed properties obtained from the second derivative fitting for (a) 99 kPa and (b) 30 kPa for a linecenter frequency of 7185 cm^{-1}. The agreement is quite good despite the poor properties used, leading to an accurate shape. 129

5.3 The Aggregate Boltzmann Plot calculated with the computationally constructed low pressure cell measurement values for (a) 99 kPa and (b) 30 kPa for a linecenter frequency of 7185 cm^{-1}. It can be seen that the slope is approximately equivalent for the two methods, but due to the different pressures measured, the y-intercept is different between the two plots. . 130

5.4 The Aggregate Boltzmann Plot given for the lines described in Table 5.2 when used with the raw data rather than using the second derivative fitting to reduce the background and baseline errors. The reconstructed temperature from this plot demonstrates the ineffectiveness of this method to complete measurements in the presence of high background and baseline errors. 132

5.5 The Aggregate Boltzmann Plot given for the lines described in Table 5.2 when used with the accompanying second derivative fitting data. The reconstructed temperature from this plot demonstrates the effectiveness of this method to complete measurements in the presence of high background and baseline errors when coupled with the second derivative fitting. 133

5.6 The simultaneous solution for the three lines demonstrated in Table 5.2 using the second derivative only. The agreement with the expected value is far better than with the Aggregate Boltzmann Plot alone, due to the excess error introduced by baseline offsets. However, the mean measured temperature has approximately a 15% difference than the expected temperature from White [1] and Cantera due to incorrect HITRAN broadening parameters. 134

5.7 The Aggregate Boltzmann Plot temperature solution for the three lines described in Table 5.2 when used with the accompanying second derivative fitting data. The temperatures seen are much closer to the expected values of 2050 K, with the mean temperature within 6% of the expected temperature. The solution can be seen to explode in the final points of the plot, possibly due to increased errors as the optics began to heat up. 135

A.1 Experimental setup of the integrating sphere. 149

A.2 Example image of a uniform power scan taken with the LAC using the integrating sphere and TDL. 149

A.3 Comparison plot over three gain settings of the LAC experimental SNR to laser power measurements with the analytical solution to the SNR equation. As can be seen, the measured SNR and the SNR obtained using the manufacturer's specifications are closely matched, thus the LAC behaves well. 151

B.1 Algorithm describing the method by which the acceptable errors in the baseline are determined computationally. The algorithm outputs errors in pressure and temperature based on the expected pressure and temperature and the expected baseline errors. 154

B.2 Data simulated at 300 K and 1 atm for (a) the zeroth order derivative and (b) the second order derivative with RMS offset errors of 0.0534 and (c) the zeroth order derivative and (d) the second order derivative with RMS offset errors of 0.2066. 155

B.3 Data simulated at 2100 K and 2.2 atm for (a) the zeroth order derivative and (b) the second order derivative with RMS offset errors of 0.0534 and (c) the zeroth order derivative and (d) the second order derivative with RMS offset errors of 0.2066. 156

LIST OF TABLES

Table

2.1 Table demonstrating the modeled vibrational amplitude versus the measured vibrational amplitude for the out of plane vibrational case. Good agreement between the model and the measured cases are seen. 55

2.2 Table demonstrating the variation in the linestrength with temperature over several transition lines. It can be seen that these lines may or may not be effective choices due to the variation in linestrength depending on the temperature range expected in the measurement. 66

2.3 Table demonstrating the standard deviation of the uncorrected and corrected images for each of the given beam standard deviations. . . 70

3.1 Analysis of the second derivative data measured over the McKenna Flat Flame burner for a Φ of 0.87. As can be seen, there is still a large error in the solutions due to the incomplete spectral database parameters as well as other inherent noise errors. 87

3.2 Table demonstrating the variation in the linestrength with temperature over several transition lines. It can be seen that these lines may or may not be effective choices due to the variation in linestrength depending on the temperature range expected in the measurement. 90

3.3 As seen listed here, the spectral quantity of the lower state energy varies from transition to transition. In order to become insensitive to noise and sensitive to temperature, the difference in the lower state energies between two or more transitions should be maximized. . . . 91

4.1 Aggregate clusters chosen for the low pressure cell experiments. These were used for the relatively large difference in the lower state energies and for populating the Aggregate Boltzmann Plot with strong, easily measured transitions. 119

4.2 Aggregate clusters chosen for the McKenna. These were used for the relatively large difference in the Lower state energies and for populating the Aggregate Boltzmann Plot with strong, easily measured transitions. 123

5.1 Representative table of the fit properties from the second derivative fitting algorithm in the low pressure cell in two different pressures, 99 kPa and 30 kPa for the lines chosen according to Sec. 4.7.3. . . . 128

5.2 Table of the fit properties from the second derivative fitting algorithm in the McKenna burner without the benefits of the Aggregate Boltzmann Plot database error rejection. The RMS error is given to demonstrate the accuracy of the fit to the lines. 131

B.1 Direct fitting results for baselines which result in RMS errors seen in the first column generated by a baseline offset. Note that the bounds of the solution space probed by the MATLAB code would lead to a maximum error of 50%, meaning that the reconstructed values with errors of 50% are actually more erroneous than listed due to the analytical bounds. 153

B.2 Second Derivative fitting results for baselines which result in RMS offset errors seen in the first column. In all offset cases and temperature and pressure combinations, the inferred temperature and pressure are alsmost exact. 153

LIST OF APPENDICES

Appendix

A. LAC Characterization 148

B. Computational Calculations of the Second Derivative Fitting Algorithm with Representative Baseline Offset Errors 152

ABSTRACT

This work expands Tunable Diode Laser Absorption Spectroscopy (TDLAS) measurement and data processing techniques. Specifically, it introduces new data acquisition and data reduction techniques that improve scanned direct absorption spectroscopy measurements.

Current data acquisition techniques are limited in temporal and spatial resolution. Some of these limitations are resolved by extending measurements from a single point to a plane by the introduction of a novel instrumentation method, the Linear Array Camera (LAC). The use of an LAC allows for simultaneous imaging of absorption spectra on multiple points, from which the spatial distribution of pressure, temperature and species fraction can be inferred. Example measurements are presented to demonstrate the capability of a planar measurement approach. Some practical challenges are identified, and corrections are given for common design problems, as well as models to help with the design of an LAC system.

TDLAS is typically used to generate measurements of temperatures, pressures and species fraction. Their accuracy is limited by errors introduced in the measurement of the absorption profile and by the accuracy of the spectral parameters used to related absorbance to the thermochemical state. Some of these limitations are overcome by the introduction of a novel application of the second derivative fitting of the absorption spectrum, the wavenumber-domain equivalent of Wavelength Modulation Spectroscopy (WMS), a Fourier domain technique. Because the WMS technique requires fast acquisition, it is impractical for use with state-of-the-art LAC systems, which have limited scan rates. The second derivative reconstruction method allows

for insensitivity to baseline errors and increases sensitivity to small variations in the spectral absorbance, which allow for more accurate measurement of temperatures and vastly improve the measurement of pressure through spectral fitting.

The second derivative scheme, a spectral fitting technique, is dependent upon the accurate knowledge of the spectral parameters, which are typically taken from a spectral database. One common database is the HITRAN spectral database, which lists parameters for the spectral transitions and includes collisional parameters for air and self broadening. In actual applications, such as in combustion environments, the collisional partners are frequently far more numerous than air and self collisions. The lack of these parameters can introduce errors into the reconstructed measurements. This can be addressed through the use of the Boltzmann Plot method, which makes use of the integrated area under a number of isolated transitions to negate the dependence on accurate broadening parameters. To overcome the necessity for isolated features an extension is introduced, referred to as the Aggregate Boltzmann Plot method, based on the concept of aggregate spectrum within a Boltzmann Plot framework to expand its applicability to high pressure and temperature conditions where spectral blending has prevented the application of the traditional Boltzmann Plot method.

The Aggregate Boltzmann Plot requires accurate measures of spectral profiles, which are affected by baseline errors resolvable by second derivative fitting. Therefore, through the combination of second derivative fitting and the Aggregate Boltzmann Plot method, a robust measurement technique is obtained. This technique applies the second derivative fitting to obtain baseline insensitive spectral profiles, which are then applied in the Aggregate Boltzmann Plot method to mitigate the effects of missing broadening parameters. This results in a robust measurement technique capable to generate accurate measurements under conditions that were previously inaccessible by traditional approaches based on scanned direct absorption methods.

CHAPTER I

Introduction and Background

The field of Aerospace Engineering contains the need for a plethora of diagnostic techniques to cover a wide and varied set of flow field conditions. Because the properties of flows of interest cover such an extensive scope, no single measurement technique is applicable to all cases. For the study of shocks, the Schlieren imaging technique can be applied to observe shock locations and movement through the deflection of light as it passes through density gradients[2]. In the study of flow field velocities, Particle Imaging Velocimetry (PIV) is often used, where particles are tracked within a flow to determine their speed and direction[3]. In flame measurements, Planar Laser Induced Fluorescence (PLIF) can be used to track the edge of a flame by detecting the intermediate combustion species through laser excitation[4]. Tunable Diode Laser Absorption Spectroscopy (TDLAS) allows for certain species in a flow to be probed, and uses the resulting spectra to calculate flow properties including pressure, temperature, and species concentration. For an overview of the imaging techniques described, the reader is directed to Clemens "Flow Imaging" chapter in the *Encyclopedia of Imaging Science and Technology*[5] and Trolinger [6]. Each of these diagnostic methods gives specific knowledge to cases of interest in aerospace. Additionally, each technique is limited by the constraints of the techniques, such as the size of the measurement system, the range of operating conditions each technique is

sensitive over, and noise inherent within each diagnostic technique. These techniques are applied for everything from understanding the underlying physics of combustion and fluid flows, to real time testing of experimental systems. The overarching goal of these techniques is to improve upon existing aerospace systems.

The novel contributions of this work that will broaden the scope of TDLAS are: (1) the design of a novel system setup using a Linear Array Camera (LAC) to improve upon spatiotemporal resolution limits, (2) the novel implementation of a fitting technique using the second derivative of the absorption features to mimic the benefits of traditional Wavelength Modulation Spectroscopy techniques with limited systems hardware, and through the modification of an existing processing technique, the Boltzmann Plot method, which will allow for this reconstruction technique to be applicable over much higher temperatures and pressures than canonically have been able to be used, and (3) a combination of the Second derivative and Aggregate Boltzmann Plot methods to generate an inference scheme which obtains the benefits of both techniques while mitigating the errors encountered when using them separately. The methods described herein are general techniques which can be applied to any absorber species, but for the purpose of this work, will be applied to H_2O.

flight ready hardware

1.1 Motivation

The measurement of flow properties is critical in the understanding of aerospace systems and applications. In combustion measurements, temperature is a critical parameter both in determining the efficiency of combustion and the necessary material properties to contain the combustion process. Measurement of flow species can be used to determine where a reaction is occurring, and the completeness of that reaction. Pressure measurements can give lift and drag on an airfoil and lend insight into the pressure gains or losses in a system. Tunable Diode Laser Absorption Spectroscopy

is a convenient measurement technique which can be used to obtain these properties without the drawbacks of traditional measurement probes causing flow disruption [7]. Advancements in optical telecommunications systems have allowed for easily set up TDLAS optical probes for combustion species of interest including H_2O, CO, CO_2, and NO [8, 9, 10, 11]. However, there are serious limitations in measurement techniques, noise, and reconstruction techniques. High temperature and pressure cases are difficult to measure rapidly, cheaply, and accurately. The techniques used to obtain properties in flows such as these either have high systems costs and long processing times, or they are relatively inaccurate. The field of aerospace engineering is rapidly expanding into systems in these regimes, such as ramjets, scramjets, and Rotating Detonation Engines (RDEs). This leaves a large gap in the current state of the art, where rapid, cheap, flight ready systems and processing are missing. This thesis will fill these gaps through the application of novel instrumentation which can expand traditional integrated path measurements to planar measurements, and processing techniques which will allow for rapid processing of lower resolution data and which may have large errors induced by poor baseline measurements and empirically fit broadening parameters.

1.2 Overview of Tunable Diode Laser Absorption Spectroscopy

TDLAS is a well understood and frequently used diagnostic method for fluid flows. For a good overview, the reader is directed to the review papers by Allen and Liu [12, 13]. Molecules have ro-vibrational energy states, with specific energy levels for these states. Transitioning from one state to another takes a quantized amount of energy. By exciting these states with specific frequencies of light, the energy from the light can be used to move molecules from one ro-vibrational state to

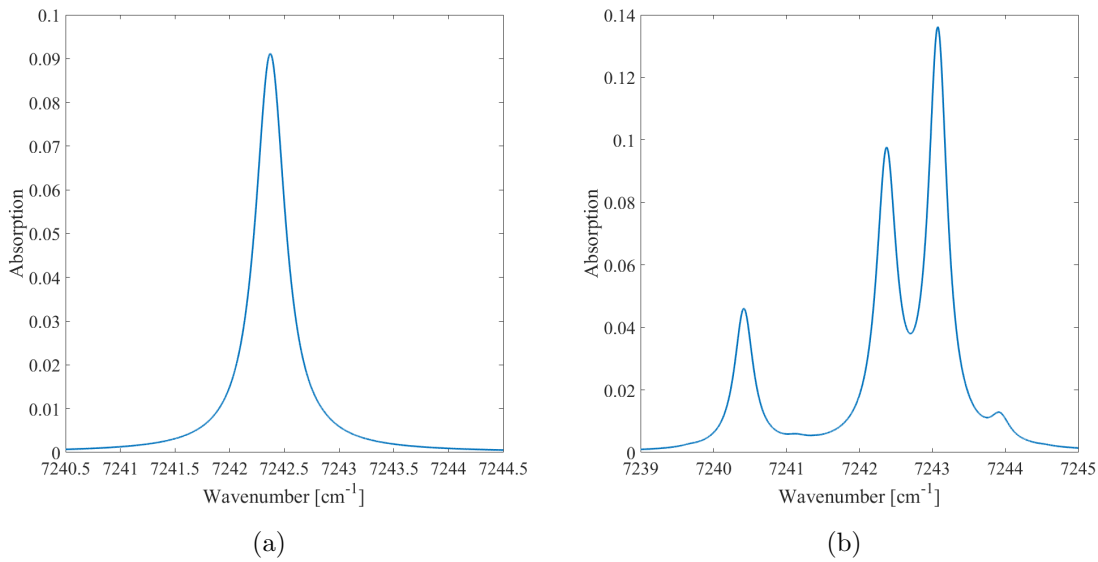

Figure 1.1: Raw image (a) and shift needed for correction (b) of the in plane vibrational noise.

another. The frequencies at which molecules change states are called transitional lines or merely transitions, where the molecule transitions from one state to another. The summation of all the molecular transitions for a specific molecule is the absorbance spectrum for that molecule. An example of a transition is seen in Fig. 1.1(a), while the spectrum around this transition, the summation of all the lines in the vicinity of the spectral feature, is given in Fig. 1.1(b). It is seen that transition observed at 7242 cm^{-1} is surrounded by several other spectral features in close proximity and the transitions overlap. This is denoted as blending between transitions. The incident and transmitted laser intensities can be related to the absorbance of the light through the application of Beer's Law as seen in Eq. 1.1

$$I = I_o e^{-\alpha_\nu} \tag{1.1}$$

where I is the laser intensity transmitted through the absorbing medium, I_o is the incident laser intensity, and α is the absorption coefficient. The absorption coefficient

is given as

$$\alpha_\nu = -\log\left(\frac{I(\nu)}{I_o(\nu)}\right) = \sum_{i\in\Omega}\int_0^L P(\ell)\,\chi(\ell)\,S_i(T)\,\phi_i(P,T,\nu)\mathrm{d}\ell \tag{1.2}$$

For a path of length L of uniform properties, the above reduces to:

$$\alpha_\nu = \sum_{i\in\Omega} P\chi S_i(T)\,\phi_i(P,T,\nu)L \tag{1.3}$$

Where the summation of individual transition lines is extended over a range Ω, P is the pressure of the absorbing medium, χ is its mole fraction, $S(T)$ is the linestrength of a particular transition within Ω, and ϕ is the lineshape of a particular transition within Ω. For this work, the absorbing species is H_2O and the lineshape function is taken as a Voigt with the lineshape parameters coming from the HITRAN database [14]. The linestrength for transition i is given as:

$$S_i(T) = S_i(T_o)\frac{Q(T_o)}{Q(T)}e^{-\frac{hcE_i''}{k}\left(\frac{1}{T}-\frac{1}{T_o}\right)}\frac{1-e^{-\frac{hc\nu_{o,i}}{kT}}}{1-e^{-\frac{hc\nu_{o,i}}{kT_o}}} \tag{1.4}$$

and is a function of temperature. Here, T_o is the reference temperature (generally 296 K), Q is the partition function, h is Planck's constant, c is the speed of light, E'' is the lower state energy, k is Boltzmann's constant, and ν_o is the linecenter frequency of the transition. This equation accounts for both emitted and absorbed light at a given wavelength. In this work, the emission term is negligible, giving:

$$S_j(T) = S_i(T_o)\frac{Q(T_o)}{Q(T)}e^{-\frac{hcE_i''}{k}\left(\frac{1}{T}-\frac{1}{T_o}\right)} \tag{1.5}$$

The linestrength equation describes the relative population of the molecules at a particular state based upon the partition function. These states become populated at different temperatures, leading to transitions becoming active in different flow

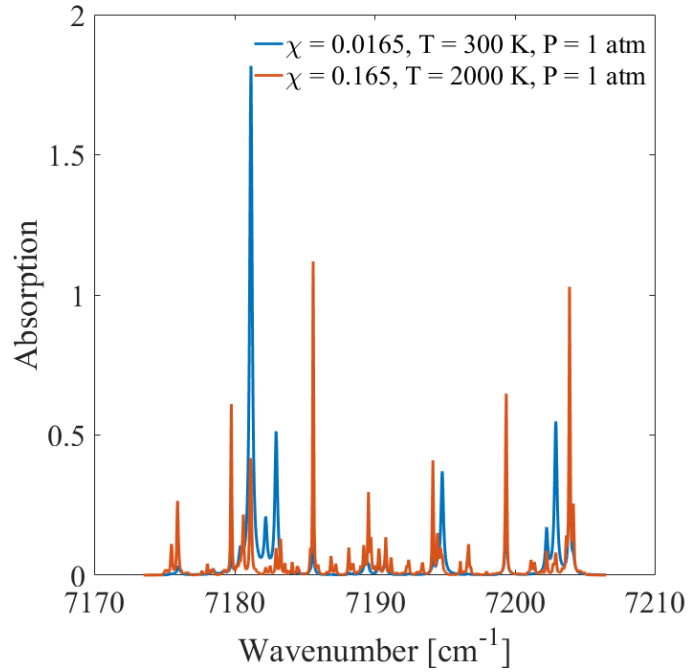

Figure 1.2: Examples of absorption profiles for water vapor at 300 K and 2000 K over a portion of the spectrum accessible by instrumentation used in this study. Due to the temperature dependence of the population of different states, it can be seen that different transitional lines become active in the 300 K and 2000 K spectra.

regimes. Transitions which have very strong linestrengths in ambient room temperatures may not be active in relatively high temperatures such as those seen in a burner and vice versa. The linestrength is visible in the absorption spectrum in the size of the transitions measured. These lines shown in Fig. 1.2 are plotted for absorption profiles at 300 K and 2000 K. It is prominent that the different transitions are effective at different temperature ranges, some of the lines are very strongly apparent in near atmospheric temperatures with others appearing only at the elevated burner temperatures. It is important to obtain lines with reasonably high linestrengths at the temperatures expected within the experiment such that the SNR of the measurement is adequate.

1.3 Lineshape Functions

There are several approaches to determining the lineshape of a transition. The accuracy of these methods is determined by the properties of the flow regime that are being probed. Different regimes affect the shape of the absorption profile in different ways and can therefore be modeled by different profiles. One such way the lineshape can be affected is through broadening. Two phenomena causing broadening of the lineshape are Doppler broadening and collisional broadening. Doppler broadening occurs due to the random motion of the absorbing species in the flow. As molecules move, the effective wavelength of the absorbed light varies due to the Doppler effect. This causes the absorption transition line to be broadened as different wavelengths are absorbed by molecules moving at various velocities centered about the central absorbing wavelength for a given transition. A second broadening method is collisional broadening. As particles collide, energy is transferred between the particles, causing the absorbed light to be broadened about the central absorbing wavelength. When either Doppler or collisional broadening dominate, the lineshape can be modeled as a Gaussian or Lorentzian profile respectively. In intermediate regimes, the lineshape is frequently modeled as a Voigt profile, which is the convolution of the Gaussian profile with the Lorentzian profile. This is the lineshape function assumed in this thesis.

1.3.1 Gaussian Lineshape Function

The Gaussian lineshape function is appropriate whenever Doppler broadening dominates the lineshape. This occurs in low pressure and high temperature cases, when collisions between molecules are infrequent and there is a broad probability distribution function for velocities. The lineshape is then modeled as:

$$\phi_G(\nu) = \frac{1}{\Delta\nu_G}\left(\frac{\ln(2)}{\pi}\right)^{0.5}\exp\left(-\ln(2)\left(\frac{\nu-\nu_o}{\Delta\nu_G}\right)^2\right) \tag{1.6}$$

The half width at half max (HWHM) for this profile shape is given as:

$$\Delta\nu_G = \frac{\nu_{o,i}}{c}\sqrt{\frac{2\ln(2)\,kT}{m}} \tag{1.7}$$

The HWHM is a function of the line center wavelength $\nu_{o,i}$, the temperature, and the molecular mass m. The Gaussian profile is broadened by increasing temperatures and narrowed as a function of the molecular weight. It is also notable that the line center frequency affects the broadness of the profile as well.

1.3.2 Lorentzian Lineshape Function

The Lorentzian lineshape function is a good model in high pressure and low temperature environments, where collisional broadening is the dominant broadening effect. In these cases, there are frequent collisions between molecules while they move at slower speeds. The profile is modeled as seen in Eq. 1.8.

$$\phi_L(\nu) = \frac{1}{\pi}\frac{\Delta\nu_L}{(\nu-\nu_{o,i})^2 + (\Delta\nu_L)^2} \tag{1.8}$$

and the half width at half max for this profile can be modeled as:

$$\Delta\nu_L = P\sum_j \chi_j\gamma_j(T) \tag{1.9}$$

Here, the HWHM is broadened by the collisional broadening coefficient, γ_j, of a specific collisional partner j, weighted by the mole fraction of the collisional partner.

It is important to note that the collisional broadening coefficients are obtained typically from spectral databases, which may have significant uncertainties. These databases, such as HITRAN, are populated experimentally and are continually being updated with more accurate parameters. Experiments, such as those completed by Upschulte and Kauranen [15, 16], can give more accurate parameters to the spec-

tral databases and demonstrate where better accuracy is needed. Many researchers have worked on collecting and surveying the research in order to fill gaps in the databases[17, 18], and this research is ongoing. Accurate values for the database are necessary to calculate the true FWHM. Often, databases only contain the broadening parameters for self collisions and collisions with air molecules, but in aerospace flows of interest where combustion exhaust species often act as collisional partners to the probed molecules, the collisional broadening parameters for these exhaust gases are needed. For instance, in this work, H_2O is the species of interest being probed, but in methane-air combustion chemistry, a large fraction of the exhaust is CO_2, which is not often accounted for as a collisional partner in the spectral databases. Additionally, the coefficient is dependent on temperature, as seen below:

$$\gamma_j\left(T\right) = \gamma_j\left(T_o\right)\left(\frac{T_o}{T}\right)^n \tag{1.10}$$

The exponent for the temperature term is obtained from the spectral databases, but is often only given for self broadening and air broadening. This is a challenge to making measurements in the exhaust of hydrocarbon fueled combustion systems.

1.3.3 Voigt Lishape Function

Most cases of interest fall in between these two regimes, where both Gaussian and Lorentzian broadening occur and neither is dominant. In these cases, a typical lineshape function used is the Voigt. This is a convolution of the Gaussian and Lorentzian lineshape functions, and accounts for both broadening methods. The profile is modeled as:

$$\phi_V = \frac{\sqrt{\ln\left(2\right)/\pi}}{\Delta_G} K\left(x, y\right) \tag{1.11}$$

where the Voigt function $K(x, y)$ is given as

$$K(x, y) = \frac{y}{\pi} \int_{-\infty}^{\infty} \frac{\exp(-t^2)}{(x-t)^2 + y^2} \mathrm{d}t \tag{1.12}$$

and

$$x = \sqrt{\ln(2)} \frac{\nu - \nu_o}{\Delta_G} \tag{1.13}$$

$$y = \sqrt{\ln(2)} \frac{\Delta_L}{\Delta_G} \tag{1.14}$$

The half width at half max for this profile is approximated *Whiting* as:

$$\Delta\nu_V = \frac{\Delta_L}{2} + \sqrt{\frac{\Delta_L^2}{4} + \Delta_G^2} \tag{1.15}$$

As can be seen, if the Doppler broadening dominates, $\Delta\nu_G >> \Delta\nu_L$, the Gaussian HWHM of the profile is recovered, and if collisional broadening dominates,$\Delta\nu_L >> \Delta\nu_G$, the Lorentzian HWHM of the profile is recovered.

There are also many numerical approximations and algorithms to the Voigt function intended to reduce computation times [19, 20, 21, 22, 23], as well as review papers that compare them for accuracy and speed [24, 25]. These can be given in terms of the half width at half max of the Gaussian and Lorentzian profiles. It is also possible to obtain the Voigt from the real part of the Fadeeva function, which is easier to solve computationally than the convolution terms.

1.4 Wavelength Centerline Shifting

The centerline of the absorbance profile can shift due to various effects. An example of what this shift can look like is seen in Fig. 1.3, where the transition has moved off of it's centerline wavenumber. This section will briefly discuss two phenomena that contribute to shifting the centerline wavelength of a transition from its undisturbed

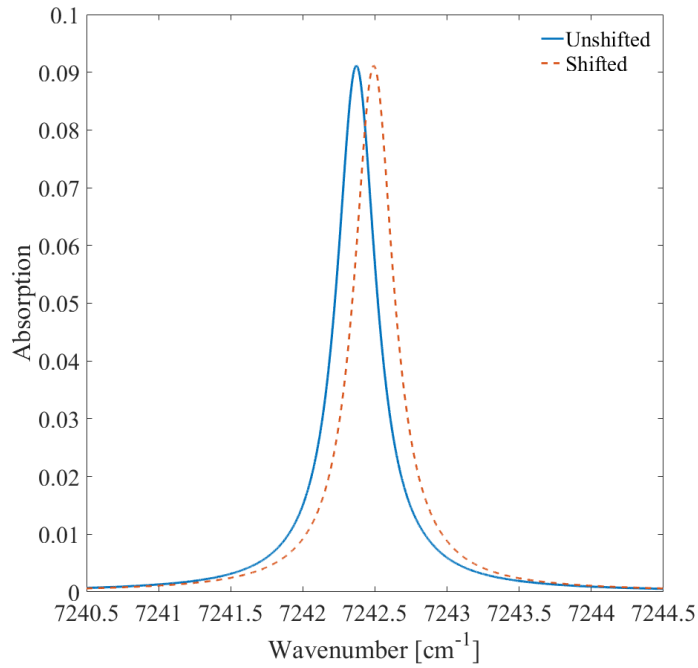

Figure 1.3: Example of a transition shifting off of its centerline wavenumber.

position, Doppler shifting and pressure shifting.

1.4.1 Doppler Shifting

Doppler shifting of a centerline wavelength can occur through the same mechanism by which Doppler broadening occurs: through the motion of the particles inducing an apparent shift in the wavelength of the incident light [26]. For Doppler broadening, this happens due to the random thermal motion of particles that gives a distribution of shifted frequencies resulting in a Gaussian absorption profile. A centerline shift due to Doppler shifting results from the bulk motion of a gas, which then induces an overall apparent frequency shift within the incident light for all particles. This shift is given by the equation:

$$\Delta\nu_o = \nu_o \frac{v \cos\theta}{c} \tag{1.16}$$

where v is the bulk velocity, c is the speed of light, and θ is the angle between the flow and the incident beam. This effect can be used to determine the velocity of a

test gas through looking at the centerline shift of an molecular transition. These can be seen applied in Miller et al. [27], where full scale velocimetry measurements have been performed on Pratt & Whitney F-100 gas-turbine engine using scanned direct absorption spectroscopy, as well as in shock tubes as applied by Phillipe and Hanson [28] using wavelength modulation spectroscopy.

1.5 Pressure Shifting

A second centerline wavelength shifting mechanism is pressure shifting, and this occurs due to intermolecular potential differences that affect the spacing between energy levels [29]. This change in the energy level spacing results in a shift in the centerline frequency of an absorbing transition, as the required quantized energy to cause a transition has now changed. This effect is experimentally measured, and is empirically modeled by:

$$\Delta\nu_o = P \sum_j \chi_j \delta_j \tag{1.17}$$

where, for collisional partner j, the pressure shift coefficient, read from a spectral database, is weighted by the mole fraction of that collisional partner. This is a linear function in pressure for a given transition. The coefficients are able to be both positive and negative depending upon the transition probed. These shifts can be significant: as an example, a shift occurring in the transitional line centered at 7199 cm^{-1} in a methane-air flame can have an induced pressure shift at 2 atm of approximately equal magnitude to a velocity shift measured at a 45°angle in a Mach 1 flow. Whenever a high speed, high pressure measurement is necessary, such as in a scramjet combustor, the pressure shift must be taken into account. The pressure shift coefficient, like the collisional broadening coefficient, is dependent on the temperature. This is modeled as:

$$\delta_j\left(T\right) = \delta_j\left(T_o\right)\left(\frac{T_o}{T}\right)^m \tag{1.18}$$

where, $\delta_j\,(To)$ and m are given in spectral databases such as HITRAN. As before, these coefficients are not always listed in spectral databases, leading to errors when secondary flow species are present.

1.6 Common TDLAS Data Acquisition Techniques and Processing Methods

Several methods of data acquisition make use of the fundamentals of TDLAS in order to obtain flow properties. These methods tend to balance the complexity of the system with the quality of the measurement, and each has its own merits and faults. The acquisition methods tend to have their own processing techniques, which have varying degrees of complexity, accuracy, and processing speeds. This subsection will describe some of the common techniques that are used along with the limitations of each method.

1.6.1 Fixed Wavelength Direct Absorption Spectroscopy

Fixed Wavelength Direct Absorption Spectroscopy (FWDAS) is perhaps the most straightforward method of TDLAS data acquisition. In this technique, a laser beam is tuned to a specific wavelength - often the center line wavelength for a particular transition k - and held constant. The incident intensity is measured as well as the transmitted intensity. The equation for the spectral absorbance at a particular wavelength then becomes:

$$\alpha_{\nu,k} = -\ln\left(\frac{I_k}{I_{o,k}}\right) = \int_0^L P\chi S_k\,(T)\,\phi(P,T,\nu_k)\mathrm{d}\ell \tag{1.19}$$

or if the properties are uniform along the path length,

$$\alpha_{\nu,k} = -\ln\left(\frac{I_k}{I_{o,k}}\right) = P\chi S_k\,(T)\,\phi(P,T,\nu_k)L \tag{1.20}$$

Taking the ratios of two of these spectral absorbances gives:

$$\frac{\alpha_{\nu,k}}{\alpha_{\nu,l}} = \frac{S_k\left(T\right)\phi(P,T,\nu_k)}{S_l\left(T\right)\phi(P,T,\nu_l)} \tag{1.21}$$

If information about the pressure is known, this ratio reduces to a function of temperature only. This technique is easily performed and can be processed at very high speeds, but is lacking in the properties it is able to accurately reconstruct.

This technique has been demonstrated numerous times in various pressure cell and combustion environments [30, 31, 32, 33]. The design of a FWDAS sensor is described by Nagali [30], in which a method for thermometry using the above equations is given. They discuss the need to assume flow species and broadening parameters in order to make use of the method. This is due to the fact that the broadening parameters are species dependent, and spectral databases are frequently missing these parameters.

A sensing technique is described and tested by Baer et al [31] in which both a fixed wavelength and scanned wavelength method are tested. The broadening parameters used are effective parameters that include all of the possible collisional broadening terms. The FWDAS ratiometric thermometry technique matches temperatures well with both the thermocouple measured temperatures and the Scanned Wavelength Direct Absorption Spectroscopy (SWDAS) data taken at temperatures from approximately 1100 K to 1800 K. The benefits of FWDAS drawn the scanned method as described by Baer are such that it can be useful in higher pressure cases, where the spectral broadening of the absorption features means that data can be lost in the wings of the measurements.

Sanders [32] describes the implementation of the technique described in Baer [31], applying it to pulse detonation engines (PDEs), in which rapid accumulation of data points due to the FWDAS setup allows for a PDE pulse to be time-resolved in terms of the flow properties. The measurement method is extended to multiple absorption

lines, which Sanders uses to observe several species simultaneously (JP-10, soot, and H_2O).

As recently as 2016, Brittelle [33] discuses a FWAS system which is theoretically designed for H_2O measurements over 800 K to 2100 K and 1 to 30 bar, although the testing was carried out in near ambient conditions due to the missing HITRAN parameters, which can skew the measurements. Brittelle concludes by claiming that the future of the method is dependent on the improvement of the spectral databases.

From these sources, it is observable that there exist several drawbacks to this technique. The first is that the lineshape must be very well known. The lineshape function ϕ is present in the solution equation and can introduce errors if parameters such as the collisional broadening terms are incorrect or missing. This is often the case with combustion flows since the collisional partners are often not included in the databases. This method also depends on precisely obtaining measurements at a well known wavelength in a spectrum, therefore requiring precise laser calibration. If the laser wavelength is offset by some small amount, then ν_k will be incorrect in the measurement, leading to errors in the solution. Lastly, pressure shifting can also induce errors in this technique. Because the measurement relies on the accurate knowledge of spectral parameters and a well known spectral profile, shifting of the centerline absorption feature can induce errors in the reconstruction of flow properties. These various errors can compound and make the direct absorption spectroscopy method unreliable for high accuracy measurements.

1.6.2 Scanned Wavelength Direct Absorption Spectroscopy

Scanned Wavelength Direct Absorption Spectroscopy (SWDAS) is the next step up from FWDAS in that the laser wavelength is tuned about a central wavelength in order to capture an entire absorbance transition, rather than holding the wavelength fixed. This corrects several issues that arise from the FWDAS. In FWDAS, the wave-

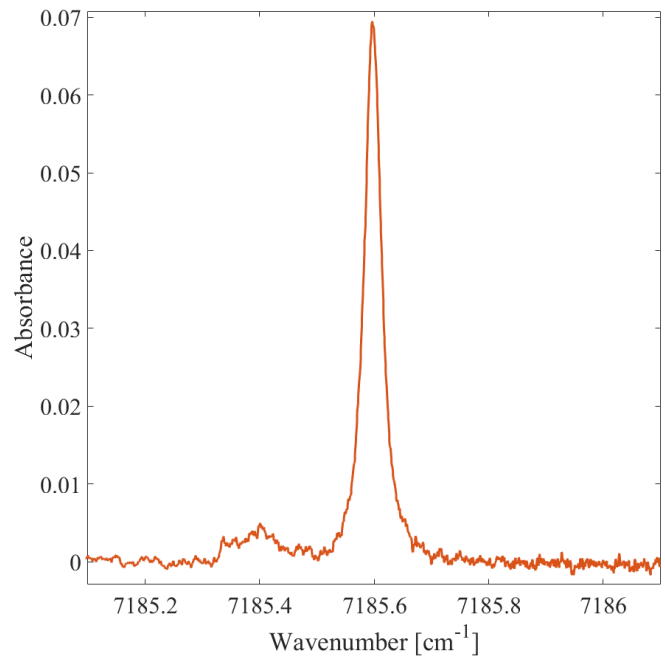

Figure 1.4: Example of an absorbance Spectrum measured for a centerline frequency of 7185.5 cm^{-1}.

length of the laser must be very precisely known in order to capture the information properly. In SWDAS, the entire absorption feature can be captured so that the peak of the feature is seen in processing, allowing for corrections to be made due to shifting of the center line frequency. The absorption profile is obtained from the ratio of the intensities as seen in Eq. 1.2. This gives a spectral feature as seen in Fig. 1.4, where the entire transition lineshape is captured.

1.6.2.1 Ratiometric Thermometry

There are several techniques with which properties can be obtained from measured absorption lines or spectra. One approach is based on using the ratio of the integrated absorbance of two different transitions. The integrated absorbance is given as:

$$A_i = \int_{-\infty}^{\infty} -\log\left(\frac{I}{I_o}\right) d\nu = \int_{-\infty}^{\infty} \sum_{i\in\Omega} \int_0^L P\chi S_i\left(T\right)\phi_i(P,T,\nu)\mathrm{d}\ell\mathrm{d}\nu \tag{1.22}$$

One property of the lineshape function is that it integrates to unity over the entire wavenumber range regardless of flow conditions. In addition, if the properties are uniform over the path length, the integrated absorbance reduces to:

$$A_i = \sum_{k \in \Omega_i} P \chi S_k \left(T\right) L \tag{1.23}$$

Taking the ratio of two of these integrated absorbances gives:

$$\frac{A_i}{A_j} = \frac{\sum_{k \in \Omega_i} S_k \left(T\right)}{\sum_{l \in \Omega_j} S_l \left(T\right)} = f(T) \tag{1.24}$$

which is a function of only the temperature of the gas. It can be easily demonstrated that the sensitivity of this method relies on the difference in lower state energies, where the larger the difference in the lower state energies, the more precisely the temperatures can be measured. This method is easy and rapidly calculated, making it an attractive method for on-line temperature monitoring systems.

Baer [31] demonstrates this alongside his FWDAS ratiometric method. Because the absorption is integrated, the dependence on the effective broadening parameter drops out of the equation. Data is measured at approximately 1100 K to 1800 K and compared to the FWDAS method and thermocouples with good agreement. The obtained temperatures are used to generate Voigt profiles and the residuals between the measured and approximated Voigt fits are less than 5%.

Arroyo [34] obtains accurate spectral parameters through measurements in a 15 cm length static cell in order to reduce the errors acquired from the poor spectral databases. Once obtained, measurements are completed through room air and fair agreement is obtained with the ratiometric thermometry technique. They observe poorly reconstructed temperatures when using line pairs with similar lower state energies, which is to be expected from the sensitivity dependence on lower state energy differences. They also note the errors induced by the blending of spectral

peaks, which makes it challenging to obtain accurate measurements. The technique was also applied in a flame environment, in which poor agreement was found based on the lines chosen. This poor agreement was potentially due to a missing transition in the HITRAN database and the poor sensitivities of the lines chosen. The differences in the lower state energies were not large enough to have high temperature sensitivity in the measurement.

Arroyo also applied this ratiometric technique to a shock tube[35], measuring the temperatures in a number of cases where shocks were induced in different mixture fractions of H_2O and O_2. The measured data was compared to theoretical temperatures for the shocks and good agreement was found using this technique.

Additionally, Schultz et al [36] have applied this ratiometric technique in a direct connect scramjet combustor. The method was probing a CO_2 transition and testing alongside a wavelenegth modulation spectroscopy measurement that was probing CO and H_2O transitions. Good agreement was reached in terms of the temperatures and analysis of the errors suggests that the fluctuations in the measurements made are due to variations in time, rather than errors induced by the measuement techniques.

Allen and Kessler [37] demonstrate some of the dependence of sensitivities in choices of line pairs for the ratiometric technique. This is done through the observation of various line pairs in different flow regimes and comparing how the increased sensitivity from well chosen line pairs affects the accuracy of the measurements in the presence of noise. Their demonstrations show that, using off-the-shelf components at that time, good accuracy was easily attainable for 300 K to 1300 K with the possibility of extending accurate measurements to 1900 K.

From these demonstrations, it is evident that the ratiometric thermometry technique is a quick and reliable method for determining the temperature of the flow. However, it does rely on accurate knowledge of the lower state energies of the transitions in order to avoid errors [34]. The integrated absorption must also be accurate

in order to obtain good measurements, as the ratios are based upon the spectral area ratios. It is important to note that the technique only gives temperature, not simultaneous properties of the temperature, pressure, and species fraction. As such, it is applicable in flows where these parameters are either known, or are not of great importance. Lastly, because the sensitivity is very dependent on the areas of the integrated absorbances, certain transitional lines are not applicable to certain flow regimes, either due to low differences in the lower state energy or weak linestrengths at certain temperatures. This means that the system is not as robust in environments where the flow properties vary over a large range, unless many lasers are used and scanned simultaneously, which increases both the cost and footprint of the system.

1.6.2.2 Spectral Fitting

A second method for the application of SWDAS, is spectral fitting. This technique takes a measured absorption line or spectrum and uses nonlinear least squares regression to attempt at finding the best fit solution by minimizing the error between the measured absorption spectrum and a spectrum calculated from Eq. 1.2. This technique is used both in the determination of spectral quantities if the conditions are well known [34, 38], or in calculating the flow properties when the spectral quantities are well known [35, 39, 40, 41].

Accurate measurements of flow properties rely heavily on the accuracy of spectral parameters. In order to obtain these parameters, it is possible to use spectral fitting and a well calibrated setup in order to back out the parameters from absorption lines. Arroyo et al [34] and Goldenstein et al [38] both demonstrate this in their experiments. In order to obtain accurate measurements with the lines that are used, spectral database parameters were checked by filling test vessels with calibrated mixtures of vapors and gases, such as pure H_2O and H_2O-N_2 mixtures at various externally measured temperatures and pressures. These validated spectroscopic parameters were

then used in experiments.

Conversely, if the parameters are well known, the flow properties can be reconstructed using these fittings. Scherer [40] demonstrates a gas analyzer for the measurements of oxygen, carbon monoxide, and hydrogen chloride through acquiring laser scans, fitting a baseline and completing a nonlinear least squares fit to the profile using a Voigt lineshape. The application for these measurements is combustion detection in spacecrafts, using lightweight TDLAS equipment for a mobile measurement platform, which is capable of continuous operations over long periods of time.

Spearrin [39] uses spectral fitting to obtain flow properties of CO and CO_2. These experiments are completed in a scramjet application, where in situ measurements of exhaust gases can help close out the chemical reaction for hydrocarbon combustion which give insight into combustion efficiency. Spatially resolved measurements can be scanned over a grid through the use of a translational stage with mounted optics.

Prior work [34, 39, 41] has noted several problems that can induce inaccuracies in the measurements. One such way is that the accuracy of the spectral fitting methods are dependent upon the baseline, I_o, measurements. Baseline offsets can induce errors in the measured absorbances, with no perfect method for reducing these errors [34]. In harsh environments, such as in a scramjet combustor, the uncertainties in the measurements come mainly from the quality of the baseline and fitting schemes[39]. Li et al [41] also note that boundary layers can induce poor fits, which can lead to inaccuracies.

Sappey et al [42] use direct scanned absorption in a wavelength multiplexed system measuring 9 unique wavelengths which cover 4 combustion exhaust species: H_2O, CO, CO_2, and O_2. This allows for simultaneous measurement of many exhaust parameters to help quantify the efficiency of the combustion being measured.

From the prior work, it can be noted that the spectral fitting method can be applied across a wide variety of aerospace flows and give inferred measurements of tem-

perature, pressure, and species fraction readily. The systems are compact and flight ready, but they are heavily dependent on spectral databases and accurate knowledge of these spectral quantities. Additionally, they are baseline dependent, where poor baseline measurements can induce errors and cause inaccuracies in the measurements.

1.6.2.3 Second Derivative Fitting

A subset of spectral fitting, Second Derivative Fitting, has been explored as well. Using the second derivative to increase sensitivity to minor variations in absorption features and bands is a common technique. Second Derivative Spectroscopy has been applied to large spectral scan width broadband absorption and emissions signals in an effort to achieve higher accuracy solutions in under resolved measurements and additionally to resolve overlapping pairs of spectral lines, where a weak absorption band is obscured by a stronger band in order to increase the accuracy of the inferred measurements[43, 44]. Analysis into the errors of second derivative spectroscopy of mixtures and linearization of the equations have also been studied by O'Haver and Hawthorne[45, 46]. Olsen and Grieble, in a two part set of papers, describe a moethod for determining line profiles from the second derivative and practically obtaining the second derivative from modulating the wavelength [47, 48]. Frequently, second derivative fitting is used in bio-medical procedures, in which large regions of an absorption or emissions spectra are scanned, and important information is often hidden in the wings or in blended under resolved regions of the spectrum. Such applications include the monitoring of the freshness of beef [49], protein measurements [50], and chromium in human urine [51]. Additionally, the technique has been used in testing waste water samples for nitrates [52], freshwater samples for nitrogen compounds [53], and combustion species measurements in broadband UV combustion measurements [1]. In each of these cases, the spectrum was under resolved and much information was obscured for typical spectral fitting algorithms. The second derivative is able to

resolve these missing segments of information through observing the spectral curvature, greatly increasing the accuracy of the measurements. The technique has been applied over a wide variety of laser wavelength cases ranging from UV to NIR.

1.6.2.4 The Boltzmann Plot Method

Lastly, the Boltzmann plot method is a technique by which several isolated transitional lines are measured and used to obtain the temperature and partial pressure of a system. This is done through solving the linestrength equation and the integrated absorbance equation, and combining them to obtain a linear relation in terms of the measured integrated absorbance and the lower state energy. The Boltzmann plot equation can be see below:

$$\ln\left(\frac{A_j}{S_{o,j}}\right) = -\frac{hc}{k}\left(\frac{1}{T} - \frac{1}{T_o}\right)E_j'' + \ln\left(\frac{Q_j(T_o)}{Q_j(T)}\frac{\chi P\ell}{kT}\right) \tag{1.25}$$

The y-coordinate in a Boltzmann plot is given by the term on the left hand side of the equation, the measured integrated absorbance, which correspond to the area integrated under the spectral absorbance profile. The slope is given by $-\frac{hc}{k}\left(\frac{1}{T} - \frac{1}{T_o}\right)$, which is a function of temperature only, and the x-coordinate is the lower state energy of the transition E_j''. The final term, $\ln\left(\frac{Q_j(T_o)}{Q_j(T)}\frac{\chi P\ell}{kT}\right)$, is the y-intercept and gives the partial pressure of the absorber. An example of a Boltzmann Plot is seen in Fig. 1.5, where two measurement cases are represented for different temperatures and partial pressures. The slopes of the two lines would give the temperatures for the two transitions, while the y-intercepts would give the partial pressures. This method of property reconstruction is insensitive to the missing broadening parameters due to its use of the integrated area, wherein the lineshape function integrates to one. However, it is necessary to use sufficiently isolated transitions, due to the spectral nature of the equation. If there are lines which are blended, i.e. if nearby transitions interfere with

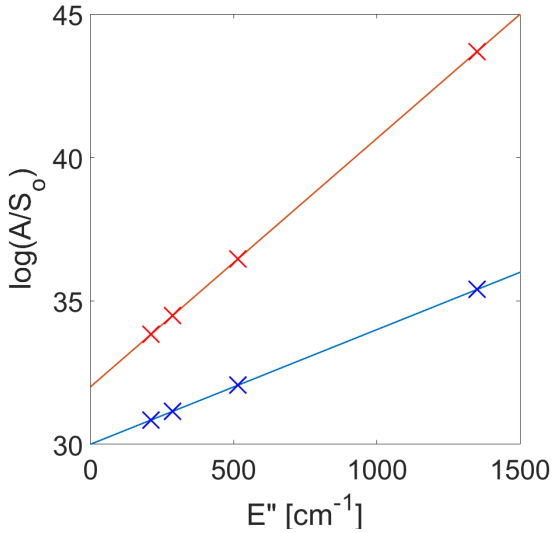

Figure 1.5: Representative Boltzmann Plot with the contribution of several isolated transitional lines plotted for two measurement cases with different temperatures and partial pressures. The slope is directly relatable to the temperature, while the y-intercept gives the partial pressure once the temperature is obtained.

each other as seen in Fig. 1.1(b), the Boltzmann plot method begins to fail. The derivation and further demonstrations of the Boltzmann plot method will be further discussed in Chap. 4.

The Boltzmann plot method has been demonstrated many times and in many applications. Brown [54] demonstrates the accuracy of such a method over a flat flame burner. The measurements made were compared to thermocouple data in order to validate the method. Busa and Brown [55] continued this analysis to generate a fast data processing technique based on the Boltzmann plot method in low spectral resolution data. Busa et al have also demonstrated this technique in a direct connect hydrocarbon fueled scramjet to determine temperatures and mole fractions.

Lindstrom et al [56, 57] describe the application of the Boltzmann plot method to shock train structure in their two part papers, detailing the system design and validation and the analysis and CFD comparison. The experiments demonstrated good agreement with past data and is able to be miniaturized such that it can be

flight ready, whereas more traditional optical techniques such as Schlieren particle velocimetry cannot. Lindstrom et al also note some of the errors that can arise from the Boltzmann Plot method including the fact that broadening parameters for fitting spectral line shapes can be missing and that errors can be propagated through the analysis.

Sappey et al [58] have used the Boltzmann plot method for measurements in turbine engines. They also reference the fact that temperature non-uniformity can cause the slope of the Boltzmann plot method line to curve because different lines may have different temperature sensitivities. This curvature can be used to demonstrate that a gas flow does not have a spatially uniform distribution of temperature, or it varies over time.

The Boltzmann plot method has also been demonstrated in plasma emissions in addition to absorption spectroscopy for combustion measurements. Many papers are found demonstrating the same analysis technique used in plasma dynamics research, such as Ar-N_2 plasmas [59], CF_2 plasmas [60], and CO [61] plasmas among many others. These measurements are frequently used to obtain electron temperatures from emissions, where the derivation of the Boltzmann plot method is completed for the emission terms of the equations, rather than for the absorption terms. These measurements demonstrate that the Boltzmann plot method, with the correct derivations, can be applied in many scenarios, not simply for combustion research with isolated absorption spectra.

The current state of the art sources demonstrate the ability of the Boltzmann plot method to be used to reconstruct temperatures and partial pressures in a wide variety of test cases. Each of the lines probed in these measurements is an isolated spectral feature used in order to fulfill the requirements of the Boltzmann plot equation, which needs a lower state energy value from a given transition. This limitation, requiring that isolated transitions be measured, is inherent in the traditional Boltzmann plot

method approach.

1.6.3 Wavelength Modulation Spectroscopy

Wavelength Modulation Spectroscopy is the next step up in complexity from SWDAS, which imparts a second and much higher scanning modulation frequency on top of the slower scanning wavelength.

The modulation introduces harmonics into the signal, which are typically of a much higher order than any noise and neglects random shot noise, which has no set frequency. These harmonics can be captured with a lock in amplifier to obtain an effectively noise free signal. This is one of the biggest benefits of using WMS techniques.

To process WMS data, fitting algorithms have been developed for calibration free measurements. One of the more commonly used methods is the $2f/1f$ technique, where lock-in amplifiers are used to capture the first and second harmonics, which are then ratioed. These harmonics are related to the second and first derivative of the signal. These ratios give a noise free signal, which is fit in the same manner as the spectral fitting, only with the $2f/1f$ signal instead. Because it is a fit, this method is still susceptible to errors in the spectral databases, although it is relatively noise free. A second drawback is the cost and scale of the instrumentation necessary to make this technique useful. In order to obtain these measurements, high frequency TDLs and detectors are necessary. Additionally, at least two lock-in amplifiers must be used to obtain the $2f$ and $1f$ signals for the calibration free, noise insensitive measurements. These instruments are costly and also bulky, making real time, in situ flight ready measurements an ill fit for this technique. Finally, the processing times for such a technique are long, meaning that real time measurements using WMS are challenging, if not impossible, with current equipment and computing devices. This method has been tested in high temperature applications, but is still undergoing research into

how it can be applied to high pressure cases, and other cases where transitional lines are heavily blended.

WMS is frequently used to obtain high SNR, noise insensitive measurements. These were described by Rea and Hanson [62] as a way to discriminate against broadband background signal. Hanson's group has since continued to pioneer the use of WMS in order to obtain accurate measurements, applying them to scramjets [63, 64, 65, 36], rotating detonation engines [66], boiler exhaust in coal-fired electric utilities[9], and internal combustion engines [67]. These applications are often noisy and require a method for background noise reduction. The WMS techniques are useful for obtaining signal without this background noise. It is noted that the measurements are best fits to the datasets using spectral databases in these works. Additionally, the instrumentation must be able to be rapidly tuned so that the important information is captured. For high speed applications such as the RDE, this requires scanning rates of 112 kHz [66], which requires special TDLs and the lock-in amplifiers.

WMS has also become a more prevalent method of data collection, being investigated by Fulge [68]. Their work analyzes the accuracy of the WMS technique in measurements over a McKenna flat flame burner. The work concludes that the WMS signals are accurate, but the specifications for the molecular transitions used needed further research, demonstrating the necessity of good spectral database parameters for accurate measurements.

Sappey et al [69] demonstrate some of the limitations in the WMS technique for flight-ready hardware. WMS was considered versus direct absorption for the application of a flight sensor for the HIFiRE hypersonic vehicle test. Both the WMS technique and the direct absorption technique were considered, but due to processing constraints, the direct absorption system was chosen. This was because of the higher calculation cost of the WMS technique.

Finally, WMS-2f has been demonstrated in tomographic applications [70] in which WMS-2f was used to reconstruct temperature and mole fraction distributions over a radially symmetric flame. This demonstrates the power of the WMS technique, in that it is possible to make use of it, even in tomographic measurements.

From these sources it is evident that the WMS techniques are becoming widely applicable in aerospace measurements. However, there are still advances to be made. Errors include the necessity for accurate database parameters, fast tuning lasers and detectors, and the specialized equipment necessary to obtain the data. While this technique is accurate, it is not always the best choice, leaving gaps in its applicability.

1.7 Gaps in the Current Knowledge

Although TDLAS has been developed and successfully applied in different forms to a variety of problems for more than 40 years, there remain significant limitations on the spatio-temporal resolution of measurements as well as their precision and accuracy. These gaps occur within a number of areas in the field. These gaps include: (1) tomographic reconstruction resolution, (2) accuracy and precision in measurements, and (3) robust measurement techniques for high varying flow conditions. First is the tomographic instrumentation techniques, which lack either spatial or temporal resolution. To gather measurements at multiple spatial locations, these tomographic methods have been applied, but are not able to fully resolve both time and space within a flow. Limitations on resolution are mainly associated with existing hardware, although the diode laser technology for telecommunications applications is in continuous evolution. Second, measurement accuracy is limited by several factors, such as signal-to-noise, background rejection, laser response calibration (e.g., baseline measurement) and wavelength registration, line blending effects, accuracy and availability of spectroscopic information on absorbing species. Measurements with low SNR result in poor precision of the data. background noise and laser response cali-

bration can skew inferred flow properties, resulting in lower accuracy. Line blending effects can cause processing techniques, such as the Boltzmann Plot, to fail. Additionally, lack of availability and accuracy in the spectroscopic information of absorbing species can cause models used for spectral fitting to be poorly fit. Thirdly, there exist a gap in the application of robust measurement techniques over rapidly varying flow fields measured with low sampling rate instrumentation. Current state of the art techniques require specialized instrumentation and large amounts of processing power and time. In order to obtain flight ready systems, property inference methods need to have higher spatiotemporal resolution, insensitive to poorly fit baselines and spectral parameters, and have the ability to function over varying flow fields such as those that might be seen in the operation of an engine, from start to shutdown.

State of the art tomographic instrumentation techniques are limited by temporal and spatial resolution. It is possible to obtain high resolution measurements in either space or time, but currently, obtaining both is a large challenge. Commonly, two methods for obtaining tomographic measurements are employed. The first uses a movable laser system, which are set up to scan a laser through different regions in an experiment, taking data at each individual spatial location. This allows for very high spatial resolution to be obtained, but the time resolution is dependent on the speed with which the system moves and the time it takes to acquire the data. The second type of setup passes several laser beams through a system simultaneously, allowing for several measurements to be made at once. This has very high temporal resolution, only limited by the data acquisition time. However, such systems require large amounts of space and are limited to the resolution allowed by the physical size of the experiment and instrumentation. These two techniques for tomography, while providing vital insight into the operation of engines and experiments, lack the spatiotemporal resolution necessary to fully quantify the flow field. The movable system gives a time averaged reconstruction of the properties of the probed experiment.

While useful, this does not give insight into the rapid variations in an experimental configuration in time. This can cause a loss in the measurement of time fluctuating structures in an experiment. The edge boundary of a turbulent flame would not be resolvable, for instance, but rather, an average value for the the flame as it varies in time would be obtained. The second method, using several simultaneous measurement probes, loses spatial resolution and accuracy due to fewer pitched lines. While again providing insight into the overall flowfield, and even possibly resolving temporal fluctuations within said field, the measurements of fine structures within the field can be lost. Because the instrumentation has a finite physical size, this technique must infer the flow properties along these lines and interpolate between them. This can lead to a loss of the fine structures within an experiment, such as spatial deviations in an engine measurement, or turbulence in a wind tunnel measurement. These losses in resolution can impair the capability a measurement technique to completely characterize an experiment and can cause important information to be missed. These techniques need to be improved in order to more full extend the capabilities of such measurement systems.

Many TDLAS measurement techniques rely on accurate measures of absorption profiles, such as FWDAS, SWDAS, and the Boltzmann Plot method. However, as stated by Li, Spearrin, and Arroyo [41, 39, 34], errors within baseline measurements can skew the results of measured fluid properties. As will be discussed later in Chapter V, small offsets in the baseline measurements can skew results in the reconstructed temperatures by up to 10% for strong transitions and higher than 50% for weak transitions. One method to avoid these baseline errors is through the application of WMS, where the effective derivative obtained through the second harmonic minimizes the errors due to the baseline. However, this technique requires specialized equipment and extended processing times. For instrumentation with low sampling rates, such as the LAC, WMS is not necessarily a possibility as an inference technique. For

these instrumentation techniques, the characterization of the laser system within an experimental configuration needs to be completed. This means that great care must be taken when performing calibration of the laser system. It is not always possible to calibrate the instrumentation in a manner that results in a baseline measurement of adequate accuracy. Errors arising due to these inaccurate baseline measurements can lead to incorrectly inferred properties. A better method for minimizing this baseline error needs to be obtained in order for more traditional TDLAS techniques to benefit from it.

Fitting techniques also are notoriously challenging methods for the reconstruction of pressure. The offsets from the baseline coupled with the poor sensitivity of the spectral fitting method to small variations in the shape of the spectral profile result in measurements where the temperatures are often fairly well measured, but the inferred pressure can vastly differ from the true pressure value. Again, WMS provides the sensitivity to these variations with low input from noise. However, as discussed, WMS measurements are not always feasible within certain experiments or instrumentation techniques. In these situations, it would be beneficial to obtain the sensitivity of the WMS method without the need for high sampling rates, while still employing a spectral fitting method for its simplicity as an inference technique.

Additionally, errors in the spectral databases, from missing broadening parameters to missing transitions, can cause errors within measurements. Spectral databases are consistently being updated to include spectral transitions and new and more accurate parameters as data becomes available, and many researches perform their own experiments to determine the accurate values themselves [34, 38]. However, when using the current databases to obtain measurements in flows without the proper broadening parameters, errors in measured temperatures can be up to 15% as seen in Chapter V when using fitting schemes. The Boltzmann Plot method avoids these database induced errors through the use of the integrated absorbance of isolated

spectral features. The necessity for the use of isolated spectra can make measurements in high temperature and pressure cases challenging, where these isolated features become rare. It is precisely in these environments that novel property inference techniques need to become more functional, as these are the environments in which much aerospace research is currently being conducted. As ramjets, scramjets, and RDEs become more prevalent, the application of the Boltzmann Plot method becomes more challenging in research. These engines operate in conditions in which pressure broadening and high temperature transitions cause the previously isolated transitions to begin to have interference. In order to make the Boltzmann Plot method more robust and functional in these experimental configurations, this isolated transition limitation needs to be overcome.

State of the art processing techniques cover a wide variety of test cases, but none of them work in all regimes. Indeed, there are still regions of interest in which none of these techniques can provide fast and highly accurate data. High pressure experiments and experiments in which there are varied conditions cause these processing techniques to fail. This needs to be rectified as aerospace applications move into higher pressure and wildly varying flow field conditions in experiments such as scramjets, ramjets, and RDEs. Additionally, the need for flight ready systems is rising. As these experiments progress into more fully realized and flight capable engines, the testing and processing of these engines needs to grow more sophisticated as well in order to keep up with the demand in speed, accuracy and processing capabilities of the measurement techniques.

1.8 Thesis Objectives and Novel Contributions

The objectives and contributions of this study are:

- Investigate the use of digital imaging instrumentation and techniques with TD-

LAS methods to extend TDLAS from path-integrated point measurements to planar measurements. Extending TDLAS from single point to planar measurements will provider higher simultaneous line-of-sight spatial density in TDLAS measurements and, if combined with tomographic methods, will enable more robust uses of tomography.

- Develop and demonstrate methods based on derivative co-fitting capable of rejecting baseline errors in scanned direct absorption. These methods can be used to increase the accuracy of TDLAS measurements based on scanned direct absorption similar to the benefit that wavelength modulation provides.

- Extend the Boltzmann plot method to account for line broadening and blending effects, which are effects that currently limit the accuracy and application of the Boltzmann plot method. This method, which is here called the Aggregate Boltzmann plot method, allows for accurate temperature and absorption species mole fraction measurements under conditions that would otherwise not be possible, such as at elevated pressure and temperature conditions.

- Combine the baseline error rejection methods with the Aggregate Boltzmann plot method into a robust spectroscopy tool for the accurate measurement of temperature at high pressure conditions in combusting environements.

A novel instrumentation technique making use of a Linear Array Camera (LAC) is tested and applied. This camera is an InGaAs linescan camera and able to simultaneously sample high resolution spatial information through reading a laser sheet across it's array of pixels. The LAC is sensitive in the near infrared (NIR) range from approximately 1000 nm to 1600 nm, with a maximum scanning rate of approximately 92,000 Hz. This laser wavelength range is convenient due to easily accessible, off the shelf components that exist for this range. This camera will allow for some of the spatio-temporal resolution problems in the current research to be closed with a single,

convenient detector for line of sight (LOS) measurements. This is a benefit over the current methodology, which employs either simultaneous, yet low spatial resolution sampling, or non-simultaneous, high spatial resolution sampling. With the LAc, both the fine spatial structures, as well as the temporal structures within a flow are able to be characterized. This measurement technique has applications not only in resolving LOS measurements, but also has possibilities as a powerful tool for tomographic measurements once fully functional.

Several design challenges exist for the LAC including etalon noise, vibrational noise, and beamsteering. These challenges will be described and corrections for the etalon noise and vibrational noise will be determined. Beamsteering still presents a challenge for the LAC, which needs to be overcome to make this technique fully viable for flame applications. In addition to the design challenges, other issues which plague traditional measurement techniques affect the LAC. These include baseline and spectral database errors, which have the capability of causing inferred flow properties to have errors as well.

The processing techniques which can avoid baseline issues altogether, namely WMS methods, are not feasible for an instrumentation system with a sampling rate of only 92 kHz for acquiring high speed data. Additionally, in order to provide rapid measurements of inferred flow properties, WMS is not an ideal solution due to computation costs. In order to provide rapid, baseline insensitive measurements, a second derivative fitting scheme is explored, which is analogous to WMS $2f$ fitting techniques, but applied in wavenumber space, rather than Fourier space. While this is not the first application of second derivative fitting to spectra in research, this work does represent the first application of the second derivative method to highly resolved spectra in order to obtain baseline error rejection. Previously literature applies the second derivative fitting to many broadband measurements made in organic chemistry and biology as well as an application for broadband spectral measurements in flames.

The technique is used to increase sensitivity to small variations in measured spectra, which allows it to capture data that is otherwise lost in the wings and blended spectral features. Measurements have been made of line shape profiles of isolated transitions. However, in addition to he increased sensitivity to small variations in curvature of spectral profiles, the method also generates insensitivity to baseline offsets and curvature errors through minimizing these effects on the inferred fluid properties. The use of the measurement technique in this work will apply the second derivative fitting to highly resolved spectral features and make use of the baseline insensitivity in order to regain some of the benefits of WMS $2f$ methods without the necessity for high sampling rates and processing times. This will allow for the LAC, as well as other bandwidth or sampling rate limited instruments, to obtain accurate and rapid measurements in the face of baseline errors. Additionally, the increased sensitivity to the spectral variations will allow for very accurate measurements to be made of the pressures, which is a challenging flow property to be inferred using traditional fitting techniques.

The second derivative fitting, while insensitive to baseline errors, is susceptible to database errors which are necessary in fitting schemes where the lineshape function must be well approximated. As described, the Boltzmann Plot method, through the use of integrated absorbances, can avoid the issues with missing database broadening parameters. However, the Boltzmann Plot as described is limited by the necessity for isolated spectral features. These become increasingly rarer as temperature and pressure increase, which make the Boltzmann Plot method less feasible in these ranges. This is problematic for measurements in systems such as ramjets, scramjets and RDEs, where the inherent operating conditions of these systems occur in high temperature and pressure regimes. In order to overcome this limitation, the equations for the Boltzmann Plot method are rederived using the concept of aggregate spectra taken from Caswell [71]. Aggregate quantities are described as weighted val-

ues for normally isolated spectral quantities such as the lower state energy and the linestrength. Through the use of these aggregate quantities and slight variations on the traditional solution algorithm, the Aggregate Boltzmann Plot can be applied to blended lines as well as isolated lines, allowing for measurements which are insensitive to errors in the broadening parameters of the spectral databases while allowing for any combination of blended spectra to be used in the property inference process. This not only gives a framework for applying the Boltzmann Plot to aggregate spectra, but also allow for the Aggregate Boltzmann Plot method to become a viable technique in flows with varying property conditions. This functionality arises from the ability of the Aggregate Boltzmann Plot method to work over both isolated and blended spectra. As the pressure and temperature conditions vary, the transitions contained in the window over which the laser is scanned can vary from isolated to blended spectra due to pressure broadening and high temperature transition activation. The framework of the Aggregate Boltzmann Plot method allows for these lines to vary and continue to be usable across the transitory regimes.

While the Aggregate Boltzmann Plot method does not rely on the spectral database broadening parameters, because it relies on the integrated absorbance of the spectral features, it is susceptible to baseline errors. The final contribution of this thesis will provide a combination of the the second derivative fitting and the Aggregate Boltzmann Plot, which will gain the benefits of both methods while minimizing the contribution of errors from each. This will allow for a robust technique, which is applicable to flowfields with rapidly varying conditions, which has low sensitivity to errors from measured baselines and without the need to make assumptions about poor or missing spectral database parameters. The algorithm for this combination of techniques first uses the second derivative fitting to accurately recreate the spectral feature even in the presence of baseline errors. Taking the reconstructed transition or blended set of transitions, the integrated absorbance can be obtained and used in the

Aggregate Boltzmann Plot method. Because the second derivative fitting provides accurate shapes for the transitions, the contribution of baseline errors are minimized. The Aggregate Boltzmann Plot method only relies on accurate representations of the spectral transitions, and thus the missing broadening parameters do not affect the solution of the Aggregate Boltzmann Plot method. The application of these two processing techniques in this order allows for accurate measurements to be made over a wider range of flow conditions than canonically possible with the Aggregate Boltzmann Plot method, with the baseline insensitivity of the WMS $2f$ technique, with limited systems hardware. This overarching solution allows for the flexibility of both methods, while retaining the simplicity of the typical spectral fitting and Boltzmann Plot methods. This allows for a simple, flight ready system which can process data in the presence of baseline noise and over varying flow conditions. This process can be applied to data with sampling rates far lower than the requirements of WMS, leading to a robust measurement technique that will function over not only a wide variety of flow regimes, but also in flow regimes which have varying conditions over the testing time. A good example of this is an RDE system, in which the detonoation wave passes with very high temperature and pressure values, and then returns to nearly ambient conditions after the passage of the wave.

CHAPTER II

Description of a Linear Array Camera for Planar Absorption Measurements

2.1 Linear Array Camera

The Linear Array Camera (LAC) will be discussed in this chapter. The camera instrumentation will be described first, followed by noise and sensitivity analysis, which will be developed and shown. Common issues will be described and possible corrections for these issues will be noted and demonstrated in tabletop measurements. Finally, the LAC will be demonstrated as a promising measurement technique in a low pressure cell, demonstrating that simultaneous, high spatial resolution measurements that can be obtained. This method is denoted as the Planar Tunable Diode Laser Spectroscopy (PTDLAS) technique. The PTDLAS technique will fill in the gaps left by current measurement techniques used to obtain resolved data in a flowfield. These techniques include the scanning system, which resolves spatial data at the cost of temporal resolution, and multi-laser systems, which take simultaneous measurements at the cost of tspatial resolution. These techniques each have their own benefits, but the drawbacks of each is the lack of a robust technique to obtian high spatial measurements simultaneously. This LAC system will allow for 25 μm resolution in space over the width of an inch, with each 25 μm pixel being sampled simultaneously.

This will allow for the resolution of temporal variations as well as spatial variations within a flowfield. These measurements will be able to more fully characterize a flow in both time and space, than what was previsouly possible.

2.2 The LAC Optical Setup and Operation

The LAC itself is the SU1024LDH2, a small cubic camera that contains a single inch long array of 1024 pixels as seen in Fig. 2.1. These pixels are 25 μm in width by 500 μm in height, allowing for very dense sampling of the measurement space. The camera is sensitive in the Near Infrared (NIR) optical range, wavelengths between approximately 1000 nm to 1600 nm, perfectly suited for capturing isolated spectral transitions of H_2O, an important molecule in combustion measurements. In laser measurements, where a beam is passed through an absorbing medium, the beam must be passed through a set of pitching optics and received on the other side with a set of catching optics. In traditional single line measurements, these are usually single beam collimators and collection lenses, a schematic of which is seen in Fig. 2.2(a). An example of a single beam scan is seen on the right hand of the image, measured only through the path which the single beam takes. However, in order to obtain these linear measurements for the LAC, the pitching setup must be accounted for. In lieu of traditional laser beam collimation optics used in TDLAS measurements, the LAC experimental setup makes use of sheet-forming optics to generate a collimated, planar laser sheet. This sheet is then passed through the test gas, which absorbs light along the path of the laser sheet. The sheet impinges on the LAC detector face and is measured and the images are obtained with an NI PCIe-1427 framegrabber. This experimental setup is shown in Fig. 2.2(a), with a measurement image shown on the right hand side of the figure. This image represents measurements made simultaneously over a region of space, where each pixel in the linear array gives a measurement scan and will be further discussed later in the chapter.

Figure 2.1: The SU1024LDH2 Linear Array Camera usind in the spectral imaging experiments.

The sheet forming optics consist of two pairs of anamorphic prisms. These prisms both have a ratio of expansion of about one to four, meaning that the 2 mm TDL beam expands to about 25 mm, enough for the laser sheet to cover the linear array of pixels on the LAC. One pair of these prisms was purchased from Thorlabs directly, but in order to expand the beam to the full one inch width, the second set of anamorphic prisms were custom manufactured. The Thorlabs prisms are about 14 mm in length and so cannot be used twice to obtain the full expansion. The custom lenses are approximately 38 mm in length, leaving ample room for the full expansion of the laser beam. The catch optics have two configurations depending on the experiment. In one configuration, there is a cylindrical collimation lens to focus the laser sheet down onto the LAC detector face. This has the benefit of increasing the SNR in a stationary experiment, but if there are structural vibrational effects present this can instead increase the noise. This will be discussed in a further section. The second configuration is used to combat this vibrational noise and does not include

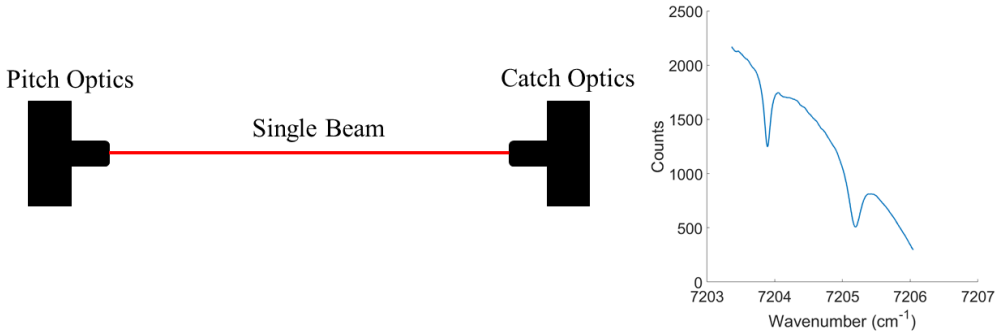

(a)

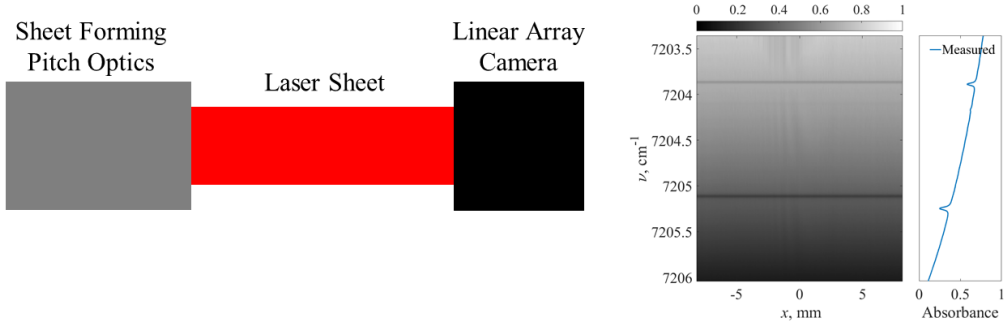

(b)

Figure 2.2: Raw image (a) and shift needed for correction (b) of the in plane vibrational noise.

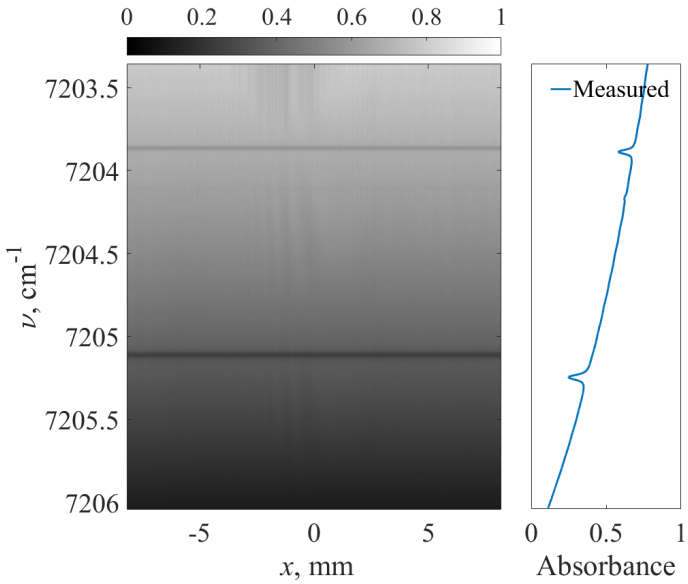

Figure 2.3: Example of an image captured by the LAC, where the x-axis is location and the y-axis is wavenumber. The image is rendered through acquiring single spatially resolved line images and "stacking" them to form the LAC image, where each pixel gives a time trace of the laser scan, and time is converted to a change in wavenumber.

the collimating lens.

The LAC acquires data by taking snapshots of the spatially resolved laser sheet in time and "stacking" them vertically to generate a two dimensional image. The x-axis of the image represents the spatial distribution of pixels, while the y-axis, taken in time, can be converted to wavenumber through the application of a solid etalon. This image is seen in Fig. 2.3. In this image, each x-location pixel gives an absorbance scan as seen at the right hand side of the image.

Applying Beer's Law to each of the pixels in the image taken by the camera gives what will be referred to as a spectral image, as seen in Fig. 2.4. This image a two-dimensional representation of the spectrum measured by the LAC, where each pixel gives an absorbance profile. The average of the absorbance profiles in this image is seen at the right hand side of the image. Because the pixel density is 1024 pixels per inch, then the LAC setup is able to obtain 1024 of these absorption scans per inch

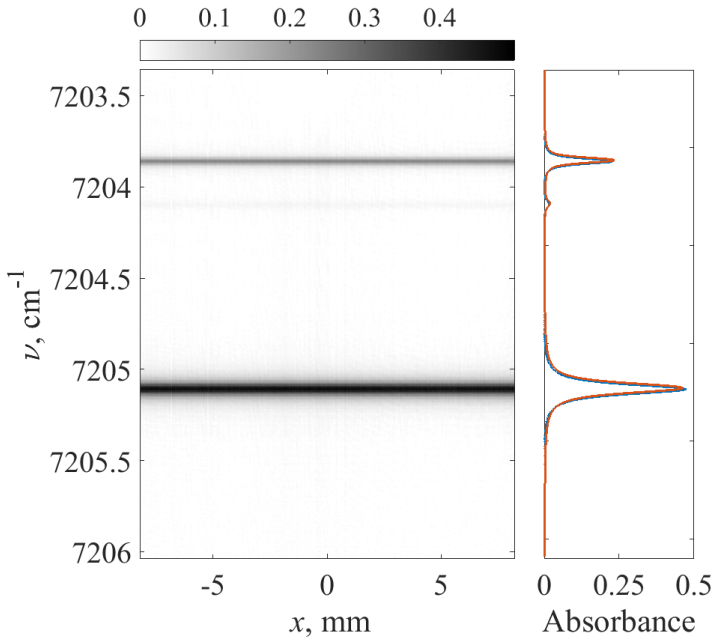

Figure 2.4: Example of the spectral image corresponding the image taken by the LAC in Fig. 2.3. The average absorbance of all the pixels is seen at the right hand side.

during measurements.

2.3 Common Problems and Corrections with the LAC

In any novel instrumentation technique, there are unexpected issues which arise. These must be corrected for the technique to be viable in systems applications. This section of Chapter 2 will describe three issues faced when implementing the LAC instrumentation system, and propose corrections for fixing these issues. The three problems to be described are etalon interference noise, vibrational noise, and beam-steering.

2.3.1 Etalon Interference

Etalon interference is a commonly addressed issue in traditional single beam TD-LAS measurement techniques, and occurs when two parallel surfaces form a resonance

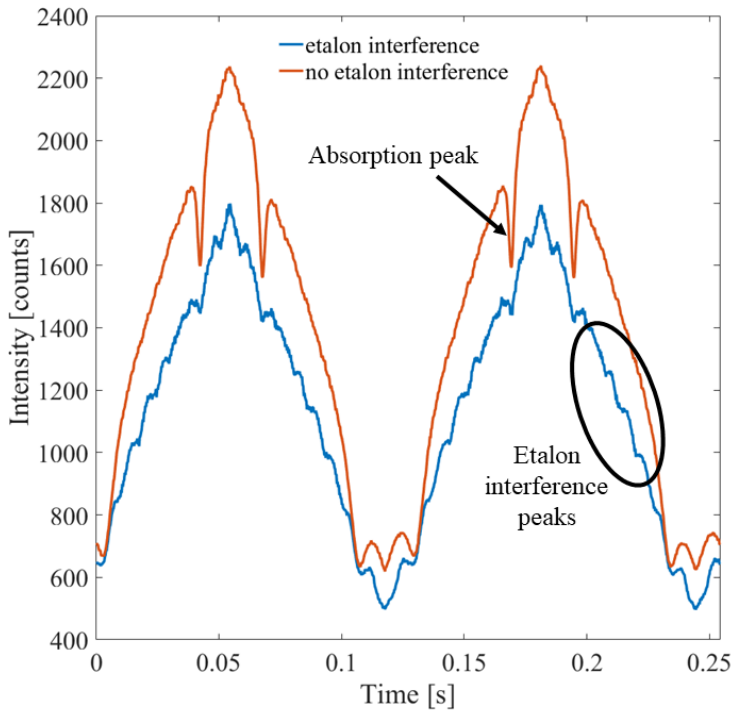

Figure 2.5: Scan of room air taken with and without etalon interference in the signal. The etalon peaks are on the order of magnitude of the absorption signal, causing large errors in the measure properties. The loss in the signal is due mainly to the introduction of the windows which are inducing the etalon effects.

cavity where beam reflections cause constructive and destructive interference patterns in the signal. These patterns are well understood and are a function of the reflectance of the walls of the cavity, the length of the cavity, and the index of refraction of the material. An example of an etalon interference signal is seen in Fig. 2.5. The etalon interference patterns are of the same order of magnitude as the absorption peaks, which can introduce large errors into the measured properties.

2.3.1.1 Etalon Equations

Etalon signals are well understood. The spacing between the peaks is called the Free Spectral Range (FSR) and is a function of the length of the resonator cavity and the index of refraction of the etalon material. The equation to determine the free

spectral range is seen below,

$$\Delta\nu = \frac{c}{2\eta_g L} \tag{2.1}$$

where $\Delta\nu$ is wavenumber spacing measured from peak to peak. The speed of light is denoted by c, while L is the length of the resonator cavity. The index of refraction, η_g, also affects this spacing, where the higher the index is, the wider the spacing between etalon peaks, or the higher the FSR of the etalon signal.

The width of the peaks themselves are called the finesse of the etalon signal. This is given as the the FSR divided by the Full Width at Half Max (FWHM) of the signal. This is given in the following equation:

$$F = \frac{\pi}{2\arcsin\left(\frac{1-\sqrt{\rho}}{2\sqrt[4]{\rho}}\right)} \tag{2.2}$$

Here, F is the finesse of the signal and ρ is the fractional amount of power left in the resonator cavity after one cycle, i.e. $1-\rho$ is the loss through one cycle. These two parameters, the FSR and the finesse, define the shape and spacing of the etalon interference signal that appears in the scan.

In TDLAS, etalon references are used to transform the time signal of a scan into wavenumbers through obtaining the peak to peak spacing and converting this spacing to a variation of the scan in time to a variation of the scan in wavenumber. This allows for a simple reference when measured. However, when the etalon signal is unintended, it causes negative effects in the measuremetns.

2.3.1.2 LAC instrumentation Etalon Issues

The initial beam shaping system for the LAC was generated from off the shelf Thorlabs components in order to make an economical and fast setup system. A fiber coupled TDL was passed into a collimator which was mounted on one inch optical mounts. A series of plano-concave and plano-convex Near Infrared Anti-

Reflection (NIR AR) coated cylindrical lenses were mounted inside a lens tube, which was attached to the same optical mount. This lens tube had an N_2 purge line attached to get rid of unwanted atmospheric H_2O absorption. However, despite the AR coating, the flat faces of these lenses create an optical cavity where the generated laser sheet can resonate. This introduces etalon interference into the laser sheet signal. This additional etalon signal in the measurements causes errors in the reconstructed flow properties, and must be minimized in order to obtain accurate measurements. A second optical setup was created to generate a laser sheet without the interference of these etalon peaks.

The second system that was tested made use of a set of anamorphic prism pairs. The configuration for these prism pairs is seen in Fig. 2.6. These anamorphic prism pairs act as sheet forming optics and spread the beam by a factor of four times per pair. This takes the approximately 2 mm laser beam into approximately 1 inch collimated laser sheet, which fills the LAC detector face. As can be seen in Fig. 2.6, the presence of resonance cavities within the sheet forming optics has been completely removed, and so there are no etalon interference signals present in the laser sheet due to sheet forming optics.

In order for these prisms to work properly, careful effort must be taken in the size and arrangement of these prisms. First and foremost, the input beam and output laser sheet need to be collimated. This allows for the path of the spatially distinct regions of the spectral images to be well characterized. The expansion of the beam should properly fit within the faces of the prisms. If the prism face is unable to collect and transmit the laser sheet properly, reflections and losses can occur. In the system described here, one set of prisms was available off the shelf from Thorlabs, but the output face was too small to accommodate the final width of the beam after the second expansion, this the second set of prisms was manufactured. The arrangement of these prisms is critical to the successful expansion of the laser beam.

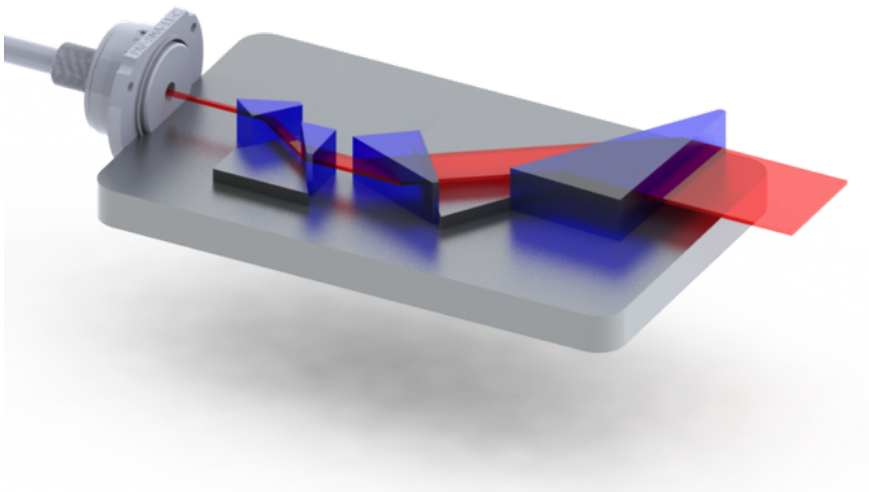

Figure 2.6: Anamorphic prism pair setup in order to generate an etalon free laser sheet. The angles of the anamorphic prisms both act as sheet forming optics as well as completely removing back reflections within the sheet forming optical setup.

By adjusting the angle of the prism itself and the angles of the prisms relative to each other, the width and output angle of the beam can be tuned. The setup generated here uses 30°angled prisms, with a system of pins to reference and locate the angles of the prisms relative to each other. Additionally, the material for the prisms is a necessary consideration. As with and laser application, the index of refraction must be accounted for over the range of the laser wavelengths being used to probe the transitions. In this work, the prisms were made with N-SF11 glass and coated with anti-reflective coating over the probed wavelength range. Lastly, the case itself needs to be airtight and purgable. The length of the optical path within the arrange contains non-negligible amounts of space where absorption can take place outside of the ideal measurement range. In order to prevent contamination, the prism arrangement is housed inside an N_2 purgable box, which prevents ambient absorption before the laser sheet is fully expanded.

2.3.1.3 Experimental Setup Etalon Issues

In addition to the etalon signals that can be introduced through the LAC instrumentation setup, the experimental configurations can also cause etalon interference to be present in the measured signal. Again, this is a well understood problem in traditional TDLAS. In single beam measurements, if two windows are parallel and the beam is passed through the windows along the normal to the parallel planes, the experimental windows create a resonance cavity. This can cause the measured signal to have etalon interference errors. Two common workarounds exist to this problem, the first of which is using a wedged window to alleviate the etalon interference [72, 36, 66, 73]. This works on the same principle as that introduced by the anamorphic prism pairs. The reflections off of the wedged face move in a difference direction than the beam, removing the etalon interference from a signal. While this is a simple method for the removal of etalon interference, it is not always possible to include wedged windows into an experimental design, or to retrofit an older experiment with wedged windows. A simple example of this would be an optically accessible wind tunnel, where the walls of the tunnel are long panes of glass. In cases such as these, passing the beam through the glass panes at an angle has the same effect as using a wedged window. The back reflections off of the angled face of the glass allows for the reflections to pass at a different angle removing the resonance cavity that forms when the beam is passed at a normal direction.

Because the PTDLAS method is extended in a dimension, these methods are also vulnerable to noncollinear etalon effects. This is due to the presence of possible back reflections along the laser sheet, where the sheet can interfere with itself. This case arises whenever the planar sheet is parallel to the plane made by the angle of incidence of the laser sheet and the normal vector to the window. A schematic of this can be seen in Fig. 2.7.

As shown in this figure, the back reflections along the plane of the laser sheet can

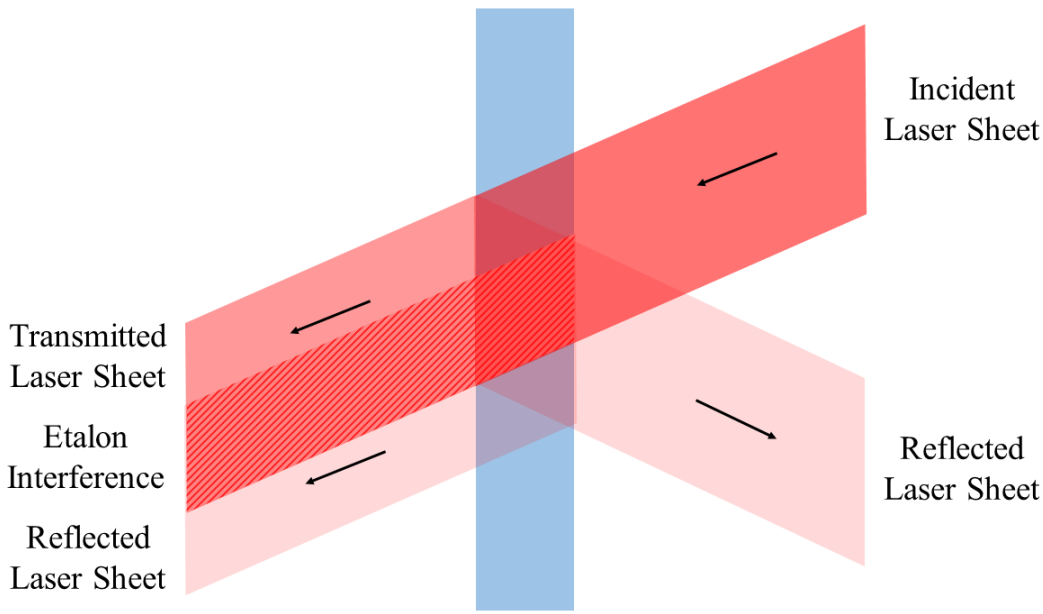

Figure 2.7: Schematic of an etalon interference region due to reflections of the laser sheet off of the windows.

cause etalon interference with the sheet. This is mitigated by rotating the laser sheet about the vector along the angle of incidence. As long as the sheet is not parallel to the plane made by this axis and the normal vector to the window, the reflections from the laser sheet will not interfere. Because the interference can cause large errors in the measurement, great care needs to be taken in ensuring that these back reflections are not present in the system.

2.3.2 Vibrational Noise

A second major issue with the LAC system is the sensitivity to structural vibrations in the LAC mounting system. As with etaloning inherent in a system, vibrational effects are often present in single beam measurements [37, 41]. However, in single beam measurements, these effects are quite easy to deal with[74, 67]. A collection optics assembly can be placed in front of the detector face to gather the light

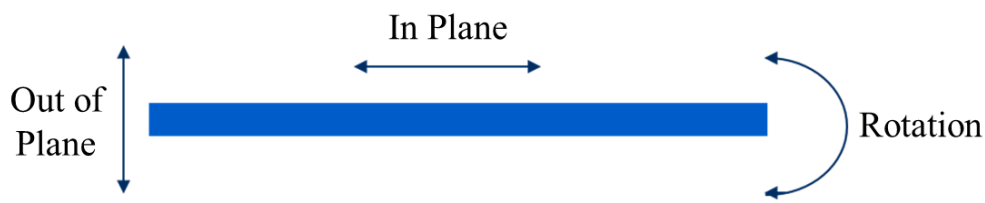

Figure 2.8: Schematic demonstrating the various vibrational motions observed in the LAC data. The motions are in plane, where the pitch angle changes in the plane of the laser sheet, out of plane, where the pitch angle varies out of plane, and rotation.

from a wandering single beam and funnel it to the detector. Because the LAC images laser sheets, this solution does not work well for the LAC system. The pixels in the LAC array are 25 μm by 500 μm. Due to the small size of each cell, small changes in the pitch angles can induce large variations in the intensity levels measured by the LAC detector. As seen in Fig. 2.8, there are three different vibrational modes. The first mode is the in plane motion, where the pitch angle varies in the plane of the laser sheet. This results in shifts along the pixels on the LAC. The second motion is an out of plane angle change where the laser sheet moves in and out of the laser sheet plane. This results in an intensity change during the scan as the sheet moves across the pixels. The final mode is rotation, which manifests as a combination of the two other motions, and is rarely seen.

These vibrational modes need to be accounted for in the system. Ideally, the system would be rigid, with no vibrational effects, but this is not always possible. In order to investigate this issue, a tabletop experimental configuration was created. In this experiment, an optical rail was set up on the tabletop with both the pitch and the catch optics mounted to it. An additional plano-concave is mounted on the pitch optics to expand the beam. As the catch optics are moved along the rail, the effective Gaussian shape of the laser sheet is widened, giving a method to observe how the broadening of the Gaussian can reduce the effects of vibrations in in the

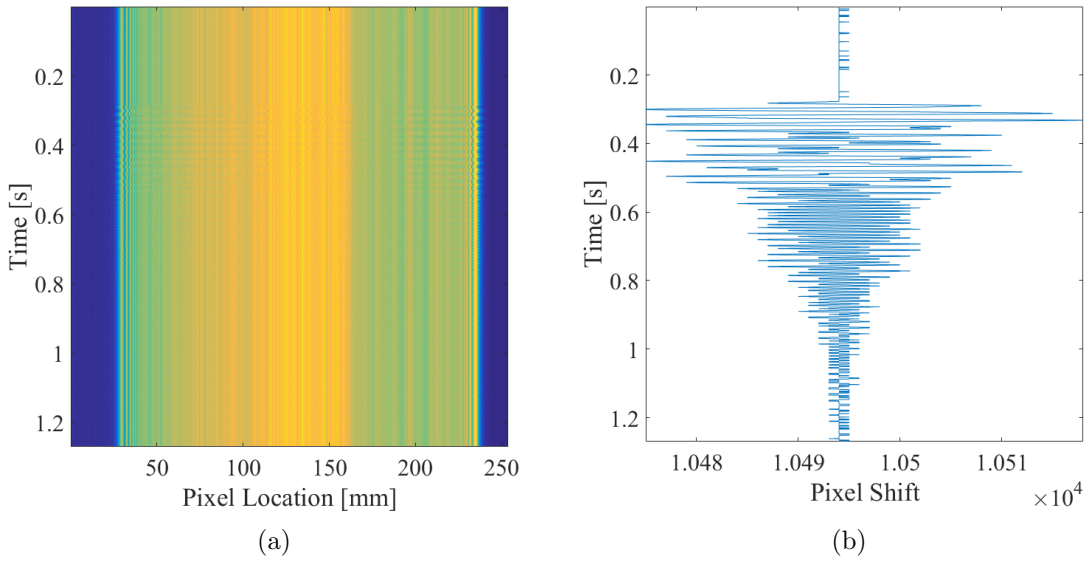

Figure 2.9: Raw image (a) and shift needed for correction (b) of the in plane vibrational noise.

out of plane direction. A striker was set up to impart a mechanical impulse on the tabletop. The catch optic was moved along the optical rail and images were taken during an impulse from the striker, resulting in an image that had contamination from vibrational effects. The two apparent vibrational modes arising from this experiment were an in plane motion and an out of plane motion. These manifested in the images as pixel shifting and intensity variations. The first of these, the shifting of the pixels, is very evident to the naked eye as seen in Fig. 2.9(a), near the 0.3 second time mark.

Because this shift is only in the plane of the laser sheet, correcting for this shift in post processing is straightforward. Using an edge detection algorithm to determine the rising edge of the laser sheet or using cross correlation between individual snapshots of the camera allows for fast and accurate determination of the shifting that occurred between each image taken by the camera. This is seen in Fig. 2.9(b), where the shifting of the pixels in space is given on the x-axis while the time of the shifting is given on the y-axis. Through correcting the image by these shifting amounts and realigning the image, the in plane shifting motion can be easily removed. This is

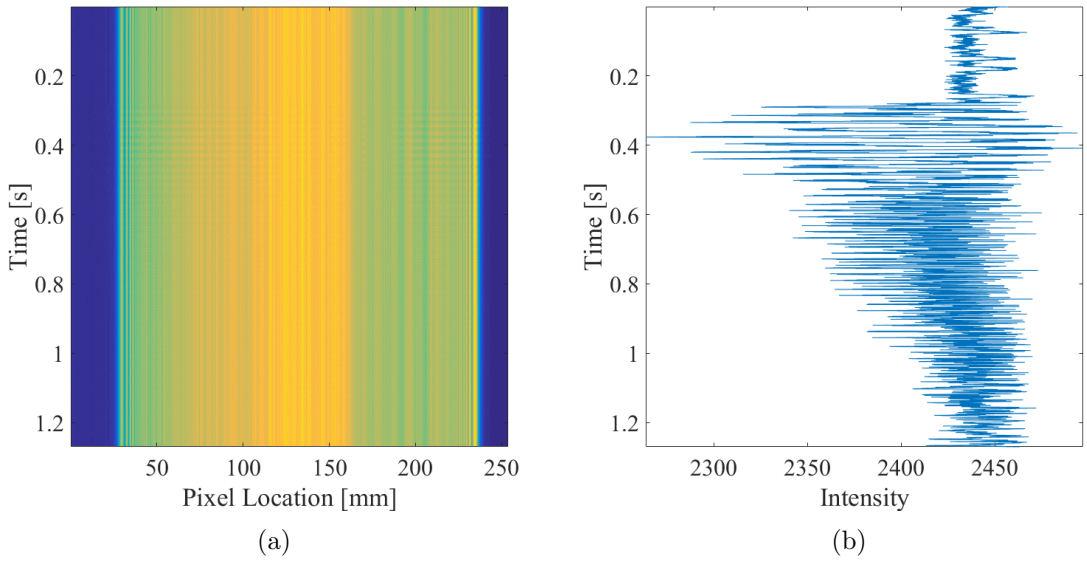

Figure 2.10: Image corrected for the in plane motion. the resulting image is left with the out of plane intensity variations, seen in (b)

demonstrated in Fig. 2.10.

As seen in Fig, 2.10(a), the realigned image no longer has the contribution of the in plane variations, but the intensity variation remains. This variation is due to the out of plane motion induced by the vibrational impulse on the tabletop, which results in the laser sheet pitching setup to vibrate in and out of the plane of the sheet. The amplitude oscillation of the image is seen in Fig. 2.10(b), where the averaged intensity variation across the image is given. The laser sheet is a Gaussian profile with the peak of the Gaussian occurring at the midpoint of the laser sheet. In order to look at the laser sheet, the LAC and the sheet were oriented at 90 degrees, such that the sheet intensity could be measured by the camera. The typical collimated laser sheet was imaged and can be seen in Fig. 2.11(a), while an expanded laser sheet is given in Fig. 2.11(b). These images were taken at a higher gain setting than the vibrational images in order to have a higher SNR in the observed laser sheet profiles. The intensity profile is given along with the Gaussian fit to that profile.

In the typical, narrow laser sheet, the Gaussian profile is very peaked. A shift in

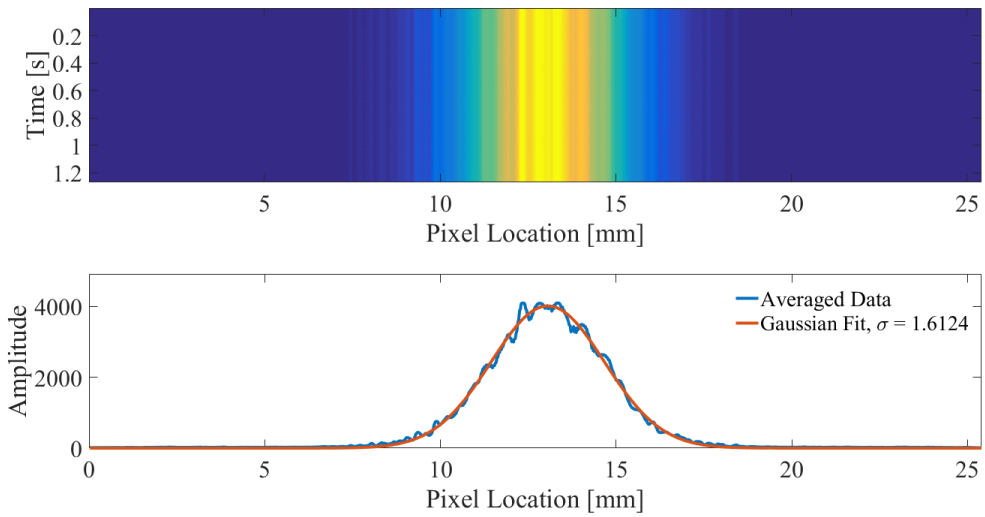

(a)

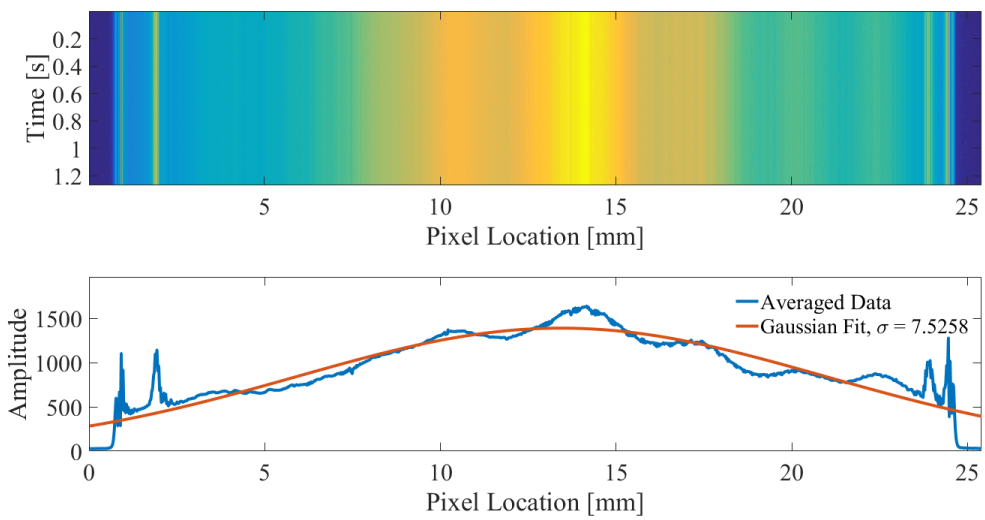

(b)

Figure 2.11: Gaussian distribution of light for an unexpanded laser sheet (a) and for an expanded laser sheet (b).

either directions from centered by as little as 1.5 mm can induce an intensity variation of up to 50%. In experimental setups where the distance between the pitch optics and the LAC is large, very small deflections in the pitch angle can have a large effect on the intensity profile seen by the LAC. A simple method for correcting this problem is not to use a narrow laser sheet. The narrow sheet was expanded through the use of a plano-concave lens, which broadened the Gaussian shape of the beam. This is seen in Fig. 2.11(b), where the standard deviation of the Gaussian of the laser sheet is approximately 5 times larger than that of the narrow sheet. As observed in the fit data, a shift of 1.5 mm in either direction of this broadened beam results in negligible intensity variations through the system. The overall intensity is lower, but with a sufficiently powerful laser, this is not problematic. The lasers used in the experiments in this work needed to be attenuated, as they were strong enough to over-saturate the LAC, and so the loss in he power of the signal accrued by spreading the beam over a wider region was tolerable.

The ability of the wider beam to negate the out of plane vibrational effects is demonstrated in Fig. 2.12, where the expanded beam was passed to the LAC and measured. After alignment of the in plane motion, and due to the broadened Gaussian, the final image is obtained and shown in Fig. 2.12(a). The intensity variation is shown in Fig. 2.12(b), where the impulsed region, this time at 0.7 seconds is effectively indistinguishable over the inherent noise variation in the signal.

The effects of the broadening of the Gaussian laser sheet compared to the deflection of the beam based on the vibrations out of plane can be reduced to a general model. The range of the deflection of the beam is given as:

$$\Delta = L \tan \theta \tag{2.3}$$

where Δ is the deflection of the centerline of laser sheet at distance L for a given

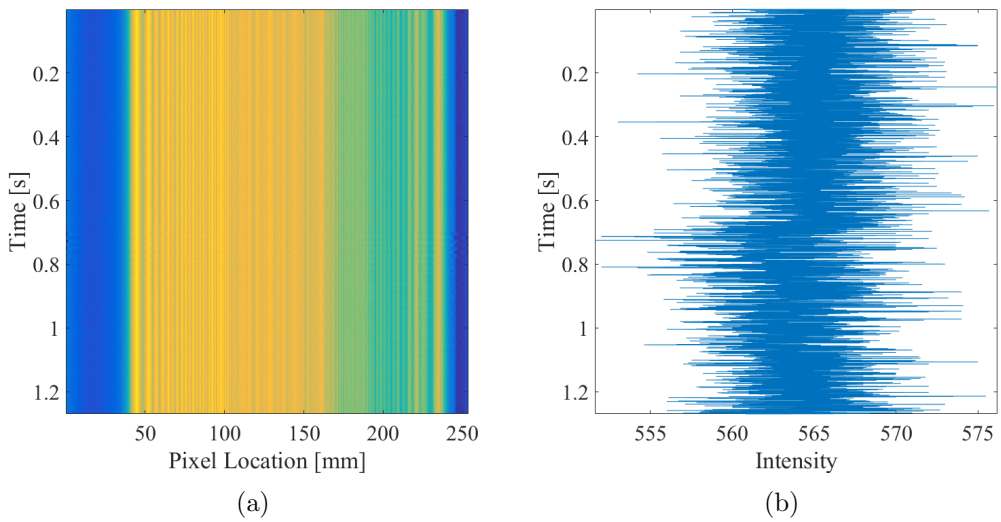

Figure 2.12: Corrected image (a) and amplitude oscillation (b) demonstrating the out of plane vibrational noise for an expanded laser sheet.

deflection angle θ. Modeling the Gaussian shape of the beam with the normalized Gaussian gives:

$$G(x) = \frac{a}{\sigma\sqrt{2\pi}} \exp\left\{-\frac{1}{2}\left(\frac{x}{\sigma}\right)^2\right\} \tag{2.4}$$

where a is a constant value based upon the integral size of the normalized Gaussian, σ is the standard deviation of the Gaussian, and x is spatial range over which to calculate the Gaussian intensity. In this model, x is the beam deflection range $-\Delta$ to Δ. This pair of equations allows for the modeling of how vibrations can be mitigated by the broadening of the Gaussian laser sheet. The solution can be optimized on a case by case basis. Typically, it would be preferable if the variation in the intensity $G(x)$ is less than the system noise as seen in Fig. 2.12. If the system noise and path length L are known, the standard deviation necessary to mitigate the vibrational effects can be determined. The equation can also be used to put bounds on the tolerances to vibrations for a given system. This model agrees with the analysis given above for the LAC images, where, for an angular deflection of approximately 0.15°, the modeled intensity variations compared to the measured intensity variations can

L [mm]	σ [mm]	δG_{model} [counts]	δG_{meas} [counts]	residual normalized by I
220	1.6	133	195	0.08
620	5.4	23	28	0.007
920	7.5	15	12	0.005

Table 2.1: Table demonstrating the modeled vibrational amplitude versus the measured vibrational amplitude for the out of plane vibrational case. Good agreement between the model and the measured cases are seen.

be seen in Table 2.1.

Through careful application and system configuration, the effect of vibrations on the LAC system can be negated. In plane vibrations are corrected in post processing by realigning the individual images measured by the camera. The out of plane vibrations are corrected through the broadening of the laser sheet. In this way, clean and accurate laser scans can be obtained.

2.3.3 Beamsteering

A third contribution of error is the effect of beamsteering on the measurement. Beamsteering is an effect of density fluctuations within an experiment, where, due to density gradients, the index of refraction varies throughout a system. As with the previous issues of etaloning and vibrations, this is a well known problem which also exists in single beam measurements[27, 63, 75]. Likewise, because of the two dimensionality of the laser sheet, it is a harder problem to overcome. In the previous two sections, the problem was described and possible corrections were given to complete the system and make it viable in certain experiments. In this section, the problem of beamsteering will be described and a possible correction will be given, but it is not an ideal solution for the problem.

The LAC laser sheet is a harder problem to overcome than traditional TDLAS beamsteering due to the two dimensionality of the sheet. Random fluctuations in density, such as those seen through a flame, can steer laser beams in different directions. With a single beam and a large enough collection optic, this is easy to rectify.

However, because the LAC uses a laser sheet, different parts of the sheet can be steered in different directions simultaneously. There are several vectors along which a beam can be steered, similar to the vibrational modes described in the last section. The sheet can move in plane or out of plane, or some combination of both. However, whereas the motion described in the vibrations section was a bulk motion with the entire plane moving, the density fluctuations vary in three dimensional space. In a flowfield such as this, different locations within a laser sheet are able to be steered independently and simultaneously. One section of the laser sheet may be moved off of the LAC detector face, which results in a measured intensity value that is much lower than is to be expected as the Gaussian beam wanders off of the detector face. Additionally, the motion can occur in the plane of the laser sheet, steering segments of the sheet in different directions. If a section of the sheet is moved along the plane of the sheet, this results in two sections with incorrect values. The first section records a lower intensity than is true, as the laser sheet moves out of that region. The pixels where the laser has been steered onto then result in a higher measurement of intensity as well. The random nature of these fluctuations is such that each region of the sheet can move in each of these directions simultaneously, resulting in a final LAC image that is very difficult to correct.

Currently, the best way to correct for these variations is based on the assumption that the density fluctuations are truly random. In this case, averaging the image should result in a measurement that is accurate. This is not an ideal solution and requires many shots of data over a long period of time. A single shot image is seen in Fig. 2.13(a). The beamsteering due to the density fluctuations is very evident, with bright and dim sections of the scan demonstrating the random density gradients of the flame. Figure 2.13(b) demonstrated the reduction in this interference with averaging. Again, the assumption is made that the fluctuations are truly random and independent. If this is the case, then the average of enough images would overcome

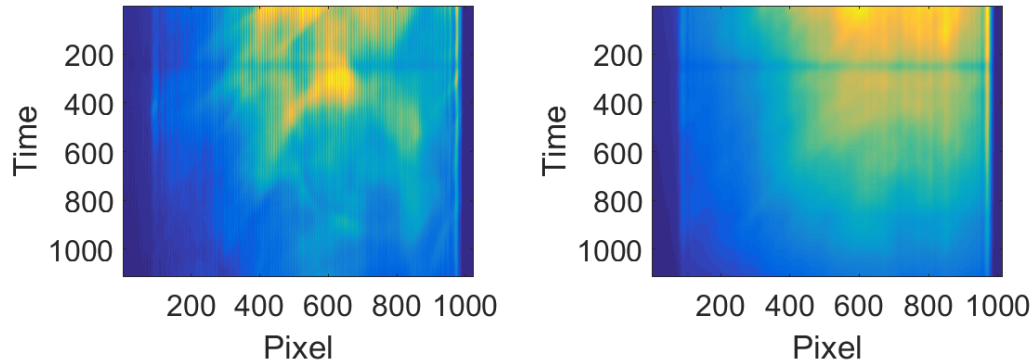

(a) (b)

Figure 2.13: Single shot image taken above a McKenna flat flame burner (a) an an average of 30 such images (b).

the random noise.

Other correction methods have been tested, including using a comb to separate segments of the laser sheet to account for wandering along the path of the pixels. This does correct for in plane motions, but does not account for out of plane motions. The correction for the out of plane motion described in the vibrations section also does not work due to the three dimensionality of the random density fluctuations. Whereas in the bulk motion due to vibrations the entire sheet moved as one due to the random fluctuations in the beamsteering, the density fluctuations are capable of having a focusing effect, where the thick laser sheet may be focused onto the LAC detector face due to the beamsteering. The current best suggested practice is to determine if the experimental system has truly random motions and use the averaging method if it does. This will allow for the averaging out of the contribution to the noise due to beamsteering effects.

2.3.4 Experimental Setup

The AC setup was tested in a 90 cm low pressure cell, of approximately 2 inches in diameter. The optical access ports to the cell consist of 3°wedged windows which are

1.5 inches in diamater, allowing for the entirety of the of the one inch laser sheet to be passed and which are used to prevent etalon interference as discussed previously. The cell has two Swagelok connections welded onto it where it can be connected to a vacuum, which is used to pump the cell down from ambient to various pressure conditions, and to a N_2 purge for absorption free conditions. The conditions within this cell were measured by external means, using an MKS Baratron (Type 626C) and an SK Sato Datalogger which records temperature to within 0.1°Centigrade and relative humidity to within 0.1%. The laser used in this experiment is generated by a DFB laser diode (NEL NLK1E5GAAA, 20 mW power), which is tuned near 1388 nm, probing the H_2O spectral transitions at 7203.890 cm^{-1}, 7203.894 cm^{-1}, 7204.166 cm^{-1}, and 7205.246 cm^{-1}. The first two lines, 7203.890 cm^{-1} and 7203.894 cm^{-1}, have approximately the same wavelength and lower state energy and are treated as a single absorption line by summing the lower state energies.

The laser is passed through a 1x4 splitter in order to obtain enough beams for different reference needs. The first beam is passed through the LAC pitch optics and spread into the laser sheet, and is measured by the LAC. The second beam is passed through a reference etalon for the conversion of time to wavenumber using the etalon equations 2.1 and 2.2 and is measured by a DET10C detector. A third beam is passed directly to a DET10C detector as well for measurement of a reference baseline, in order for processing the images as described previously. These DET10C outputs are measured with a high speed 14 bit GaGeScope digitizer.

2.4 Demonstration Measurements

Demonstration measurements are completed in a tabletop configuration employing a low pressure cell. The low pressure cell is initially filled with room air at ambient conditions, and was then pumped down in stages to near vacuum. Data was collected at each stage resulting in spectral images like those seen in Fig. 2.14.

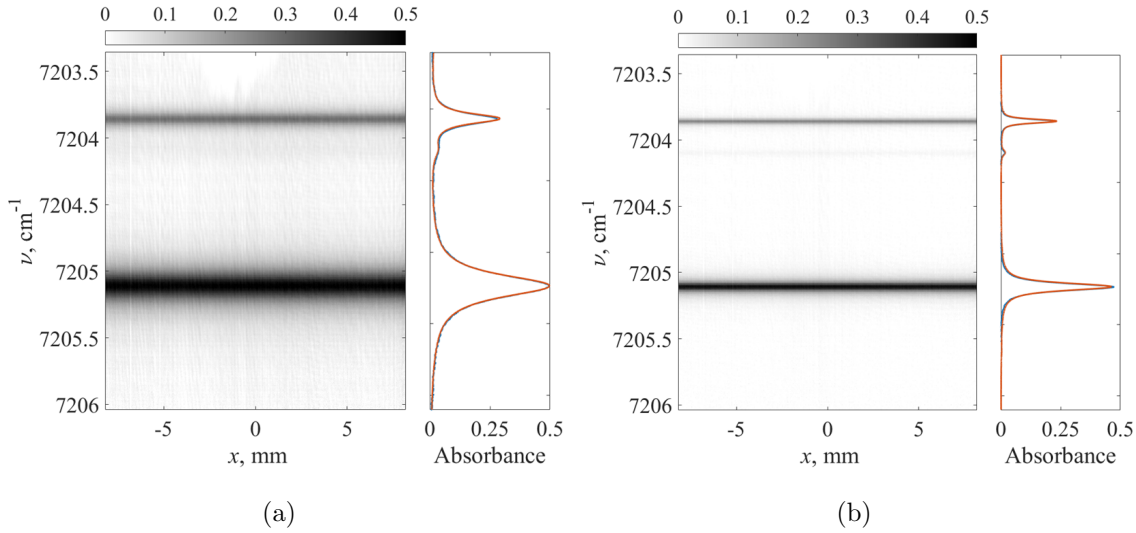

Figure 2.14: Example measurements taken in the low pressure cell with (a) taken at ambient pressure conditions (roughly 99 kPa), and (b) taken at 30 kPa. The effect of the lower pressure is seen in the spectral images as the absorbance regions become narrower and more peaked.

The changes in the spectral features are seen in the spectral images as the absorbance lines become narrower and more peaked. A span of cases were taken and reconstructed properties using the traditional spectral fitting technique were obtained. These properties matched with the externally measured data to within 5 K and 1 kPa in the 30 kPa case and to within 4 K and 1 kPa for 99 kPa case.

2.4.1 Statistics on Corrections

The original, uncorrected images taken by the LAC were capable of producing measurement results. These results were close in value to the actual test case measurements taken by the external instrumentation. However, the accuracy was limited by etaloning and structural vibration effects, and sometimes these effects caused severe errors in the reconstructed fluid properties. This is the reason it is necessary to make the corrections suggested in this work. This section will briefly focus on the statistics of the solutions obtained by the uncorrected and corrected images.

First, the uniformity of the image must be determined. The LAC is useful, in part, because of its ability to measure distinct regions of the flowfield simultaneously. In order to validate this, the measured properties obtained by each individual pixel must not have variation when measuring a uniform flowfield. This allows for more confidence in flowfields where the properties are not uniform, that the measured values are real and not just errors due to the LAC system.

Examples of the scans taken before and after the corrections were applied can be seen in Fig. 2.15. These images are obtained through the following method. The original experimental setup using the plano-concave and plano-convex cylindrical lenses was mounted on the vacuum chamber and the chamber was pumped down from ambient to near vacuum. Data was collected at approximately every 10 kPa. The lowest vacuum state is used as a baseline case, because there are minimal absorbing species left within the vacuum chamber. This process was repeated for the anamorphic prism configuration. A dark image where the laser is off is taken as well for background correction. Once this data has been collected, the dark images are subtracted from each measurement to give LAC images which are background corrected. To perform noise analysis on the images to determine if etalon rings are present, the baseline image is subtracted from the scan at a given pressure. This results in an image that is baseline corrected leaving only the noise and the absorbance present. Because the etalon curves shift across the scan, they can be averaged out. An average was taken across an image and subtracted from the entire image to remove the offsets and absorbance. What is left are images that consist of only the noise present during the measurement, including etalon effects. The images are normalized by the maximum pixel value to bring them to a similar state. The obvious etalon effects are seen in the image shown in Fig. 2.15(a), while they are not present in Fig. 2.15(b).

The etalon effects manifest in different manners depending upon where the etalon is arising from. In Fig. 2.15(a), there are two distinct shapes that are seen. The first

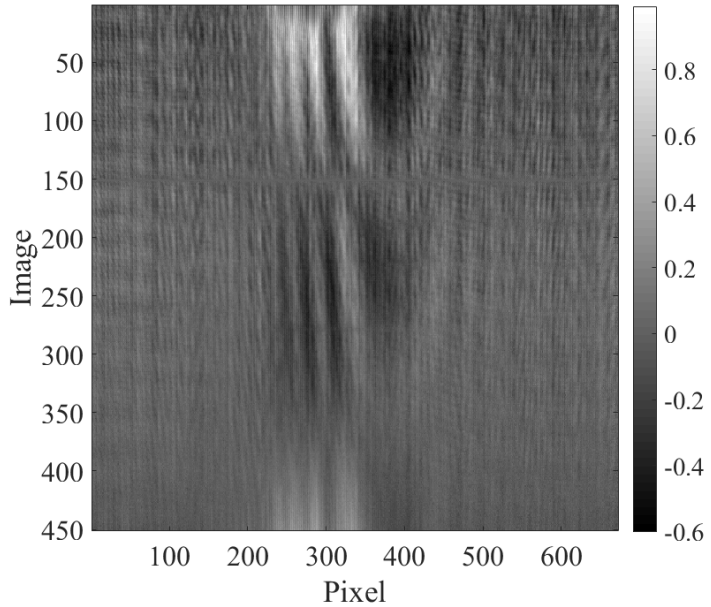

(a)

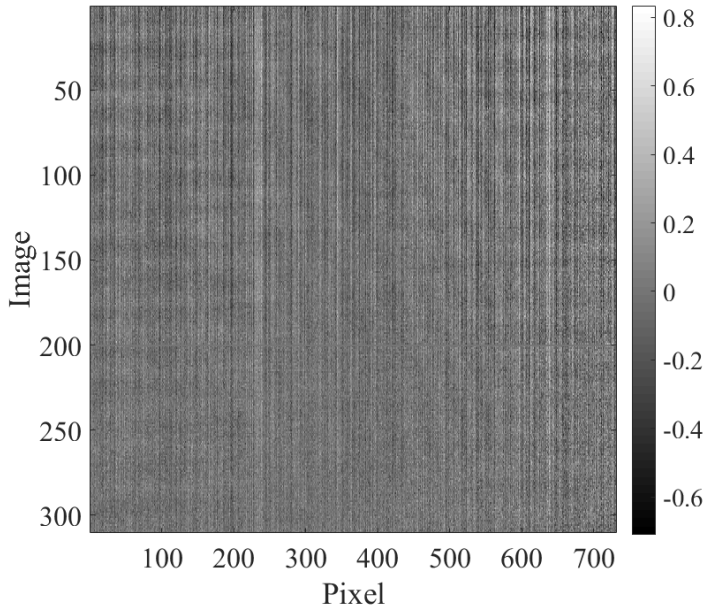

(b)

Figure 2.15: Images taken before and after the corrections were made to the LAC system. The etalon effect is seen in image 2.15(a), while there are no extra noises present in image 2.15(b).

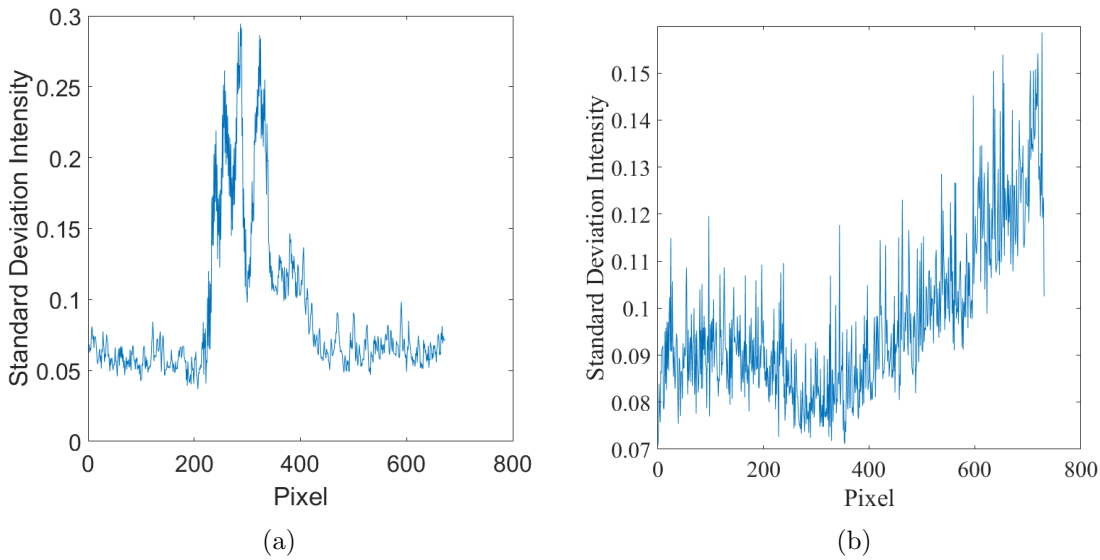

Figure 2.16: Standard deviation taken across the pixels in space. The effect of the etalon noise is seen in the higher standard deviation values for the original optical configuration for the LAC.

of these is the curved noise apparent in the system. The curve appears to originate in the pixels around the 610th pixel. This effect is present throughout the image as the curves persist across all pixels. The second form is a more regular slanted set of etalon noise, seen strongly in the right hand portion of the image, but is also weakly present in the left hand side as well. The effect of the etalons can be treated as systematic noise within the images. This is measured by completing a standard deviation both across the image, as pixels vary in space, and along each image as the measurements vary in time. The standard deviation in space in the old optical system using the cylindrical plano-convex and plano-concave lenses versus in the new optical system with the anamorphic prism pairs are seen in Fig. 2.16.

From these images it is seen that the standard deviation in space across the laser sheet is broader for the older optical system, a direct result of the additional etalon interference in the imaging. In order to obtain a more uniform laser sheet, this etalon must be removed. Similarly, the etalon affects the laser scans at each pixel in time.

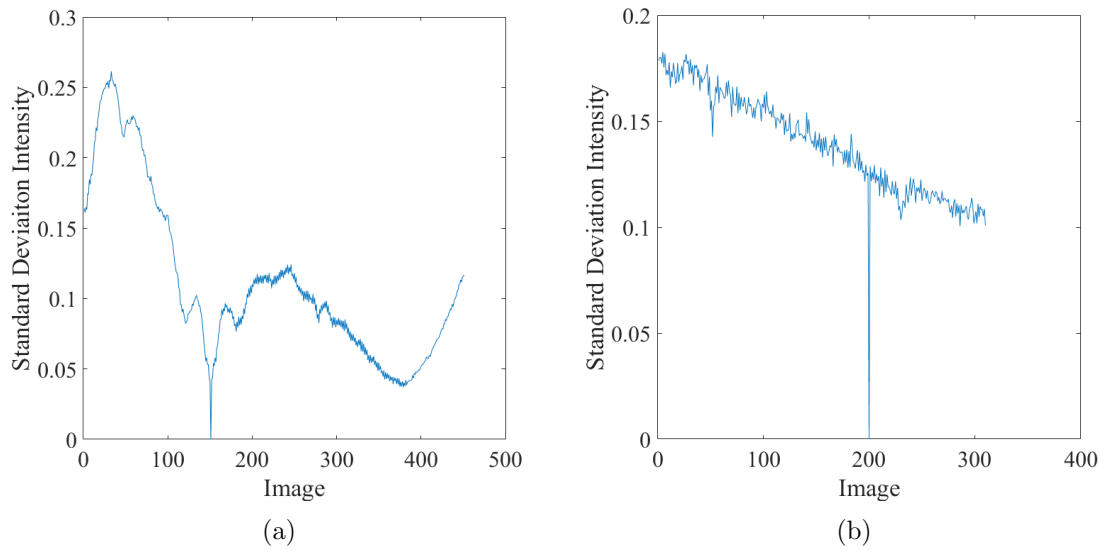

Figure 2.17: Standard deviation taken across the array in time. The effect of the etalon noise is seen in the higher standard deviation values for the original optical configuration for the LAC, as well as the variation in the deviation. The standard deviations vary in time due to the etalon signals which can vary in both time and space as seen in Fig. 2.15

This has a more direct effect on the reconstructed properties in that it directly affects the spectral shape of the scan. The standard deviation of the noise in the signals at each pixel is given in Fig. 2.17. Here it should be noted that the old configuration has an inherently higher standard deviation due to the presence of etalon noise in the signal. However, it is also notable that the variation within the standard deviation is much higher for the old optical system configuration than for the anamorphic prism pairs. These two plots demonstrate the effect of etalon on the apparent noise in the system. Because the etalon noise can vary spatially, it can be reduced by averaging, but, in averaging the pixels, information is lost spatially resulting in less resolved measurements than what could be obtained if the signal had no contribution of the etalon noise. This is the reason for the creation of the new system, which removes the effects of this etalon noise in the LAC pitch system.

The plots shown in Figs. 2.18, 2.19, and 2.20 are demonstrations of the deleteri-

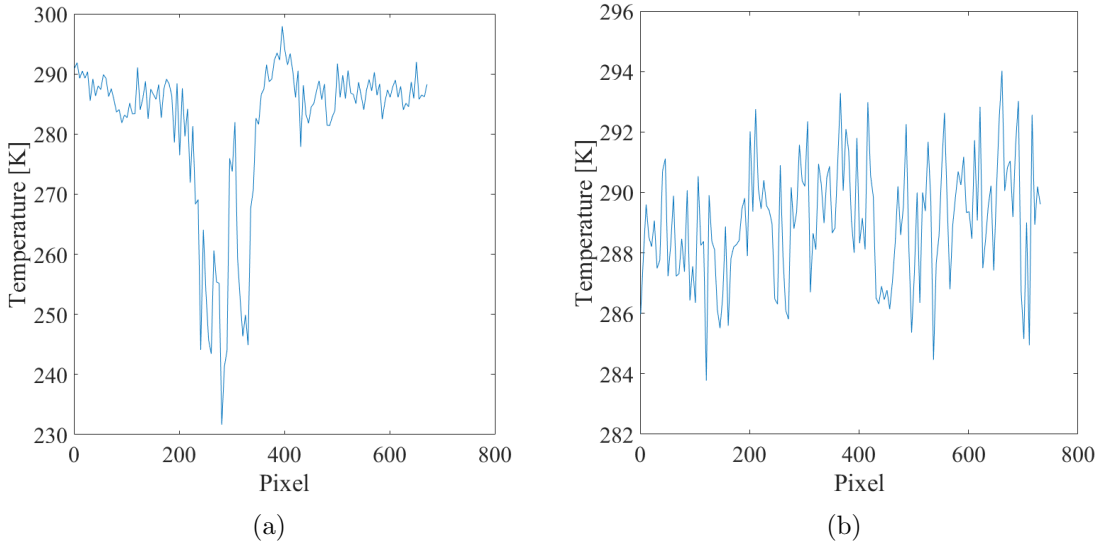

Figure 2.18: Temperature reconstructed from (a) the original optical setup and (b) the new optical setup. It is readily apparent that the etalon negatively impacts the solutions. The standard deviations are (a) 13 K and (b) 2 degrees K.

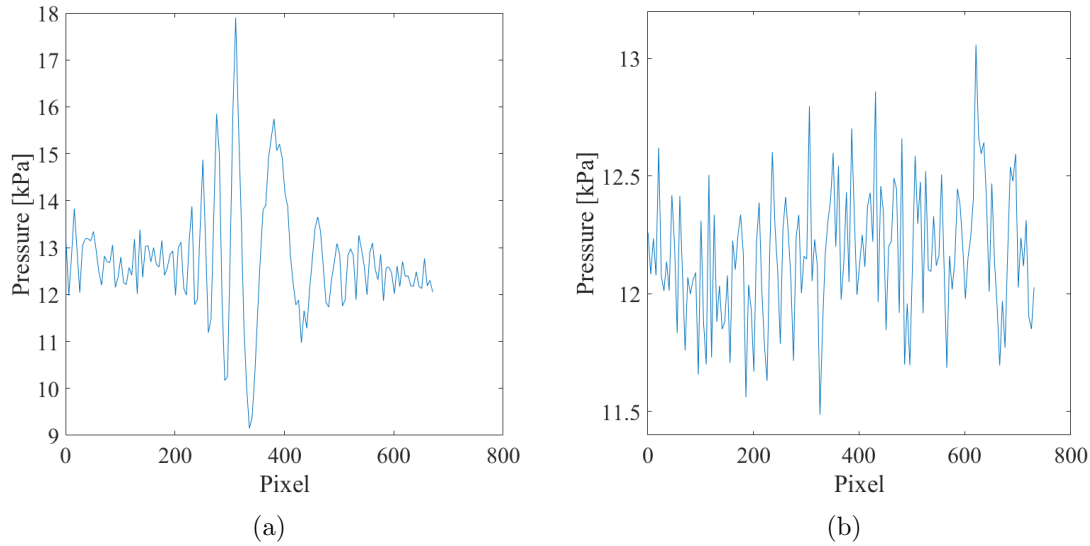

Figure 2.19: Pressure reconstructed from (a) the original optical setup and (b) the new optical setup. It is readily apparent that the etalon negatively impacts the solutions. The standard deviations are (a) 1.22 kPa and (b) 0.28 kPa.

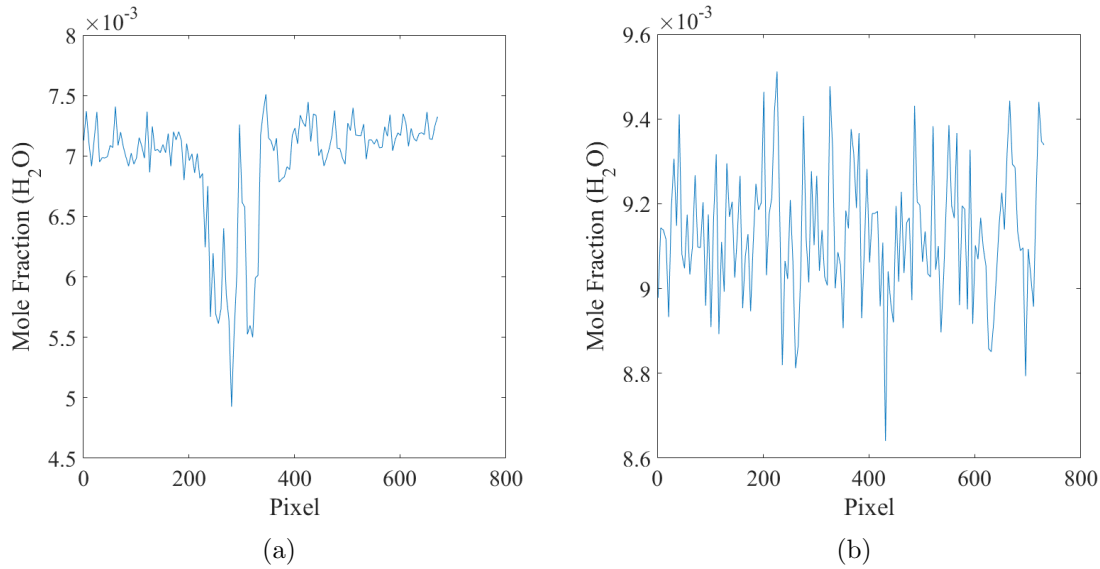

Figure 2.20: Mole Fraction reconstructed from (a) the original optical setup and (b) the new optical setup. It is readily apparent that the etalon negatively impacts the solutions. The standard deviations are (a) 4.86 e-04 and (b) 1.57 e-04.

ous effects that the etalon signals have on the reconstruction of properties, and the improvements gained by implementing the anamorphic prism pair optical arrangement. As seen in Fig.2.15, there is a large contribution to the error of the image due to etalon effects near the center of the frame. This contribution leads to very large errors in the reconstructed temperatures, pressures, and mole fractions across the pixels in this region. In order to measure the properties, the traditional spectral fitting scheme is applied to these measurements. The measurements were made in low pressure conditions in air with no contribution from flame exhaust species, and so this reconstruction technique is both valid and accurate because the collisional partners are well known and the broadening parameters are documented. In order to perform this analysis, the LAC images were taken, along with a dark image. The dark image was subtracted from the LAC scan to obtain a background corrected LAC image. Because the pressure was low, an accurate baseline fitting was applied to the wings of the scan. With the scans from each pixel and an accurate baseline, Beer's

Optical Setup	σTemp (K)	σPress (kPa)	$\sigma\chi$
Lenses	13	1.22	4.86 e-04
Prisms	2	0.28	1.57 e-04

Table 2.2: Table demonstrating the variation in the linestrength with temperature over several transition lines. It can be seen that these lines may or may not be effective choices due to the variation in linestrength depending on the temperature range expected in the measurement.

Law was applied to obtain a spectral image. The data given was downsampled to every fifth pixel to reduce processing time. No averaging was done on the image or the pixels in order that the true noise values for a single image are preserved. The reconstructed properties seen using the old optical arrangement from the system with the plano-concave and plano-convex lenses has a large contribution to noise from the etalon signal seen in the middle of the image. This manifests as very large errors in the reconstructed properties seen in Figs. 2.18(a), 2.19(a), and 2.20(a). The anamorphic prism optical arrangement was passed through the cell at approximately the same pressure and the properties measured are given in Figs. 2.18(b), 2.19(b), and 2.20(b). As is seen here, the properties reconstructed are much more uniform, without the large errors arising due to etalon effects. The standard deviations were taken across the pixels for the reconstructed temperatures, pressures, and species fraction in order to approximate how much more precise the anamorphic prism pair measurements are than the lenses. These are listed in Table 2.2, where vast improvements are made in the reconstruction of each property. This set of experiments demonstrates the necessity of and improvements gained from applying the anamorphic prism pairs to negate etalon noise from the system.

2.5 Structural Vibrational Analysis

An analysis was completed to determine the effect that structural vibrations have on the uniformity of the laser sheet. Ideally, vibrational effects should be completely

removed from the laser sheet. As stated, this can be accomplished through a combination of post processing corrections and through the broadening of the laser sheet. The test cases completed expanded the sheet from a Gaussian with a standard deviation of 1.6 mm to a Gaussian with a standard deviation of 7.0 mm in nine steps. The in plane motion is corrected as described, with rising edge detection being used to realign the images taken by the LAC and to account for the in plane motion. Fig. 2.21 demonstrates the difference in the standard deviation along the individual pixels in space when the in plane vibrational mode is active and after it has been corrected. The correction brings the influence of the errors introduced by this vibrational mode down to the level of the shot and dark noise inherent in the system. This is seen in the figure, where, after the image has been realigned, the standard deviation is much smaller. Additionally, the variation in the standard deviation form line to line is also reduced. The system demonstrated in this measurement has a laser sheet with a Gaussian thickness that is 7.0 mm standard deviation. It will be shown that a beam with this thickness has fluctuations in intensity below that of the inherent noise, making this measurement a valid method for looking at the standard deviation due only to the in plane motion.

The out of plane motion was also studied in this set of measurements, and was completed by taking measurements with a series of beam thicknesses as described previously and correcting the images for the in plane motion using the post processing techniques described. This leaves a series of images in which only the out of plane intensity variations remain. This has been previously described in Fig. 2.10(b), where the variation in intensity is seen. The standard deviations of the pixels in the nine cases described are seen in Fig. 2.22.

Here it is seen that as the thickness of the laser sheet increases, the standard deviation of the intensity due to errors in the out of plane motion decreases. The mean of the standard deviation at each of the thicknesses given is taken and compared

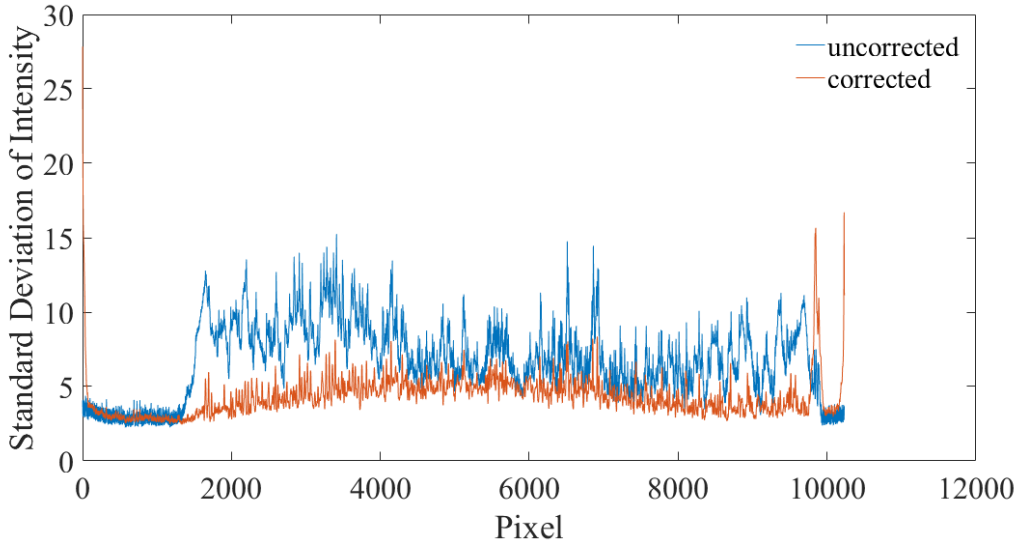

Figure 2.21: Comparison of the standard deviation across all pixels for the uncorrected in plane vibrational mode versus after the correction.

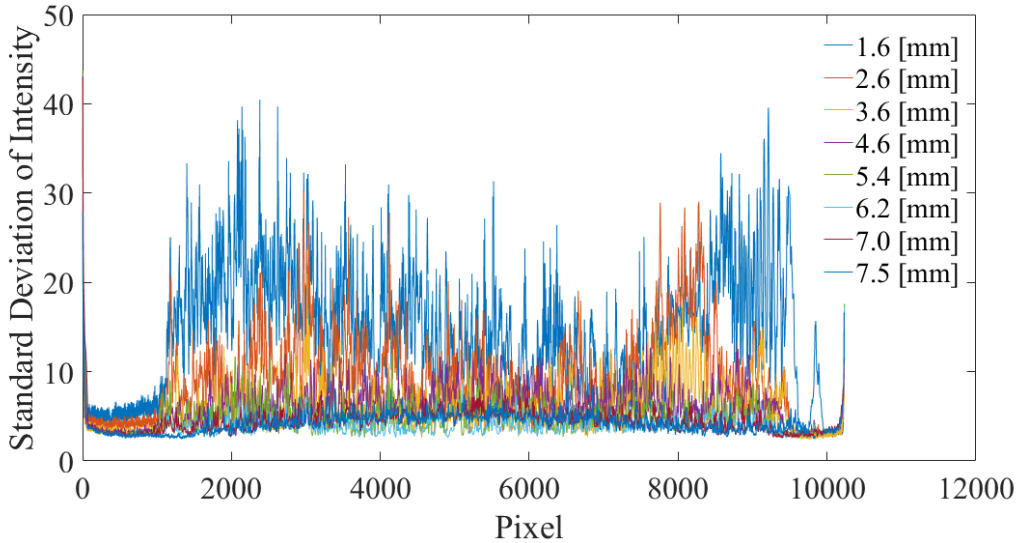

Figure 2.22: Comparison of the standard deviation across all pixels for the cases described. As the thickness of the laser sheet increases, the standard deviation in intensity decreases.

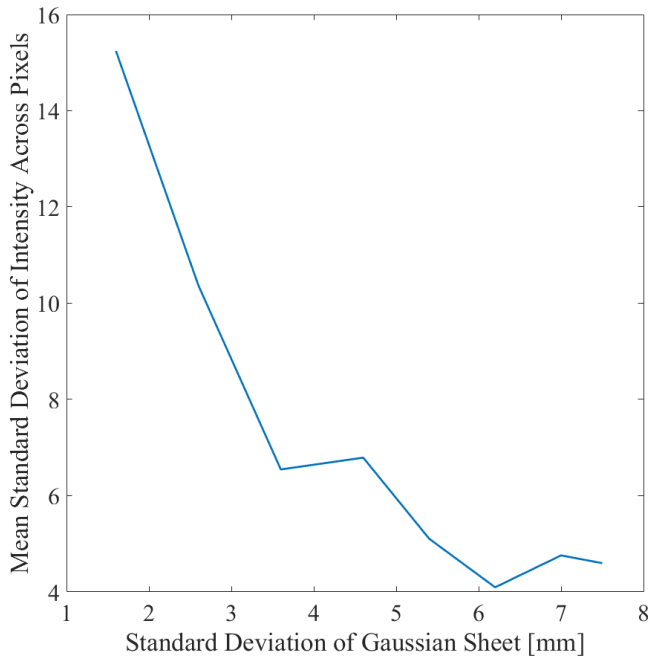

Figure 2.23: The mean standard deviation of the pixels in time compared to the thickness of the laser sheet for each measurement taken. As can be seen, the curve asymptotes to a specific values of about five counts, the inherent noise within the system. The specific values are tabulated in Table 2.3.

to the standard deviation of the Gaussian shaped laser sheet. These are plotted in Fig. 2.23, where the mean of the standard deviations across the pixels is taken and compared to the thickness of the laser sheet.

Fig. 2.23 demonstrates the reduction in the standard deviation of the intensity of a uniform image whenever the beam thickness is increased. By thickening the beam, the variation in intensity as the Gaussian beam shape wanders varies less over the LAC. At some thickness, the variation in intensity is below the inherent noise in the system. This occurs, for these measurements, near a Gaussian with a standard deviation of about 5 mm. Once this limit has been reached, further widening of the beam only results in the further loss of signal. The values for the standard deviations are tabulated in Table. 2.3, demonstrating both the necessity and feasibility of the vibrational corrections made to the LAC system.

Beam STD [mm]	STD Intensity uncorrected	STD Intensity corrected
1.6	22.0	15.2
2.6	19.1	10.4
3.6	13.7	6.5
4.6	13.7	6.8
5.4	11.6	5.1
6.2	9.1	4.1
7.0	8.8	4.8
7.5	7.4	4.6

Table 2.3: Table demonstrating the standard deviation of the uncorrected and corrected images for each of the given beam standard deviations.

2.6 LAC Conclusions

The LAC system has been described and tested in a low pressure and ambient environment. Several novel challenges with the system were noted and overcome including beamshaping, etaloning, and structural vibrations. Beamsteering continues to present a challenge that needs to be overcome to make this a robust testing method. The effects on the nonunifomrity of the laser sheet were described for both the etalon case and the vibrational cases. Once corrections are made for both cases, the uniformity and accuracy of the method are shown to be in high agreement with externally measured flow properties. This demonstrates the feasibility of the LAC in laminar environments. In order to be a more fully robust measurement technique, the beamsteering effects must be overcome in order to extend the method to turbulent environments with high density gradients.

CHAPTER III

Baseline Error Rejection through Second Derivative Curve Fitting

A novel application of second derivative fitting to SDWAS to process typical scanned absorption signals in the presence of large baseline errors to obtain accurate spectral shapes in measurements with relatively low sampling rates for aerospace applications will be further described in this chapter. Traditional spectral fitting measurements rely on accurate calibration of baseline measurements. The errors in the calibrated measurements skew the results of the inferred flow properties. In real experimental conditions, it is challenging to guarantee the accuracy of the baseline measurements. The second derivative fitting method will mitigate the effect of these baseline errors, greatly increasing the accuracy of the measured parameters, specifically of the pressure. This technique is intended to mitigate the systematic errors resulting from these calibration measurements. The fitting technique not only reduces the effect of the poorly measured baseline, but also increases the sensitivity of the method to small variations in the spectrum. The combination of the baseline mitigation and the increased sensitivity allows for very accurate inference of pressure from spectral fitting techniques, which is typically a challenging task. A final benefit of this method is that, because it is applied in wavenumber space, the sampling rate dose not need to be as high as the WMS fitting techniques, which are applied in

Fourier space. This allows for the method to retain some of the benefits of the WM fitting techniques, but on systems with much lower sampling rates, such as the Linear Array Camera.

3.1 Baseline Measurement Experiments

One of the leading reasons for the use of the second derivative method is its insensitivity to baseline errors. Many TDLAS experiments rely on accurately measured or fit baselines for the TDLAS scans, but often errors in the baselines can cause uncertainty and errors within a measurement[27, 76, 34]. Early in the demonstration work for the LAC, it became evident that the measured baseline and the measurements through the optical access ports in the low pressure cell were not matching correctly. This was leaving a section of the absorption profile with errors, resulting in measurements that were low in accuracy when attempting to use the measured baselines. This was overcome at the time by the application of baseline fitting schemes to the wings of the data, which works well in low pressure, low temperature cases, due to the large regions of zero absorption in the wings of the spectral features. However, baseline fitting is not always possible in TDLAS measurements depending on the experimental setup and the temperatures and pressures being measured. This lead to a set of experiments to determine the cause of the baseline errors.

Several basis measurements were made by sending a beam both through the low pressure cell configuration described in Chapter II with the windows in place and directly to a detector face. A DFB laser (NEL NLK1E5EAAA) was used to generate the wavelength near 1392 nm in the same manner as described in the LAC low pressure cell experiments. This test, however, replaced the LAC sheet forming optics and the LAC itself with a single beam collimator pitch and catch set of collimators which were measured by a DET10C detector. These cases are seen in Fig. 3.1, where the intensities of several wavelength scans centered on the given wavenumbers are plotted

normalized by a reference scan. The curvatures seen in these plots demonstrates the variation of the transmission through the optical cell with wavenumber. If the transmission was constant, then each of these lines would be a simple, constant ratio. However, it is evident that there is some effect of the wavelength and scan intensity which can cause the ratio of the beams to be inconsistent. This can occur due to the variation in the index of refraction of a window with wavelength and the variation in the detector sensitivity to wavelength. These effects, when coupled, can case variations in the measured intensities of the direct beam and the beam passed through the windows. This means that even the small variations in the wavelength of the output light from a TDL are enough to disrupt the baseline measurements, because the dependencies of the ratio between the reference beam and the transmitted beam vary within the scan. The experiment can be calibrated to account for the abnormalities induced by the windows and the intensities, but in experimental setups, it is not always possible to perform these types of calibration measurements. This leads to the necessity of a measurement technique in which these baseline errors can be rejected.

3.2 Comparison of Second Derivative Spectroscopy with WMS

WMS spectroscopy is a technique that can approximate different derivative orders through the use of time frequency harmonics of a signal and careful consideration of modulating amplitudes[46, 48]. The second harmonic is a close approximation to the second derivative and has even been used to obtain the second derivative prior to the application of true WMS spectroscopy[47, 48]. Whereas the second derivative method is used mainly for broadband under resolved measurements, WMS is typically used to measure highly resolved transitional lines. This method has

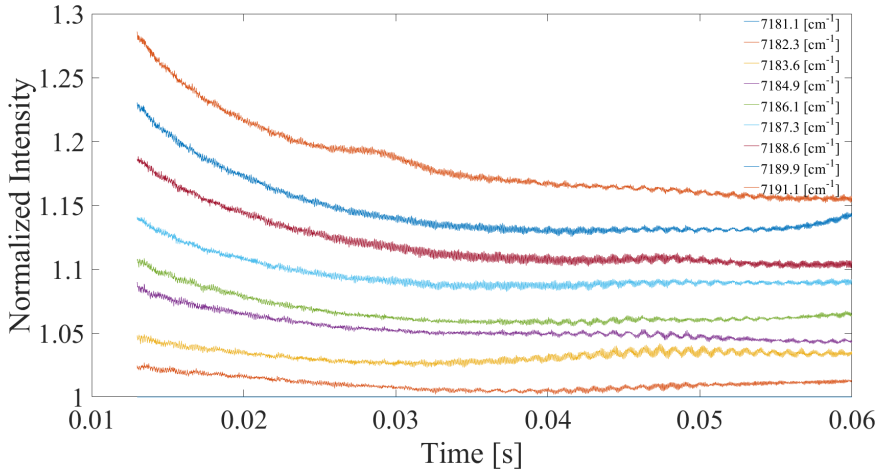

Figure 3.1: Demonstration of variation due to windows in the optical setup. Several scans were taken through the optical windows of the purge tube and referenced to a single line. The curvatures of these lines arise from the intensity variation with wavenumber of a scan when referenced to the intensity variation with the wavenumber of the reference scan. If no variation existed, these lines would be flat single value ratios, rather than curves.

been used extensively in high temperature combustion environments. As mentioned previously, this technique is referred to as the WMS $2f/1f$ method and is used to generate noise free measurements that have very high accuracy [77, 78, 79]. The theory upon which the WMS technique operates is that a high-frequency modulation of the light wavelength induces harmonics in the signal. These harmonics occur at precisely the integer multiples of the modulating frequency. These harmonics are measured with a lock in amplifier set to capture that integer multiple of the scanning wave frequency. The mathematical effect of this method is to look at the signal in Fourier space rather than wavenumber space, which makes the acquisition of these signals straightforward. However, this method requires tunable diode lasers that are capable of very fast tuning rates and detectors that can collect the data at sufficient rates to adequately sample the harmonic frequencies.

The second derivative spectroscopy method for highly resolved lines is analogous to the WMS $2f$ technique, in that it uses the second derivative to obtain accurate mea-

sures of flow properties. However, rather than complete this analysis in the Fourier space, the second derivative spectroscopy technique applies the second derivative fitting to the measured spectrum in post processing. In typical measurements where this technique is applied, the probed wavenumber range is very broad. This work will apply this fitting technique to the same highly resolved spectra as the WMS technique. This is done to recover the baseline rejection captured from the second derivative without the necessity to use the costly and large components necessary to apply the WMS technique.

3.3 Effects of Baseline Errors

Baseline errors affect the accuracy of traditional spectral fitting by causing a systematic inclusion of false information encoded within the spectral features. There are several such effects that can result from baseline errors. Effective broadening of the spectral feature through a low grade additional curve, increasing the apparent height of the wings of an absorption profile or causing a very lopsided profile if the baseline varies linearly with the wavenumber. These erroneous baselines can cause wildly varying solutions and even cause typical spectral fitting to fail entirely. Some examples of what these baseline errors can look like are seen in Fig. 3.2.

Several variations of baseline correction exist. If the laser is well characterized, and the experimental setup is well characterized, a simulated baseline can be obtained for a signal. This is beneficial, because the simulated signal is noiseless and should be an appropriate fit for the scans. The largest downside to this method is that there are many variables that can affect the shape of the laser scan, including differences in the index of refraction of windows, differences between experimental setups, and differences due to alignment variations. A second method is to take a direct baseline measurement, which can be fitted to a measured signal using the wings of the scan. This is beneficial because it accounts for minor variations in laser power over the

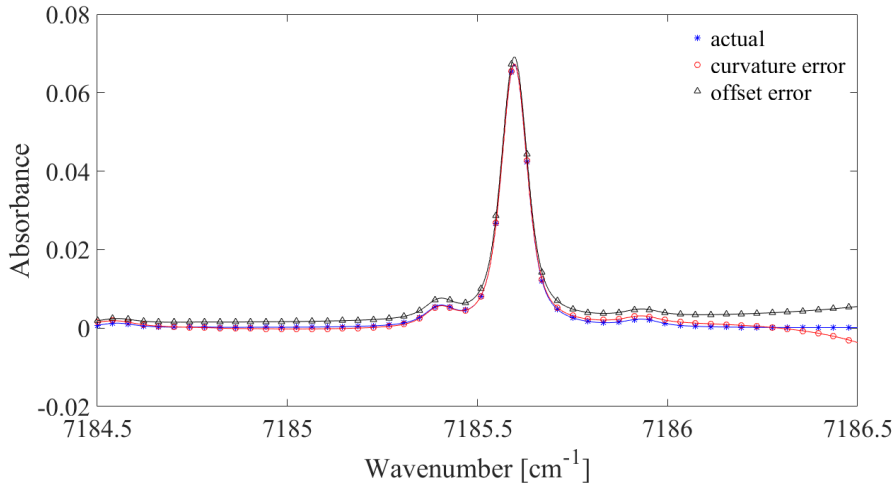

Figure 3.2: Demonstration of three absorbance curves, the first representing the actual measurement, the second representing a poor fit to the wings of a scan inducing an error in the curvature of the baseline, and the third representing an error induced by offsetting the baseline. These present as errors in the reconstructed properties in the solutions, when a solution can be obtained at all.

course of a run and is a directly fitted baseline. However, the same downsides exist in that the addition of optics and windows can affect the calibration of this method and moving between experiments also ruins the calibration. A third method is that the zero absorption regions in between spectral features can provide locations to which a baseline can be fit. The benefits of this method are that the baseline is unaffected by the addition of new optics and windows, and is unaffected by moving the setup from one experiment to another. The biggest downfall of this method is the need for large areas of zero absorption in between absorption features to which to fit the baseline. Without a set of zero absorption regions, this method fails. This makes it inconvenient to use this method in many aerospace applications, where high pressures and temperatures broaden absorption features, and cause additional high temperature absorption lines to begin to appear. A better method for baseline correction or baseline error rejection is needed.

3.4 Analysis of Highly Resolved 2nd Derivative Spectroscopy

The second derivative method of spectral fitting applies the second derivative directly to the spectra, rather than using harmonics of a modulation current to obtain a surrogate second derivative spectrum as in WMS $2f$. The general equation for any derivative of the absorption can be modeled from Beer's Law:

$$-\frac{\mathrm{d}^n}{\mathrm{d}\nu^n}\ln\left(\frac{I}{I_o}\right) = \frac{\mathrm{d}^n}{\mathrm{d}\nu^n}\alpha = \frac{\mathrm{d}^n}{\mathrm{d}\nu^n}\left(\sum_{i\in\Omega} P\chi S_i\left(T\right)\phi_i(P,T,\nu)L\right) \tag{3.1}$$

where n is the derivative order. This reduces to the equation:

$$\frac{\mathrm{d}^n}{\mathrm{d}\nu^n}\alpha = P\chi L\sum_{i\in\Omega} S_i\left(T\right)\phi_i^{(n)}(P,T,\nu) \tag{3.2}$$

where ϕ_i^n is the nth-order derivative of ϕ with respect to ν and the only term in the right hand side of the equation on which the derivative acts is the lineshape function. This means that errors in the lineshape function parameters, such as those introduced by the missing HITRAN broadening parameters, still have an effect on the properties inferred by spectral fitting of the measured spectra. This is also seen in WMS spectroscopy, where the accuracy of the measurement depends on the accuracy of the spectral database.

The general error for an arbitrary derivative of spectral fitting method between the true measured transitions and the inferred transitions in the presence of baseline error is defined as:

$$\epsilon_{(n)} = \int_{-\infty}^{\infty}\left[\frac{\mathrm{d}^n}{\mathrm{d}\nu^n}\left(\hat{\alpha}-\alpha+\Psi\right)\right]^2\mathrm{d}\nu \tag{3.3}$$

where $\epsilon_{(n)}$ is the integrated error between the true spectrum, $\hat{\alpha}$, and the modeled spectrum, α, where Ψ is a measure of the baseline error. It is important to note that as this error is minimized to obtain a solution, the baseline error term will skew the inferred properties from the true properties. Eq. 3.3 expands to the following general

equation:

$$\epsilon_{(n)} = B^2\left(\underline{\hat{x}}\right) M_n\left(\underline{\hat{x}}\right) + B^2\left(\underline{x}\right) M_n\left(\underline{x}\right) - 2B\left(\underline{\hat{x}}\right) B\left(\underline{x}\right) Z_n\left(\underline{\hat{x}}, \underline{x}\right) +$$

$$\Omega_n + B\left(\underline{\hat{x}}\right) \Gamma_n\left(\underline{\hat{x}}\right) - B\left(\underline{x}\right) \Gamma_n\left(\underline{x}\right) \tag{3.4}$$

where the terms are broken down as:

$$B\left(\underline{x}\right) = P\chi S\left(T\right)$$

$$M_n\left(\underline{x}\right) = \int_{-\infty}^{\infty} \Phi^{(n)}\left(P, T, \nu\right)^2 \mathrm{d}\nu$$

$$\Omega_n\left(\underline{x}\right) = \int_{-\infty}^{\infty} \Psi^{(n)}\left(\nu\right)^2 \mathrm{d}\nu$$

$$\Gamma\left(\underline{x}\right) = \int_{-\infty}^{\infty} \Phi^{(n)}\left(P, T, \nu\right) \Psi^{(n)}\left(\nu\right) \mathrm{d}\nu$$

$$Z\left(\underline{\hat{x}}, \underline{x}\right) = \int_{-\infty}^{\infty} \Phi^{(n)}\left(\hat{P}, \hat{T}, \nu\right) \Phi^{(n)}\left(P, T, \nu\right) \mathrm{d}\nu$$

Here $\underline{x}$ denotes a vector of the measured flow properties and $\underline{\hat{x}}$ denotes the true properties of the flow. If the influence of the baseline error is large, this generates a discrepancy between the true flow properties and the inferred flow properties when the equation is minimized. In this equation, there are several solution terms, the terms where the errors in the measurement have no effect. These are the $B^2\left(\underline{x}\right) M_n\left(\underline{x}\right)$ terms and the $2B\left(\underline{\hat{x}}\right) B\left(\underline{x}\right) Z\left(\underline{\hat{x}}, \underline{x}\right)$ terms and can be seen to have no direct effect introduced from the baseline error. The error terms are called Ω_n and $B\left(\underline{x}\right) \Gamma\left(\underline{x}\right)$ terms and are directly affected by the introduced errors from the baseline. The benefit of the equation in this form is that the error and solution terms can be directly compared to determine the sensitivity of each of the different derivatives to error. This equation gives bounds to how much error is acceptable and in what flow regimes the solutions will work. In practice, if estimates of the flow properties are known, this equation can

be used to generate expected solutions values, assuming a baseline error. This can be used to determine acceptable tolerances for baseline errors in given flow regimes and allow for researchers to understand the influence of the baseline errors on the solutions.

The first note to be made about the Eq. 3.4 is the dependence on the $B(\underline{x})$ term, which is for all practical purposes, always less than one. It is seen that the solution terms depend on $B^2(\underline{x})$, while the error terms only depend on $B(\underline{x})$. This is due to the influence of the linestrength. For weaker transitions, the sensitivity of the solution terms decreases, while the sensitivity to the error terms increases. This leads to the need to pick strong absorption lines. However, once a transition is chosen, the $B(\underline{x})$ term does not change with derivative order. Taking the ratio of the solutions terms at different derivative orders demonstrates how the sensitivity of the error to these terms varies with the derivative. These are seen in Fig. 3.3, where, for the spectral feature at 7242.37 cm^{-1}, the ratios are plotted as 3.3(a) $M^{(2)}/M^{(0)}$, 3.3(b) $\Omega^{(2)}/\Omega^{(0)}$, 3.3(c) $\Gamma^{(2)}/\Gamma^{(0)}$, and 3.3(d) $Z^{(2)}/Z^{(0)}$ for computationally constructed integrals of the temrs. The analytical expressions for these integrals have not been computed. The second derivative terms are calculated over pressures and temperatures ranging from 0.1 atm to 2.2 atm and 300 K to 2100 K. This transition was chosen as a representative case, but the overall trends hold for other spectral features as well. Because the $B(\underline{x})$ terms cancel out in the ratios, what is left is merely a function of the Voigt profile and the baseline error term. The Voigt function is well behaved, and well understood. The variation in the function is based on the broadening parameters, which vary from line to line, but do not change the trends of the function from line to line. The baseline error term used in these plots is representative of the expected errors in an experiment. A typical second derivative shape of a spectral transition is seen in Fig. 3.4, where the captured spectrum is seen on the left and the second derivative of that spectrum is seen on the right. The second derivative minimizes the sensitivity to error

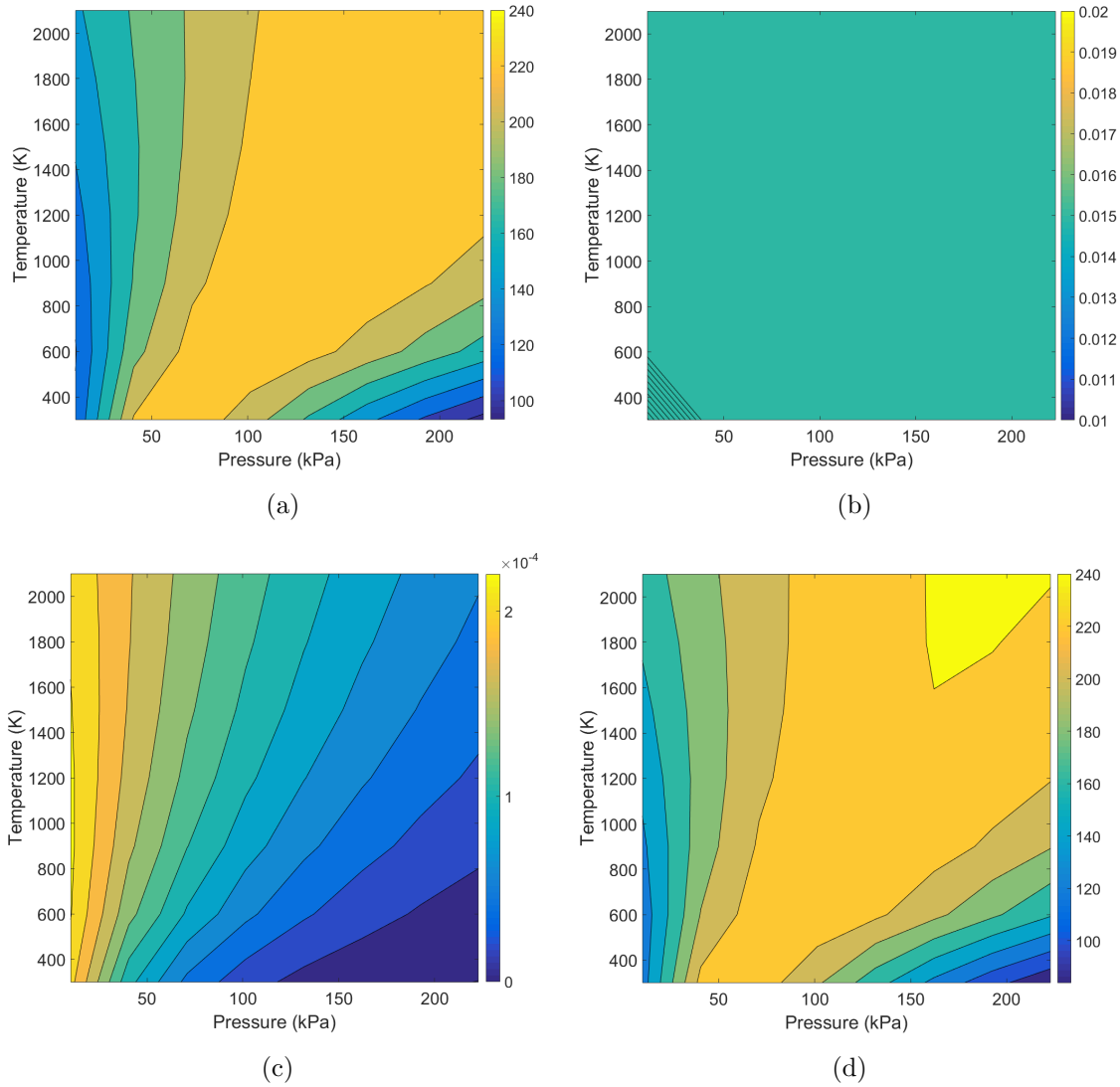

Figure 3.3: Ratios of the second derivative to the zeroth derivative of the solution and error terms in Eq. 3.4 are demonstrated over a representative sample of the flow property space expected in the experiments performed in this work. The B values cancel out of the ratios leaving the solution terms as (a) $M^{(2)}/M^{(0)}$, (b) $\Omega^{(2)}/\Omega^{(0)}$, (c) $\Gamma^{(2)}/\Gamma^{(0)}$, and (d) $Z^{(2)}/Z^{(0)}$. It should be noted that as the derivative order is increased, the solutions terms grow rapidly, while the error terms either remain constant for the Ω case or are reduced as in the Γ case.

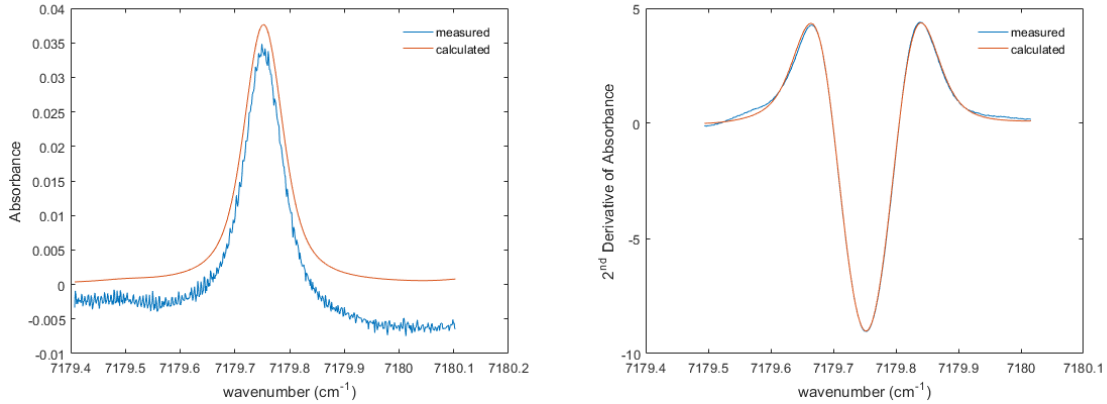

(a) (b)

Figure 3.4: Example second derivative measurement shape of a transitional line compared to the traditional spectral fitting algorithm with baseline noise.

due to the baseline, which has a very low curvature, and maximizes the sensitivity due to the spectral features which have much higher curvatures. This leads to solutions which are insensitive to errors in the baseline.

3.5 Demonstration Experiments

The second derivative method was set up and tested on both the same bench top experiment as the LAC for validation, as well as over a McKenna flat flame burner using methane/air mixtures. The validation experiments are compared to the well known conditions measured from external instrumentation. The McKenna flat flame burner experiments are compared to simulated data using Canterra as well as to previous literature.

3.5.1 Low Pressure Validation Experimental Setup

The experimental setup for the low pressure validation measurements was nearly identical to the initial LAC low pressure measurements. The pitch and catch optics were mounted to either end of the low pressure cell, which was instrumented with an

MKS Baratron (Type 626C) and an SK Sato Datalogger which records temperature to within 0.1°Centigrade and relative humidity to within 0.1%. As with the LAC testing, the cell was initially filled with ambient air at one atmosphere and approximately 294 K. The pressure cell was pumped down in steps to near vacuum and data was taken at each interval. The H_2O lines probed were near 1400 nm in the NIR region and were chosen based on criteria which will be further described in Sec. 3.6.

3.5.2 Low Pressure Cell Data

Data was collected at a number of reference pressures during the evacuation process. At each point, the typical curve was fitted along with the second derivative and compared to the measured values. In each case, the second derivative fitting was more accurate than the direct fitting, due to the low signal noise and the high baseline error rejection of the derivative fitting method. As the pressure is reduced, the fitted baseline becomes more accurate due to the increased zero level wings of the scans. The baseline is fit to the flat sections of these wings and provides a very good reference location for the measurements. However, at high pressures, as the wings of the spectral features widen, the reference for the baseline is much more narrow and does not fit as well. Example plots of this can be seen in Fig. 3.5, where the top row is the measurements at 99 kPa and the bottom row is the measurements at 30 kPa. The left hand column is the zeroth order derivative, while the right hand column is the second order derivative. It is clear that the fitting to the high pressure cases is much more closely matched by the second order derivative, where the extra width of the lines prevents a good baseline from being fit to the data set. However, in the 30 kPa case, where there are several wide regions of of zero level absorbance, a much more accurate baseline is able to be fit to the spectra, resulting in properties reconstructed from the zeroth order derivative to be just as accurate as properties reconstructed from the second order derivative.

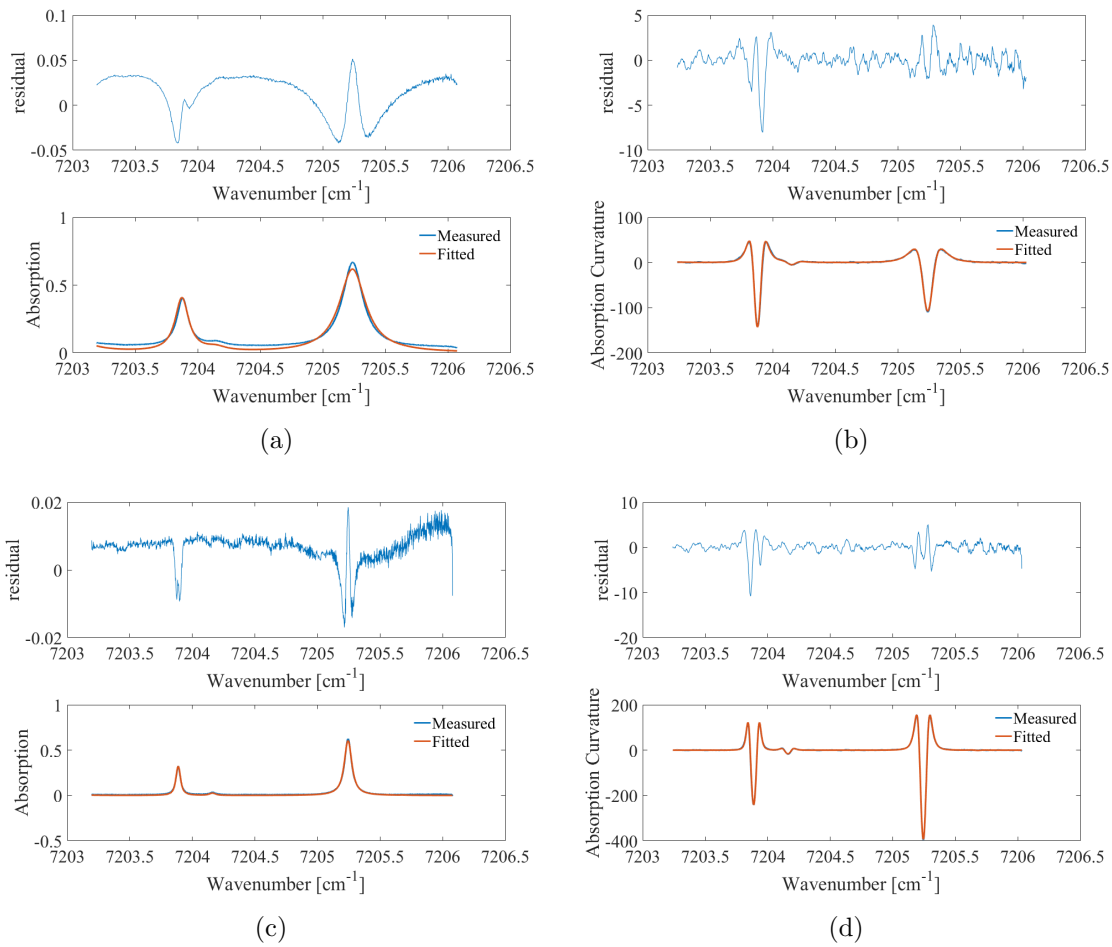

Figure 3.5: Representative measurements in the low pressure cell for zeroth and second order derivatives measured at 99 kPa and 30 kPa respectively. It is evident that the fitting is much more accurate in the second derivative case for the higher pressure where the wings of the baseline are harder to fit for the zeroth order derivative fitting. In the lower pressure case, the fitting is about even for both the zeroth order and the second order derivative fits.

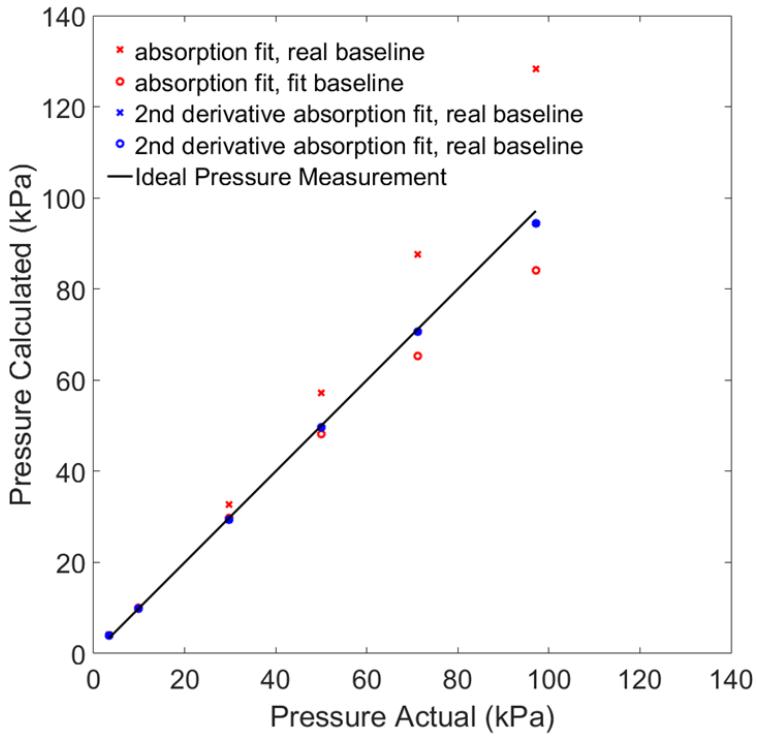

Figure 3.6: Measured values for the zeroth order derivative and the second order derivative compared to the external reference measurements. The second order derivative technique provides much more accurate solutions as the pressure continues to rise.

Because the errors in the fitted baseline are dependent on the amount of zero level absorbance present in the signal, it is expected that the zeroth order derivative technique will match the accuracy of the second order technique in low pressures, where the absorption lineshape is narrow and these fitting regions exist. As the pressure rises, however, the absorption lineshape broadens as seen in Sec. 1.6.2 and the areas where the baseline is able to be fitted grow smaller. In these regions, the baseline error dominates and the second derivative reconstruction method, which rejects this baseline error, becomes more accurate. This is seen in Fig. 3.6, where, as the pressure continues to rise, the reconstructed values from the second order derivative method remain accurate, while the zeroth order derivative reconstructed properties deviate from the externally measured reference sources by up to 30%.

3.5.3 Low Pressure Cell Conclusions

The low pressure cell demonstration shows the reduction in uncertainty due to the second derivative fitting's baseline rejection characteristics. The technique performs better than the zeroth order derivative especially in high pressure cases where the errors due to baseline misfitting grow rapidly. As shown in Fig. 3.6, the second derivative reconstruction technique captures important information in the measurements just as WMS, while simultaneously rejecting misinformation added by incorrect baseline measurements.

3.5.4 McKenna Flat Flame Burner Experimental Setup

The experimental setup for the McKenna flat flame burner measurements used the same pitch and catch optics as the low pressure cell. The TDL was passed through a 1x4 beam splitter, where one line was passed directly to a detector, a second line was passed through an etalon reference cell in order to convert time into wavenumber, and a third line was passed through the McKenna flat flame burner. The fourth line remained unused. The McKenna flat flame burner is a premixed burner, which genreates flat flames over a porous, sintered burner plug. The burner has a secondary shroud ring, which, in this work, was used to create an N2 sheath around the flame. Additionally, a water cooling line runs through the sintered burner plug that allows for cooling of the burner. The McKenna burner was set up as seen in Fig. 3.7, where the laser pitch and catch optics were inserted into a nitrogen sheath in order to purge ambient absorption from the signal and simultaneously keep the optics cooled from the heat of the flame. The test conditions here used a methane/air mixture of gases, because methane is well studied. Most of the data gathered was for an equivalence ratio, Φ of 0.87 because we have studied this condition in past work and we have additional measurements available. The H_2O spectral lines tested were in the same region as the low pressure cell cases, although different transitions were chosen that

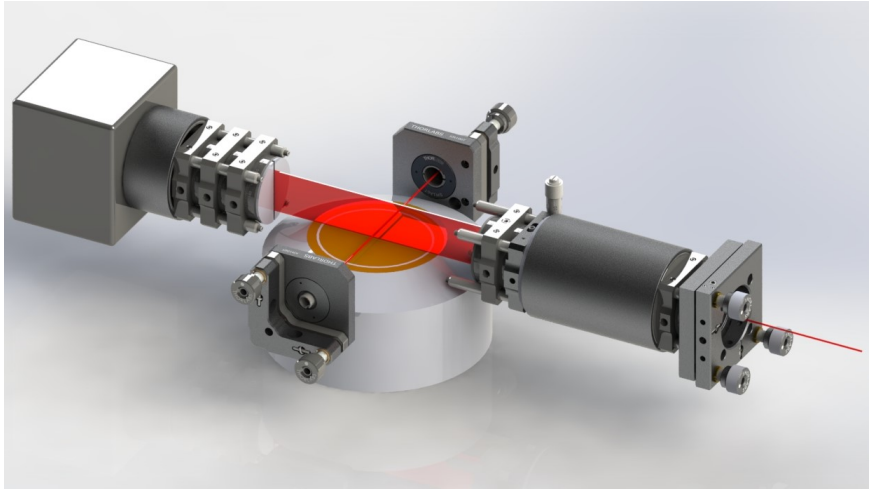

Figure 3.7: The McKenna flat flame burner setup with the laser inserted into a nitrogen sheath, with the center emitting a premixed fuel/oxidizer mixture of air and a test fuel. The experiments completed in this work used methane as a test gas due to its low flame speed and well known exhaust components.

were higher temperature lines. These lines were chosen through the line selection guides which will be described in a Sec. 3.6, but were picked such that the lines were responsive in the high temperature regions of the spectrum. For this experiment, an ILX Laser Diode Controller (LDC) was used to control three DFB laser diodes (NEL NLK1E5EAAA, NEL NLK1E5GAAA, NEL NLK1E5E1AA), which provided access to H_2O transitions from approximately 1380 nm to nearly 1393 nm or 7179 cm^{-1} to 7245 cm^{-1}.

These beams were passed over the burner and the second derivative spectral fitting analysis was performed on the measured spectra. The solutions given by this data are seen in Table 3.1. It should be noted that the HITRAN database used to reconstruct the properties from the data is missing exhaust broadening parameters, causing errors in the inferred fluid properties, though the fits are very accurate. Two representative examples of these fits are seen in Fig. 3.8.

It should be noted that the errors induced by the missing HITRAN parameters are not an indication of any fault in the reconstruction technique, but are a limitation

Linecenter Frequency [cm^{-1}]	T$_{expected}$ [K]	T$_{meas}$ [K]	RMS error
7183	2050	1256	1.74
7199	2050	1787	0.61
7240	2050	1111	1.60

Table 3.1: Analysis of the second derivative data measured over the McKenna Flat Flame burner for a Φ of 0.87. As can be seen, there is still a large error in the solutions due to the incomplete spectral database parameters as well as other inherent noise errors.

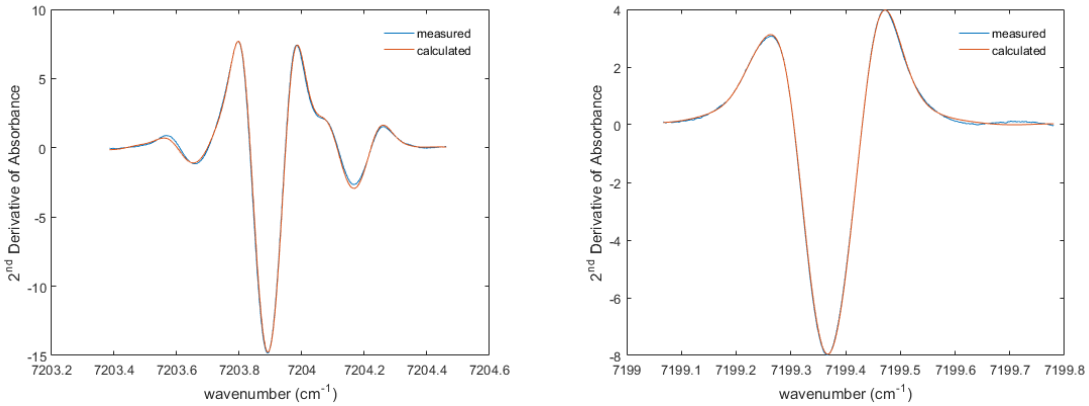

(a) (b)

Figure 3.8: Representative fits of the second derivative of the absorbance spectrum for two transitional lines. It is seen that the fit to the lines is quite accurate although the reconstructed temperature values are fairly erroneous. This is due to the presence of exhaust species in the measurement for which HITRAN has no data.

of the method. In order for the method to be accurate, a good knowledge of the flow conditions and species is needed, as well as a spectral database containing the necessary parameters.

3.5.5 McKenna Flat Flame Burner Conclusions

The McKenna flat Flame Burner tests demonstrate the ability of the second derivative fitting to closely match the absorption profiles of data taken, even in the presence of large baseline errors. The spectra are well fit, as seen in Fig. 3.8, although the solution for the temperatures is incorrect. As stated, this is not an issue with the method itself, as evidenced by the accurate values obtained from ambient and low pressure measurements, which are accurate as seen in Fig. 3.6. This is an effect of the incorrect HITRAN profiles, which are missing the additional exhaust species from combustion. In order to correct for this, the additional species must be accounted for, or an alternate method of processing which is insensitive to flow species must be obtained. A possible path for species insensitivity is given through the Boltzmann Plot, which will be further discussed in the following sections. The determination of an accurate spectral profile in the midst of baseline offset, demonstrates the benefit of this method. However, because the method relies on accurate broadening parameters and knowledge of the absorption line shape, the general use is currently limited to where these values are well known. It is possible, as in [34, 38],for the spectral properties to be documented in the lab prior to running experiments, but this takes time and resources and must be completed for each line which is being probed. The spectral databases are continually being updated, so in the future, these databases could be used once these parameters are included, to probe any line, or set of lines wanted for the second derivative fitting scheme.

3.6 Line Selection

The line selection decisions for second derivative fitting were based on similar criteria to the typical spectral fitting methods for both scanned direct absorption spectroscopy as well as for WMS [72, 80, 81]. The three criteria chosen are as follows:

- Laser scanning range;
- Linestrength;
- Lower state energy;
- Degree of isolation from nearby lines;
- Amount of interference from other absorbing species.

where each of these is an important factor in the usefulness and accuracy of the measurement. The laser scanning range (and subsequently detector range) are necessary in choosing a wavelength region to probe. The selection made for this work is near 1400 nm. This was chosen as an appropriate target wavelength due to its easy accessibility (many off-the-shelf components exist for this region due to recent growth in optical telecommunications networks), the strong water absorption bands available in this region, and because other typical absorbing species do not have interfering bands in this region. Because of this accessibility, designing, building and implementing new systems or modifying currently existing system was very straightforward. Strong water absorption bands allow for high SNR values, as the strength of the transition is directly proportional to the signal measured. Spectrally isolated bands means that the measured transitions are guaranteed to be the result of the probed molecule and do not have additional absorbance (or emissions) from secondary species.

The second criterion is that strong linestrengths are desired in the transitions measured for a given temperature. The linestrength, as seen in Eq. 1.5, is a function

Linecenter [cm^{-1}]	S(T$_o$) $\frac{cm^{-1}}{molec.cm^{-1}}$	S(300 K) $\frac{cm^{-1}}{molec.cm^{-1}}$	S(2000 K) $\frac{cm^{-1}}{molec.cm^{-1}}$
7179.75	1.698e-22	1.8015e-22	8.6409e-22
7182.95	3.77e-21	2.2463e-22	3.7308e-21
7185.60	1.977e-22	2.0743e-22	4.9526e-22
7199.38	8.96e-22	9.3062e-22	1.1742e-21

Table 3.2: Table demonstrating the variation in the linestrength with temperature over several transition lines. It can be seen that these lines may or may not be effective choices due to the variation in linestrength depending on the temperature range expected in the measurement.

of the temperature and some reference linestrength value. It is preferable to measure several transitions with fairly high linestrengths over the expected temperature regions. For this reason, different lines are suitable for different applications. An example of this is seen in Table 3.2, where the lines shown in the left column have the representative linestrengths at 300 K and 2000 K shown in subsequent columns.

The final criterion for line selection is the lower state energy, E''. It is easily demonstrated that the sensitivity of TDLAS measurement techniques to temperature is determined by the difference in the lower state energies of the transitions used [82]. The larger the difference in lower state energies between two or more transitional lines, the more sensitive to temperature a measurement is. This is a common thread in the different reconstruction techniques, from the ratio of integrated areas, to the Boltzmann Plot method. Tabulated in Table 3.3, the lower state energies of the same lines listed in Table 3.2 are given. In order to optimize the sensitivity to temperature, the difference lower state energies between two or more transitions should be maximized.

The linestrength and lower state energy criteria need to be balanced in order to obtain accurate measurements in a system. Observing the linestrengths and lower state energies shows that the optimal line selections for the 300 K case and the 2000 K case are very different. These criteria must be kept in mind and applied correctly for an expected temperature in order that the measurements be accurate, have high

Linecenter [cm^{-1}]	E" [cm^{-1}]
7179.75	1216
7182.95	142
7185.60	1045
7199.38	888

Table 3.3: As seen listed here, the spectral quantity of the lower state energy varies from transition to transition. In order to become insensitive to noise and sensitive to temperature, the difference in the lower state energies between two or more transitions should be maximized.

signal to noise ratios, be sensitive to temperature, and be insensitive to pressure.

3.7 Second Derivative Fitting Conclusions

This chapter focuses on the second derivative fitting technique and comparison to the direct fitting technique. An error equation is described to observe the benefits of second derivative fitting over traditional fitting, to help with line selection by observing the impact of the linestrength on the sensitivities, and to help determine the allowable baseline error in a measurement. For expected temperature and pressure ranges, this equation can be used to determine appropriate transitions and allowable errors within the baseline for any derivative order. Low pressure cell validation measurements are given, demonstrating the reduction in uncertainty of the second derivative fitting over the direct baseline fitting for pressures. McKenna measurements are presented, demonstrating the ability of the second derivative fitting to match the shape of the spectral feature, but, due to the missing broadening parameters for the exhaust species in the flow, recovering inaccurate fluid properties. In order to overcome this limitation, it is necessary to determine an algorithm or technique, which is insensitive to these missing parameters. The Boltzmann Plot Technique provides exactly this, and will be further discussed in Chapter 4.

CHAPTER IV

Extension of the Boltzmann Plot Method for Application with Blended Spectra

The Boltzmann Plot method is a method of property reconstruction which calculates the temperature and partial pressure from a series of measured isolated transitions. This algorithm is used to achieve spectral database insensitive measurements which are both fast and accurate, removing the systematic errors introduced from the poor empirical fits to spectral parameters. This makes this process useful in combustion cases where the exhaust gases compromise the integrity of the spectral and WMS $1f/2f$ fitting techniques, which require accurate knowledge of the gas composition and the proper broadening parameters for each species. The Boltzmann Plot method relies upon obtaining isolated spectra in order to create a Boltzmann Plot for analysis. this is a major disadvantage to the method in high temperature and pressure cases where high temperature lines and pressure broadening can cause interference between neighboring transitions. This chapter will provide a method for the use of aggregate spectra within the framework of a Boltzmann Plot. This not only lets the Boltzmann Plot function over blended spectra, but also allows for the method to be a viable measurement tool in widely varying fluid flow conditions. Because the technique is operable over both isolated and blended spectra, as an experiment transitions through various flow conditions, even if transitions become blended, the data remains usable

for the Aggregate Boltzmann Plot method. This allows the technique to process data in these conditions, a major advantage over the traditional Boltzmann Plot method.

4.1 The Boltzmann Plot Equations

The equations used to process the Boltzmann Plot arise from the definition of the linestrength as well as the integrated absorbance for an isolated spectral feature[83]. The integrated absorption equation given in Eq. 1.23, is taken for a single transition and solved for the linestrength as seen below.

$$S\left(T\right) = \frac{A}{P\chi L} \tag{4.1}$$

setting this equal to the linestrength equation given in Eq. 1.5, gives:

$$\frac{A}{P\chi L} = S(T_o)\frac{Q(T_o)}{Q(T)}e^{-\frac{hcE''}{k}\left(\frac{1}{T}-\frac{1}{T_o}\right)} \tag{4.2}$$

Rearranging this equation leads to the typical Boltzmann Plot form as seen in Eq. 4.3.

$$\ln\left(\frac{A_j}{S_{o,j}}\right) = -\frac{hc}{k}\left(\frac{1}{T}-\frac{1}{T_o}\right)E''_j + \ln\left(\frac{Q(T_o)}{Q(T)}\frac{\chi P\ell}{kT}\right) \tag{4.3}$$

This is the equation of a line containing the points described by the coordinate pair $\left(E''_j, \ln\left(\frac{A_j}{S_{o,j}}\right)\right)$. The spectral quantity of the lower state energy is the x-coordinate in this linear equation, and the y-coordinate is a function of the integrated absorbance and the spectral quantity of the reference linestrength, $S_{o,j}$. The slope of the line is a function of only temperature, while the y-intercept is a function of temperature and pressure. The reference linestrength is obtainable from the HITRAN database. Because the x-coordinate, E''_j, is a spectral quantity, it is unique to each transition and is obtainable directly from the HITRAN database for a given transition. The in-

tegrated area is a measurable quantity through the integration of Beer's Law. Taking the measured values for the integrated absorbance and the spectral database values for the lower state energy and plotting them on an x-y coordinate grid a best fit line through the points can be found. The slope of this line is directly relatable to the temperature through Eq. 4.3. Once the temperature is obtained, the y-intercept can be used to obtain the partial pressure of the absorbing species. The values obtained are averaged by the number of transitional lines measured in the system. An example Boltzmann Plot can be seen in Fig. 1.5, as discussed in Chapter I.

The spectral nature of the lower state energies means that this equation is only usable with isolated transitional lines. If neighboring transitions interfere with the isolated lines, the resulting cluster of lines is blended and is designated as an aggregate spectrum, which is unusable in the current Boltzmann Plot equation method. This is challenging in many flows of interest for aerospace, especially in high temperature and pressure regions, where isolated transitions become much rarer. In high pressure flows, the spectral features are broadened, meaning that previously isolated neighboring transitions can begin to interfere. In high temperature cases, high energy transitions can become prominent, and so spectral features that are isolated at low temperatures can have these high energy transitions appear and cause interference. These challenges cause a gap in which the Boltzmann Plot is unusable, resulting in the need for different analysis techniques.

This section will expand the current Boltzmann Plot technique to include the use of these aggregate (blended) spectra. This is accomplished through redefining the spectral parameters to weighted averages over the aggregate spectral scan. These definitions are used to derive the Aggregate Boltzmann Plot such that the line depends on these aggregate spectral quantities, rather than the typical isolated spectral quantities.

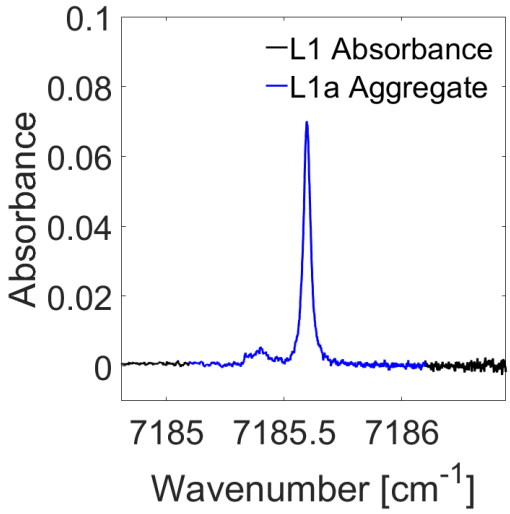

Figure 4.1: Example of a pair of aggregate lines contained entirely within the spectral range ($j \in \Omega$) denoted by the blue region of the spectrum.

4.2 The Modified Equations

The Boltzmann Plot equations have been modified previously for applications in plasma emissions diagnostics. Hornkohl [84] applies a modification of the Boltzmann Plot solution over blended spectra using a single reference point within the cluster, rather than the entire emission feature. This work makes a similar expansion in terms of the absorbance spectra, but additionally includes the entire aggregate absorbance feature. The concept of aggregate quantities is borrowed from Caswell [71]. The spectral quantities of the linestrength and the lower state energies are expanded through this idea to include a weighted spectral quantity. These quantities are taken over a cluster of lines which may or may not overlap, but are able to be fully measured in a single laser sweep. This is seen in Fig. 4.1, where the laser sweep completely covers two nearly isolated spectra. This scan was completed at a low pressure, roughly 30 kPa. At higher pressures, these lines are severely overlapped, resulting in a scan that is not amenable to the traditional Boltzmann Plot. The first of these aggregate quantities is the easiest to classify: the integrated absorbance.

$$A_\Omega = \sum_{j\in\Omega} A_j = \sum_{j\in\Omega} \frac{P\chi\ell}{kT} S_j\left(T\right) = \frac{P\chi\ell}{kT} \sum_{j\in\Omega} S_j\left(T\right) \tag{4.4}$$

Here, Ω represents the spectral band of the laser scan, while j is a particular transition. Thus, it is seen that the aggregate integrated absorbance is merely the product of the optical path length and species number density multiplied by the sum of the linestrengths for each transition contained with the scan area. From this equation, the aggregate linestrength is is defined as the sum of the individual linestrengths of each transition contained within Ω.

$$S_a\left(T\right) = \sum_{j\in\Omega} S_j\left(T\right) \tag{4.5}$$

To obtain the aggregate lower state energy, expand both sides of Eq. 4.5, using aggregate values for spectral quantities in the left hand side of the equation and merely summing the right hand side over all linestrengths of transitions contained within Ω.

$$S_{o,a} \frac{Q(T_o)}{Q(T)} e^{-\frac{hcE_a''}{k}\left(\frac{1}{T}-\frac{1}{T_o}\right)} = \sum_{j\in\Omega} S_{o,j} \frac{Q(T_o)}{Q(T)} e^{-\frac{hcE_j''}{k}\left(\frac{1}{T}-\frac{1}{T_o}\right)} \tag{4.6}$$

Here, the aggregate spectral quantities are denoted by the subscript a, thus, from Eq. 4.5, $S_{o,a}$ is the summation of the reference linestrengths and E_a'' is the aggregate lower state energy. Solving for the lower state energy gives:

$$E_a''\left(T\right) = -\frac{k}{hc} \ln\left[\frac{\sum_{j\in\Omega} S_{o,j} \exp\left(-\frac{hcE_j''}{k}\left(\frac{1}{T}-\frac{1}{T_o}\right)\right)}{S_{a,o}}\right] \left(\frac{1}{T}-\frac{1}{T_o}\right)^{-1} \tag{4.7}$$

The most apparent difference in the lower state energy and the aggregate lower state energy is that, in the traditional measurement technique, the lower state energy is a constant for each spectral transition. Here, the aggregate lower state energy is a

function of temperature rather than being constant like the spectral quantity.

As previously, to re-derive the Aggregate Boltzmann Plot equation, first manipulate the aggregate integrated area equation to obtain the aggregate linestrength.

$$S_a\left(T\right) = \frac{A_\Omega kT}{P\chi\ell} \tag{4.8}$$

This equation is set equal to the aggregate linestrength equation resulting in the following:

$$\ln\left(\frac{A_a}{S_{o,a}}\right) = -\frac{hc}{k}\left(\frac{1}{T} - \frac{1}{T_o}\right)E_a'' + \ln\left(\frac{Q(T_o)}{Q(T)}\frac{\chi P\ell}{kT}\right) \tag{4.9}$$

The Aggregate Boltzmann Plot equation seen in Eq. 4.9 is nearly identical in form to the typical Boltzmann Plot equation seen in Eq. 4.3. There are a few notable differences, including that the spectral quantities are all replaced with the aggregate spectral quantities, and that the lower state energy is now a function of the temperature of the system. As this is no longer a constant, the algorithm for the solution of this Aggregate Boltzmann Plot equation is effectively the same as that for the typical case, but with a slightly more complicated form due to the influence of the temperature on the aggregate lower state energy. This algorithm will be further discussed in the following section.

4.3 Algorithm of the Aggregate Boltzmann Plot Method

Both of the algorithms for solving the typical Boltzmann plot and the Aggregate Boltzmann plot methods are essentially the same. The main difference is that the variation in lower state energy with temperature must be accounted for in order to complete the algorithm.

Similar to the typical solution algorithm, the data is first acquired and Beer's Law is applied to get the spectral features. From these features, the integrated absorbances are obtained for each of the measured aggregate line clusters. For the

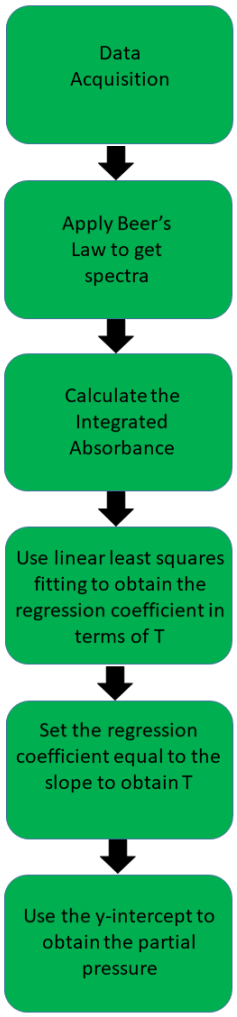

Figure 4.2: The algorithm for the Aggregate Boltzmann Plot method which takes into account the dependence on the temperature of the aggregate lower state energy.

aggregate line clusters obtained, the aggregate lower state energy must be obtained in terms of temperature. This step is different from the typical algorithm, because the temperature dependence of the aggregate lower sate energy must be taken into account, rather than simply calling on the spectral quantity of the lower state energy. Following this, linear least squares fitting is used to obtain the regression coefficient through the set of transitions chosen. This coefficient is a function of temperature, the integrated absorbances, and the width of the scan Ω. The regression coefficient is equivalent to the slope of the Aggregate Boltzmann Plot, which is a function of only the temperature. This equation, seen in Eq. 4.10, is a function only of the measured values and the temperature. In order to obtain the temperature values, a nonlinear least squares fitting is performed to converge to the correct temperature solution.

$$m = \frac{\sum_{i=1}^{n}\left[E''_{a,i}\left(T\right)\ln\frac{A_{\Omega,i}}{S_{a,o,i}}\right] - n\overline{E''_a\left(T\right)}\overline{\ln\left(\frac{A_\Omega}{S_{a,o}}\right)}}{\sum_{i=1}^{n}\left[E''_{a,i}\left(T\right)^2\right] - n\overline{E''_a\left(T\right)}^2} = -\frac{hc}{k}\left(\frac{1}{T} - \frac{1}{T_o}\right) \tag{4.10}$$

Once this temperature is obtained, the y-intercept gives the partial pressure as seen in Eq. 4.11, where b is taken from the y-intercept of the best fit line, the partition function Q is known, and the measurement length is known.

$$b = \ln\left(\frac{Q(T_o)}{Q(T)}\frac{\chi P \ell}{kT}\right) \tag{4.11}$$

In this method, both the temperature and partial pressure can be easily measured. If either pressure or species fraction is known, the other can be inferred. These forms of the equation are scalable for an arbitrary number of aggregate spectral features measured, making it useful for rapidly obtaining averaged flow property data from a large number of measured spectral transitions simultaneously.

4.4 Sensitivity and Error Analysis

In determining the usefulness of this Aggregate Boltzmann Plot, it is beneficial to compare the sensitivities and errors to the typical plot. Ideally, the Aggregate Boltzmann Plot and the traditional Boltzmann Plot methods should have the same, or nearly the same, sensitivities to noise and errors. If not, it needs to be determined where the Aggregate Plot method is valid in order to make good use of the gains made from including aggregate spectral quantities. This sections details the formulation of the sensitivity and error analysis of both the traditional and Aggregate Boltzmann Plots, compares the sensitivities of these methods, and looks at the results of the sensitivities through the use of a numerical Monte Carlo simulation.

4.4.1 Formulation

4.4.1.1 Typical Boltzmann Plot

The typical Boltzmann Plot employs the slope, m, to obtain the temperature. therefor, it is necessary to understand the sensitivity of this slope with temperature to see where the method is sensitive. This is done through taking the derivative of the slope of the Boltzmann Plot with respect to temperature, where the slope is given similarly to Eq. 4.10, merely without the aggregate values. This is seen below

$$m = \frac{\sum_{i=1}^{n}\left[E_i'' \ln \frac{A_i}{S_{o,i}}\right] - n\overline{E''}\overline{\ln\left(\frac{A}{S_o}\right)}}{\sum_{i=1}^{n}\left[E_i''^2\right] - n\overline{E''}^2} = -\frac{hc}{k}\left(\frac{1}{T} - \frac{1}{T_o}\right) \tag{4.12}$$

where the derivative of this slope with respect to the temperature, the sensitivity, is given as:

$$\frac{\mathrm{d}m}{\mathrm{dT}} = \frac{hc}{kT^2} \tag{4.13}$$

One obvious outcome of this equation is that the sensitivity of the slope of the

Boltzmann Plot is proportional to $\frac{1}{T^2}$. This means that the Boltzmann Plot is more sensitive to temperatures in lower temperature ranges, but does not preclude the method from working in higher temperature environments.

Errors can be introduced into the system, which affect the measurement. These errors manifest as an error in the integrated absorbance. This will be shown as follows:

$$A_{meas} = A_{real} + A_{error} = A_{real} + A_{real}\epsilon = A_{real}\left(1+\epsilon\right) \tag{4.14}$$

where the induced error in the measured integrated absorbance is assumed to be some error, ϵ, which is multiplied by the actual area of the integrated transitional line. These types of errors can arise from shot noise in measurements which can affect the accuracy of the measured areas. Additionally, baseline offsets and poor fittings can cause bias in the measured areas through inducing errors in the measured absorbance features. In framing the errors in this manner, Eq. 4.14 allows for simple processing to understand how errors affect the sensitivity of the Boltzmann Plot to temperature and how the measured temperature is affected by these errors. The slope of the Boltzmann Plot becomes a function of the measured spectral area, which includes this new term in place of the ideal integrated absorbance.

$$m = \frac{\sum_{i=1}^{n}\left[E_i''\ln\frac{A_i(1+\epsilon_i)}{S_{o,i}}\right] - n\overline{E''}\overline{\ln\left(\frac{A(1+\epsilon_i)}{S_o}\right)}}{\sum_{i=1}^{n}\left[E_i''^2\right] - n\overline{E''}^2} \tag{4.15}$$

Here, ϵ_i is the relative error associated with some integrated absorbance for a particular transition A_i. Through the use of logarithmic and algebraic manipulation, this reduces to:

$$m = -\frac{hc}{k}\left(\frac{1}{T}-\frac{1}{T_o}\right) + \frac{\sum_{i=1}^{n}\left[E_i''\ln\left(1+\epsilon_i\right)\right] - n\overline{E''}\overline{\ln\left(\left(1+\epsilon_i\right)\right)}}{\sum_{i=1}^{n}\left[E_i''^2\right] - n\overline{E''}^2} \tag{4.16}$$

where the first term on the right hand side of the equation is the true value that would be measured in a perfect system with no error. The second term on the right hand side of the equation represents the contribution of the error into the system. Taking the derivative of the Boltzmann Plot slope with respect to temperature gives the sensitivity of the measurement technique to temperature while accounting for random errors in the integrated absorbance.

$$\frac{\mathrm{d}m}{\mathrm{dT}} = \frac{hc}{kT^2} \tag{4.17}$$

This is identical to the ideal solution, assuming the random errors introduced through the integrated absorbance term are not related to the temperatures being measured. This is beneficial because it means that the sensitivity of the measurement is independent of the errors, providing that the errors are not a function of the temperature.

Taking the derivative of the slope with respect to a particular error, ϵ_i, yields:

$$\frac{\mathrm{d}m}{\mathrm{d}\epsilon_i} = \left(\frac{1}{1+\epsilon_i}\right) \frac{E_i'' - \overline{E''}}{\sum_{i=1}^{n}\left[E_i''^2\right] - n\overline{E''}^2} \tag{4.18}$$

Let Γ be:

$$\Gamma = \frac{\sum_{i=1}^{n}\left[E_i'' \ln\left(1+\epsilon_i\right)\right] - n\overline{E''}\overline{\ln\left(\left(1+\epsilon_i\right)\right)}}{\sum_{i=1}^{n}\left[E_i''^2\right] - n\overline{E''}^2} \tag{4.19}$$

Then

$$m = -\frac{hc}{k}\left(\frac{1}{T_{meas}} - \frac{1}{T_o}\right) = -\frac{hc}{k}\left(\frac{1}{T} - \frac{1}{T_o}\right) + \Gamma \tag{4.20}$$

The sensitivity of the slope to the measured temperature is given as:

$$\frac{\mathrm{d}m}{\mathrm{d}T_{meas}} = \frac{hc}{kT_{meas}^2} \tag{4.21}$$

Using Eq. 4.20

$$\frac{1}{T_{meas}} = \frac{1}{T} - \frac{k}{hc}\Gamma \tag{4.22}$$

leading to:

$$\frac{\mathrm{d}m}{\mathrm{d}T_{meas}} = \frac{hc}{kT^2} + \frac{k}{hc}\Gamma^2 - \frac{2}{T}\Gamma \tag{4.23}$$

where the temperature in Eq. 4.23 is the temperature of the system. Combining these two equations gives the sensitivity of the measured temperature to error introduced from the integrated absorbance.

$$\frac{\mathrm{d}T_{meas}}{\mathrm{d}\epsilon_i} = \left(\frac{1}{1+\epsilon_i}\right)\frac{E_i'' - \overline{E''}}{\sum_{i=1}^{n}\left[E_i''^2\right] - n\overline{E''}^2}\left(\frac{hc}{kT^2} + \frac{k}{hc}\Gamma^2 - \frac{2}{T}\Gamma\right)^{-1} \tag{4.24}$$

It is evident that the measured temperature relies on the errors introduced in the integrated absorbances of each transitional line. Based on the characteristics of these lines, these errors have different effects. Eq. 4.24 is a quick method for checking how the errors of the specific transitional features affect the measurement of the solution. Another note is that in order to obtain a lesser sensitivity across all transitions, the spacing between the transitions should be higher as seen in the denominator.

4.4.1.2 Aggregate Boltzmann Plot

The formulation for the Aggregate Boltzmann Plot is similar to that of the typical Boltzmann Plot, but with a few key difference. First, the aggregate values are used in place of the spectral parameters. Additionally, because the aggregate lower state energy is a function of temperature, the derivatives with respect to temperature are slightly different. taking the same assumption for $A_{\Omega,meas}$ as the same as for Eq. 4.14:

$$A_{\Omega,meas} = A_{\Omega,real}\left(1+\epsilon\right) \tag{4.25}$$

Applying this to Eq. 4.10 yields

$$m = \frac{\sum_{i=1}^{n}\left[E''_{a,i}\left(T\right)\ln\frac{A_{\Omega,i}(1+\epsilon_i)}{S_{a,o,i}}\right] - n\overline{E''_a\left(T\right)}\overline{\ln\left(\frac{A_{\Omega}(1+\epsilon_i)}{S_{a,o}}\right)}}{\sum_{i=1}^{n}\left[E''_{a,i}\left(T\right)^2\right] - n\overline{E''_a\left(T\right)}^2} \tag{4.26}$$

where the temperatures in this equation would be the real temperatures in the system being probed, not the measured temperatures. This is noted to be identical in form to Eq. 4.15, with the aggregate values for the integrated area and the lower state energy. A second point to note is the additional temperature dependence introduced through the aggregate lower state energy.

Reducing this form as with Eq. 4.16, gives the analogous equation for the Aggregate Boltzmann Plot.

$$m = -\frac{hc}{k}\left(\frac{1}{T} - \frac{1}{T_o}\right) + \frac{\sum_{i=1}^{n}\left[E''_{a,i}\left(T\right)\ln\left(1+\epsilon_i\right)\right] - n\overline{E''_a\left(T\right)}\overline{\ln\left(1+\epsilon\right)}}{\sum_{i=1}^{n}\left[E''_{a,i}\left(T\right)^2\right] - n\overline{E''_a\left(T\right)}^2} \tag{4.27}$$

As previously described for the traditional Boltzmann Plot solution, the first term on the right hand side is the ideal solution case with no error. The second term on the right hand side of the equation introduces the relative errors ϵ_i, for particular aggregate integrated absorbance values $A_{\Omega,i}$. Taking the derivative of this equation with respect to the temperature gives the sensitivity of the slope of the Aggregate Boltzmann Plot to the temperature:

$$\frac{\mathrm{d}m}{\mathrm{dT}} = \frac{hc}{kT^2} + \frac{\mathrm{d}}{\mathrm{dT}}\frac{\sum_{i=1}^{n}\left[E''_{a,i}\left(T\right)\ln\left(1+\epsilon_i\right)\right] - n\overline{E''_a\left(T\right)}\overline{\ln\left(1+\epsilon\right)}}{\sum_{i=1}^{n}\left[E''_{a,i}\left(T\right)^2\right] - n\overline{E''_a\left(T\right)}^2} \tag{4.28}$$

Equation 4.28 describes the sensitivity of the Aggregate Boltzmann slope to the temperature. It is immediately evident that the second term on the right hand side of the equation is an additional term when compared with Eq. 4.17. This term arises due to the dependence of the aggregate linestrength on the temperature. This adds a second source by which the sensitivity of the slope can be driven. It is, however,

evident that this term can be reduced by taking aggregate spectral features with large differences in the aggregate lower state energies. Taking the derivative with respect to the error, ϵ_i, of a given integrated area, $A_{\Omega,i}$ gives:

$$\frac{\mathrm{d}m}{\mathrm{d}\epsilon_i} = \left(\frac{1}{1+\epsilon_i}\right) \frac{E''_{a,i}(T) - \overline{E''_a(T)}}{\sum_{i=1}^{n}\left[E''_{a,i}(T)^2\right] - n\overline{E''_a(T)}^2} \tag{4.29}$$

As before, let $\Gamma_a(T)$ be:

$$\Gamma_a(T) = \frac{\sum_{i=1}^{n}\left[E''_{a,i}(T)\ln(1+\epsilon_i)\right] - n\overline{E''_a(T)\ln(1+\epsilon)}}{\sum_{i=1}^{n}\left[E''_{a,i}(T)^2\right] - n\overline{E''_a(T)}^2} \tag{4.30}$$

Then

$$m = -\frac{hc}{k}\left(\frac{1}{T_{meas}} - \frac{1}{T_o}\right) = -\frac{hc}{k}\left(\frac{1}{T} - \frac{1}{T_o}\right) + \Gamma_a(T) \tag{4.31}$$

The sensitivity of the slope to the measured temperature is given as:

$$\frac{\mathrm{d}m}{\mathrm{d}T_{meas}} = \frac{hc}{kT_{meas}^2} \tag{4.32}$$

Using Eq. 4.31

$$\frac{1}{T_{meas}} = \frac{1}{T} - \frac{k}{hc}\Gamma_a(T) \tag{4.33}$$

leading to:

$$\frac{\mathrm{d}m}{\mathrm{d}T_{meas}} = \frac{hc}{kT^2} + \frac{k}{hc}\Gamma_a(T)^2 - \frac{2}{T}\Gamma_a(T) \tag{4.34}$$

As is typical with this analysis, this is identical to the analogous Eq. 4.18, merely with the aggregate values replacing the spectral ones. Again, there is a new dependence on the temperature of the system being measured, but the trends set forth by the equation remain the same: the larger the difference in the lower state energies of the chosen aggregate spectral features, the less sensitive to measurement error the slope becomes. Applying the same idea as previously, the sensitivity of the measured temperature to relative errors ϵ_i in specific aggregate integrated absorptions

$A_{\Omega,i}$ results in:

$$\frac{\mathrm{d}T_{meas}}{\mathrm{d}\epsilon_i} = \left(\frac{1}{1+\epsilon_i}\right) \frac{E''_{a,i}(T) - \overline{E''_a(T)}}{\sum_{i=1}^{n}\left[E''_{a,i}(T)^2\right] - n\overline{E''_a(T)}^2} \left(\frac{hc}{kT^2} + \frac{k}{hc}\Gamma_a(T)^2 - \frac{2}{T}\Gamma_a(T)\right)^{-1} \tag{4.35}$$

Equations 4.24 and 4.35 have the same form. Again, the major difference is the additional dependence on the temperature through the inclusion of the aggregate lower state energy. The general trends set forth by this analysis are identical. By expanding the range of lower state energies, the sensitivity of the typical Boltzmann Plot method's reconstructed temperature to errors in specific integrated areas can be reduced. The same exact trend applies to the Aggregate Boltzmann Plot method using the aggregate integrated areas and aggregate lower state energies. By expanding the range of the aggregate lower state energies, the sensitivity of the Aggregate Boltzmann Plot method's reconstructed temperature to errors in specific aggregate integrated areas can be reduced as well.

4.4.2 Monte Carlo Analysis

These equations are useful in determining the effects of errors on specific lines and how they affect the reconstructed temperatures from measurements with errors. In order to get an idea of the overall effect of these errors within a measurement, a Monte Carlo analysis was completed for conditions that might be of interest in aerospace experimental applications. The setup for this analysis used random Gaussian noise with a standard deviation σ_ϵ from 0.01 to 0.1. All spectral features were assumed to draw from the same set of Gaussian values for each test case, though in actuality, different lines would have different relative errors. If a transition is much stronger, the relative error from inherent system noise would be much smaller than a transition with a weaker linestrength. The Monte Carlo Analysis was run twice, for each case, one set using four aggregate spectral features and one case using eight

aggregate spectral features. This is done to demonstrate the averaging effect of using more transitional clusters to obtain more accurate information. For each value of the standard deviation, ten thousand samples were generated, each drawing errors from the random Gaussian distribution noise and propagating them through the solutions. The reconstruction analysis described previously in Sec. 4.3, for the Aggregate Boltzmann Plot was used to determine the temperatures for each case, and statistical analysis was completed comparing these reconstructed temperatures with those used to generate the spectral features. The mean and standard deviations for the computationally reconstructed temperatures are obtained as a function of the temperature used to generate the transitions and the standard deviation of the Gaussian curve from which the errors are drawn. These mean values and standard deviations are seen in Figs. 4.3 and 4.4 respectively. By every metric tested, the cases with eight aggregate line clusters out-performed the four aggregate line clusters. The mean reconstructed temperatures and the temperature standard deviations were vastly improved over the four aggregate line cases. This is due to the averaging effects inherent to both the Boltzmann Plot and the Aggregate Boltzmann Plot methods, arising from the use of more transitional features. It should be noted in Fig. 4.3 that there exists an offset in the averaged mean temperatures obtained from the processing and the actual temperatures used in generating the spectral features. The difference seen occurs from the non-linear error term $\ln(1+\epsilon)$. The non-linearity of this term skews the dependence on the error induced from inherent random noise in the system. When ϵ is small, this term is approximately linear, but as ϵ grows, the non-linearity of this term becomes much stronger. The sensitivity of the Aggregate Boltzmann Plot to temperature as seen in Eq. 4.28, is apparent in the solutions. As the temperature grows, the sensitivity of the slope, and therefor the measured temperature is lessened. This means that small relative errors in the measurements can induce large errors in the reconstructed temperatures as seen in Fig. 4.4. This figure demonstrates the growth of the standard

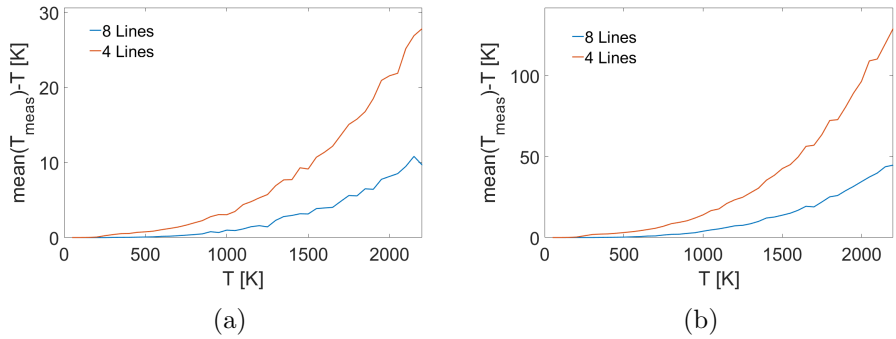

(a) (b)

Figure 4.3: The mean offset of the reconstructed temperature from the actual temperature using (a) $\sigma_\epsilon = 0.03$ and (b) $\sigma_\epsilon = 0.06$. As expected, the more lines used in the reconstruction, the lower the difference in the reconstructed temperatures. Additionally, the higher the error, the larger the skewing of the average temperature due to the non-linearity of the $\ln(1+\epsilon)$ term.

deviation of the reconstructed temperatures with the increasing temperature used to create the simulated spectral features. It should also be noted that the simulation grows exponentially and explodes for the four line case much past σ_ϵ of 6%, but hold valid through 10% for the 8 line case.

4.5 Low Pressure Cell Measurements

As with the second derivative fitting, the Aggregate Boltzmann Plot property reconstruction method was validated in the low pressure cell. The experimental setup was identical to second derivative fitting setup, with the single line pitch and catch optics being passed through the cell, along with a reference beam and an eatlon measurement. Again, the cell was pumped down from ambient conditions, and data was taken at several steps between the start of the evacuation and the near vacuum case. The experimental configuration exactly matched that of the second derivative fitting case, where the pitch and catch optics were mounted on either side of the low pressure cell. The cell was instrumented with an MKS Baratron (Type 626C) and an SK Sato Datalogger which records temperature to within 0.1°Centigrade and

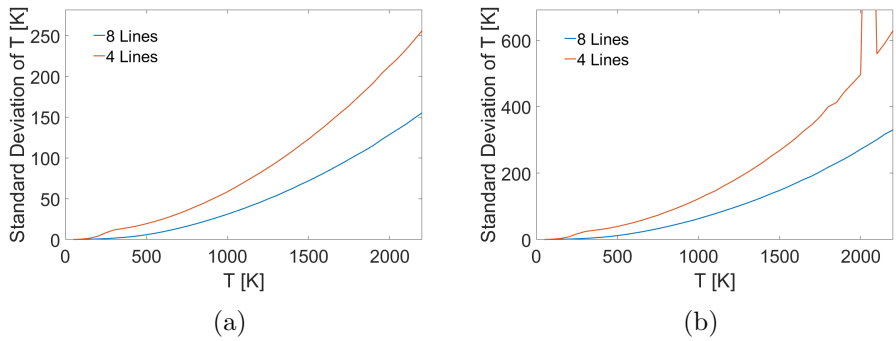

Figure 4.4: Standard deviation of the temperatures obtained through the Aggregate Boltzmann Plot for (a) $\sigma_\epsilon = 0.03$ and (b) $\sigma_\epsilon = 0.06$. As with the mean offset, the higher the initial error standard deviations, the larger standard deviation of the reconstructed temperatuer.

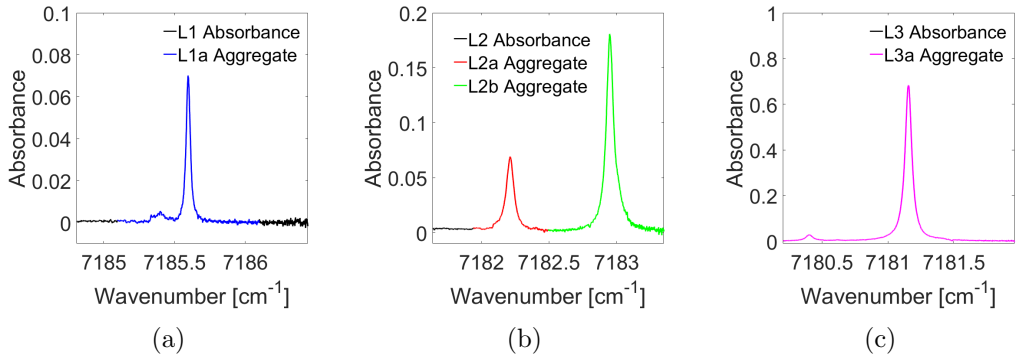

Figure 4.5: Four aggregate clusters used to determine the temperature of the low pressure cell using the Aggregate Boltzmann Plot. Conditions in the cell at the time of recording were approximately 295 K and 30 kPa.

relative humidity to within 0.1%. At each step of the evacuation, the scanned laser beams were passed through the test gas, resulting in a series of measurements with aggregate lines. The laser scan rate was run at 10 Hz. A dark signal was taken with the laser off and used as a background correction dataset, which was subtracted from the scanned values. One hundred of these values were averaged to increase the SNR of the measurements and this averaged value is used in the generation of the Aggregate Boltzmann Plots.

One of the steps in the collection was taken at 30 kPa and 295 K. Four aggregate

spectral line clusters taken at these conditions can be seen in Fig. 4.5. These lines cover the full range of possibilities for aggregate and isolated features, and were chosen as a demonstration set of lines in order to validate the method. In Fig. 4.5(a), the centerline transition for a strong absorption feature falls at roughly 7185.5 cm^{-1}. However, there is a small secondary transition located just next to the main feature, at roughly 7185.4 cm^{-1}. This small feature interferes with the main transition, causing this line pair to be unusable by the traditional Boltzmann Plot method. This feature represents the inclusion of small, but important spectral features, which are often seen in higher temperature cases, when higher energy initial states become populated. The L2a transitional line seen in Fig. 4.5(b), is actually an isolated feature, with no interference from any nearby transitions. This line was included to demonstrate that the Aggregate Boltzmann Plot is capable of functioning with both blended and isolated spectral features. The seemingly isolated transition at 7183 cm^{-1}, L2b, is actually two very closely overlapping spectral features. If closely observed, it is apparent that there is the influence of a large transition and a secondary transition of about half the strength whose centerline frequency is slightly offset to a higher wavenumber than the primary transition. This line represents the aggregate cases of absorbances which closely overlap and are of similar orders of magnitude. The final sub figure, Fig 4.5(c), contains two isolated transitions, separated by a large wavenumber gap. These lines, though isolated, can be treated as an aggregate cluster, as long as both features can be completely covered by a scan. This represents the fourth type of aggregate line that can be used with the Aggregate Boltzmann Plot. These representative aggregate clusters are not necessarily optimized for this set of conditions, but do demonstrate the usefulness of the Aggregate Boltzmann Plot in overcoming the isolated transitional line limitation of the traditional Boltzmann Plot method.

Analysis was performed according to the algorithm provided in the previous sec-

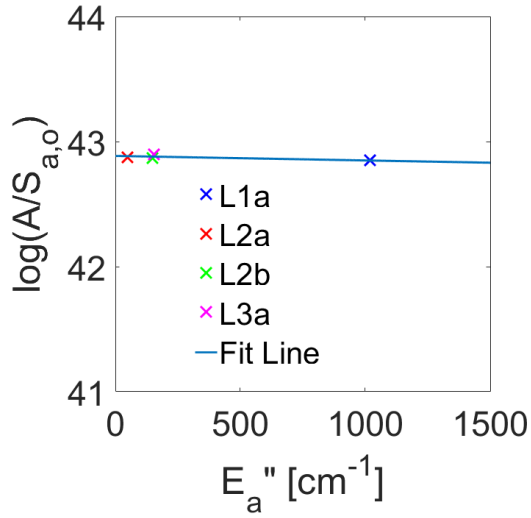

Figure 4.6: Aggregate Boltzmann Plot through the four aggregate lines demonstrated in Fig. 4.5. Note the very high aggregate lower state energy obtained through L1a, reducing the sensitivity of the measurement to errors introduced in the integrated absorbance.

tion where the aggregate integrated absorbance was determined and the temperature was obtained. The measured temperature fell within 1% of the externally referenced temperature obtain from the SK Sato Datalogger. The Aggregate Boltzmann Plot for these lines is shown in Fig. 4.6.

There are several points that should be noted from this plot. The slope of the line is nearly flat. This is due to the fact that the slope is a function of $\left(\frac{1}{T} - \frac{1}{T_o}\right)$, where T_o is the reference temperature at 293 K. Because the temperature of the system and the reference temperature are nearly equal, the slope of the line is approximately flat. A second note is the location of the L1a datapoint. This aggregate line pair has an aggregate lower state energy several times higher than the other three transitional line clusters. This is important due to the sensitivity dependence on the difference in the lower state energies for the traditional Boltzmann Plot and the aggregate lower state energies of the Aggregate Boltzmann Plot. As demonstrated, the larger the difference in the (aggregate) lower state energies, the less sensitive both the Boltzmann

Plot measurement techniques are to noise in a particular transition. Three of the transitions measured could be taken as isolated spectra, but the lower state energies of each would fall on or near the L2a, L2b, and L3a locations, leading to a system of lines whose difference in the lower state energy was near 100 cm^{-1}. The expansion of the Boltzmann Plot method that allows it to include aggregate spectra allows for this new transitional cluster, the L1a line pair, to be used in this reconstruction technique. This vastly expands the $\Delta E_a''$ from approximately 100 cm^{-1} to nearly 1000 cm^{-1}, an order of magnitude difference. This experiment demonstrates both the validity and usefulness due to the expansion of the traditional Boltzmann Plot method to include these aggregate spectra.

4.6 McKenna Burner Measurements

A similar test case was run for the McKenna flat flame burner, with a setup identical to that in Chapter III, using a methane/air flame with an equivalence ratio of $\Phi = 0.87$. This ratio was chosen to mimic previous literature by White[1] using boradband UV LEDs to determine temperature on the same burner at the same equivalence ratio. The tests were run ten times to demonstrate the precision of the method. An example of one of the Boltzmann Plots obtained is seen in Fig. 4.7, where four lines were used to obtain the slope, and therefor the temperature, of the plot.

As state previously, ten of these examples were tested, resulting in the repeated measurement case seen below. In Fig. 4.8, ten datapoints are represented along with the average of the measured data and a comparison line to the Cantera simulation. As can be seen, the agreement between the averaged measurements and the Cantera simulated measurements is quite good, approximately within 3%.

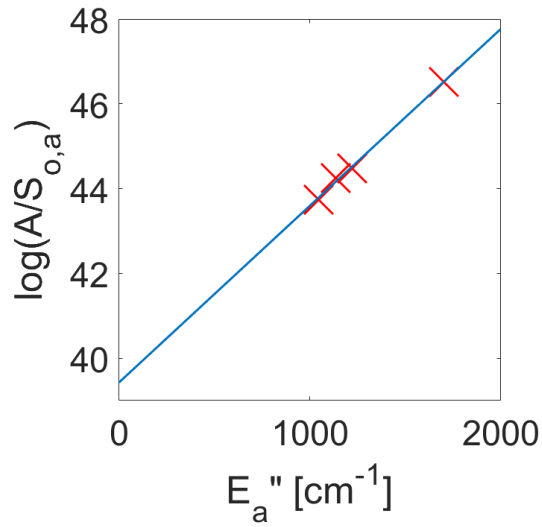

Figure 4.7: Aggregate Boltzmann Plot taken through the McKenna flat flame burner using four aggregate lines. The ΔE_a is large, reducing the sensitivity of the measurement to errors.

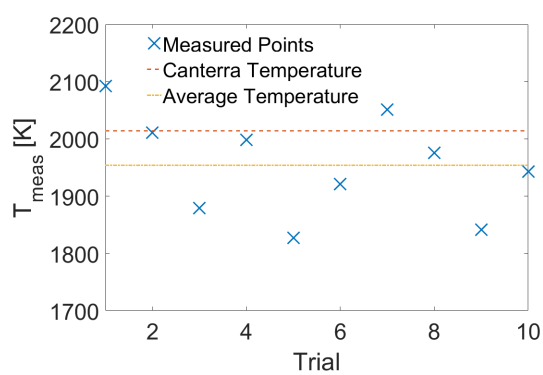

Figure 4.8: Repeated measurements taken through the McKenna flat flame burner and compared to the simulated Cantera temperature at the height above the burner measured.

4.7 Aggregate Line Selections

The spectral transition selection algorithm for the Aggregate Boltzmann Plot is different from the typical line selection algorithms used in either the Boltzmann Plot or the spectral fitting methods. In the spectral fitting method, the line selection criteria are based on the individual lower state energies of the lines in the scan as well as the linestrength. There are no limitations on the blending of the spectra or the width of the scans. For the traditional Boltzmann Plot method, the criteria for line selection include large differences in the individual lower state energies of the transitions selected and large linestrengths, which allows for higher SNRs, resulting in better measurements. The Aggregate Boltzmann Plot transitional line selection algorithm is different from each of these in a few major ways. First, it is the aggregate lower state energy of the blended transition clusters that is the determiner of how sensitive the measurement is, not merely the individual lower state energies of the transitions chosen. This leads to several complications and possible decisions to be made in the line selection algorithm.

4.7.1 Aggregate Line Selection Theory

The first note is that the aggregate lower state energy varies with temperature. This means that one criterion of the line selection for systems is that robust aggregate clusters need to be chosen where the variation in the lower state energy with temperature for that cluster allows for high sensitivity in the particular region of interested being tested. This can be completed through observing how the aggregate lower state energy varies with temperature over the set of clusters picked for the expected temperatures within the system being measured. If the temperature of an experiment is expected to be fairly constant, clusters with high differences in the aggregate lower state energy for the expeted temperature can be chosen to optimize the sensitivity. In experimental systems with expected high variation in temperature, the aggregate

clusters can be carefully chosen such that, over he expected temperature range, the difference in the aggregate lower state energy can be optimized for the set of lines picked. Additionally, the more lines that are used in the measurement, the more robust the Aggregate Boltzmann Plot will be to these changes.

A second important factor is the window width for the selection of aggregate clusters. Varying the window width for the inclusion of more or fewer lines affects the aggregate lower state energy, as well as the temperature dependence of the system of transitional lines chosen. In this style, certain lines can be included or excluded from aggregate clusters at will, in order to manipulate the variation of the lower state energy with the temperature. This allows for robustness to be determined by properly sizing the scan range and aggregate cluster sizes.

A final consideration is the linestrengths of the transitions within an aggregate line cluster. Similarly to the spectral fitting line selection and the traditional Boltzmann Plot line selection algorithms, the strengths of the scanned transitions make a difference in both the accuracy and precision of the reconstructed values. By increasing the strength of the transitions, the SNR of the signal grows, resulting in more precise measurements, while the stronger lines have less effect from the systematic error of baseline measurements, resulting in a higher overall accuracy of the technique. This is important to keep in mind when making decisions on the window sizes of the lines chosen and the expected temperatures of the measurements. Within a certain window range, it is possible to scan across several transitions with very different linestrengths. This means that the effective SNR of the measurement is bounded by the lines which are important to the measurement. Take, for example, an aggregate line cluster with a strong feature at one lower state energy, and a second transition that is an order of magnitude weaker, but at a very different lower state energy. This aggregate pair would have an expected value for the aggregate lower state energy and an aggregate integrated absorbance. However, if the inherent noise in the system overwhelms the

smaller transition, leading to errors in the integrated absorbance, which in turn causes the measurement to be very poor due to the effective SNR difference in the two lines. It is important to have good measurements not dominated by low SNR over the entire scan range, so as to not skew the results of the measurement.

4.7.2 Aggregate Line Selection Results

The region of the H_2O spectrum over which the current laser systems have access has been processed using several different scan widths and temperatures to determine which aggregate transition line clusters will be effective in the various laboratory experiments in which the Aggregate Boltzmann Plot was tested. The initial processing took the full width of the spectrum at several different temperatures and compared the effects of varying the widths of the scans, Ω. By varying the scan widths and applying the aggregate lower state energy equation, it is possible to observe how the aggregate lower state energy varies as a running property across the entire spectrum that is accessible.

4.7.3 Low Pressure Cell

The first of the laboratory experiments was completed in the low pressure cell for validation measurements. The running aggregate lower state energy is obtained for temperatures at approximately 293 K to coincide with the temperatures expected in room air measurements and in the low pressure cell. This can be seen in Figs. 4.9 and 4.10.

Figs. 4.9(a) and 4.10(a) contain the running value for the aggregate lower state energy. It is evident that the broadening of the window width has a smoothing effect on the aggregate lower state energy. This is important to bear in mind as window sizes are chosen. The spectrum is seen in Figs. 4.9(a) and 4.10(a). These are visualizations help with the choosing absorption lines based on the linestrengths. Finally,

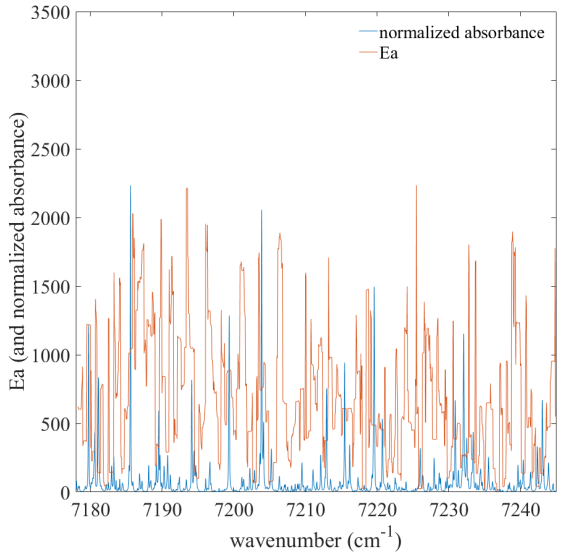

(a)

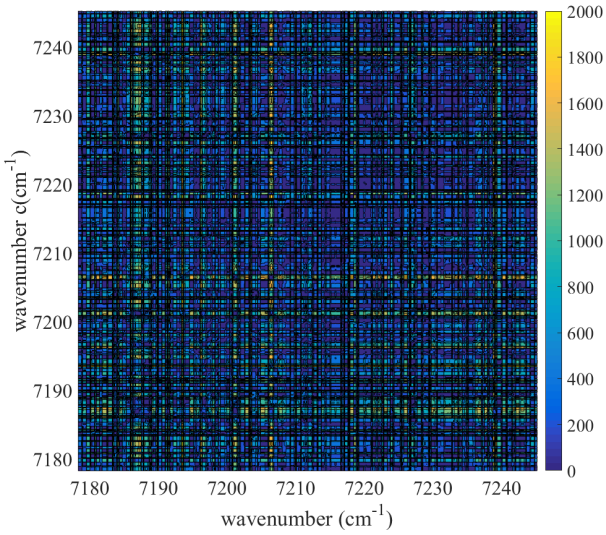

(b)

Figure 4.9: Demonstration of the running value for the aggregate lower state energy as a function of location in the spectrum for a temperature of 300 K and scan width of 0.5 cm^{-1}. The absorption spectrum at the given temperature, used to visualize the strengths of the transition lines, as well as the running aggregate lower state energy is seen in (a). These running aggregate values are generated into matrices and subtracted, giving (b). The bright regions are areas where the aggregate lower state energies are widely spread indicating a potentially useful pair of aggregate spectra.

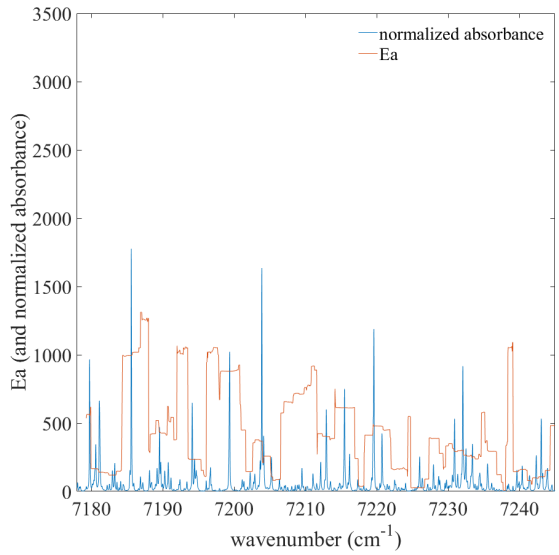

(a)

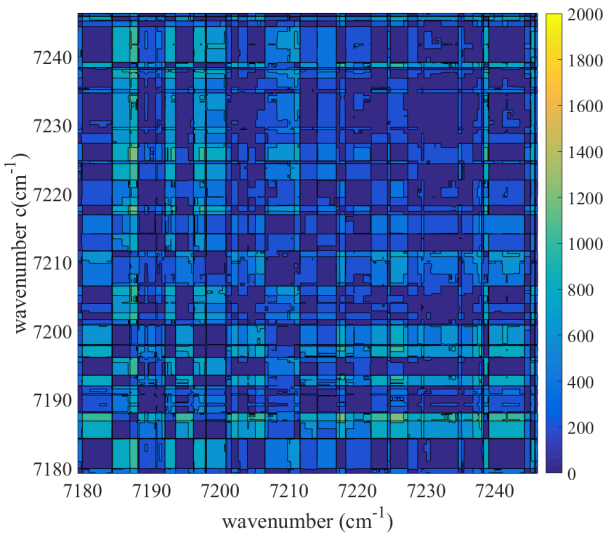

(b)

Figure 4.10: The same setup as Fig. 4.9, but with a window size that is 5 times larger, 2.5 cm^{-1}. There is an evident smoothing effect on the running value of the aggregate lower state energy.

Linecenter [cm^{-1}]	Window Size [cm^{-1}]	E$_a(T)''$ [cm^{-1}]	S$_a$(296) $\frac{cm^{-1}}{molec.cm^{-2}}$
7181	1.75	148	1.5682e-20
7182	0.56	44	1.6046e-21
7183	0.86	144	4.1852e-21
7185	1.0	1011	8.5819e-22

Table 4.1: Aggregate clusters chosen for the low pressure cell experiments. These were used for the relatively large difference in the lower state energies and for populating the Aggregate Boltzmann Plot with strong, easily measured transitions.

the Figs. 4.9(b) and 4.10(b) are hot/cold maps of the differences in aggregate lower state energies of the spectrum. The bright zones represent areas where the difference in the lower state energies is large. This represents a promising line pair. The linestrength of the transitions in these regions is determined, and aggregate line clusters with sufficiently high lower state energy differences and linestrengths are chosen and used. Note that this method gives lines with large differences in lower state energies between two locations in the spectrum, which reduces the sensitivity of the measurements to errors as seen in Eq. 4.35. However, the Aggregate Boltzmann Plot can and should also be populated with intermediate aggregate lower state energies, because, as described in the equations and demonstrated in the Monte Carlo simulations, the more aggregate transition clusters that are used, the better the averaging properties of the Aggregate Boltzmann Plot.

It should also be noted that the Figs. 4.9 and 4.10, the window sizes are the same within each set of subfigures, only changing across the figures. To truly optimize the line selections, different scan widths need to be employed. Drawing from this process, the following aggregate clusters and window sizes were used in the tabletop measurements, seen in Table 4.1. These lines give a relatively wide difference in the maximum and minimum aggregate lower state energies, and several strong transitions which give accurate measurements.

4.7.4 McKenna Burner

For the McKenna Burner, a new set of lines needs to be chosen. This set is at a very different temperature than the low pressure cell. The analysis to determine the optimal line selection was recalculated, using the centered expected temperature values for the McKenna Burner, which was in the range of 1800 K to 2200 K.

The analysis was performed for 2000 K in order to optimize for a set of lines that would been centered in the expected value for the McKenna Burner. The plots, similar to Figs. 4.9 and 4.10, can be seen in Fig. 4.11.

The same analysis style was tested, with Figs. 4.11(a) and 4.12(a) demonstrating the aggregate lower state energy for a given window size for the two different plots. Again, it is evident that the broader the window size, the smoother the aggregate lower state energy. Figs. 4.11(a) and 4.12(a) displays the spectra given at 2000 K. This is used to observe the relative strength of the aggregate absorption spectra. Figs. 4.11(b) and 4.12(b) are the hot/cold image for the difference in the aggregate lower state energies, as before, the brighter the point in the image, the larger the difference in the lower state energies of the two aggregate spectra chosen. It is evident when comparing the figures of the same window size but different temperatures, such as Fig. 4.9 and 4.11, that the optimal lines for insensitivity to the errors within the system are different. These plots represent different temperatures, and, due to the variation in the aggregate lower state energy with the temperature, the largest differences occur at different values. This is due, in part, to the large discrepancey in these cases: 300 K and 2000 K. For the line selection case on the McKenna Flat Flame burner, the lines chosen are seen in Table 4.2.

The lines in Table 4.2 represent a large difference in the aggregate lower state energies, while maintaining the necessary linestrengths to observe measurements with ample SNR values. The secondary lines are absorption features with high linestrengths at the given temperature, set up to populate the Boltzmann Plot with lines of sufficient

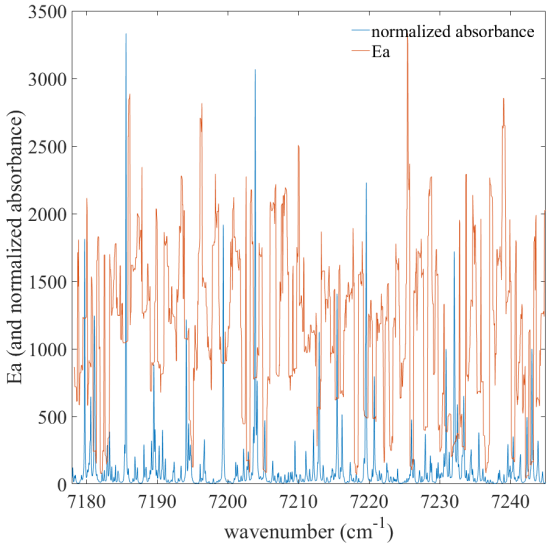

(a)

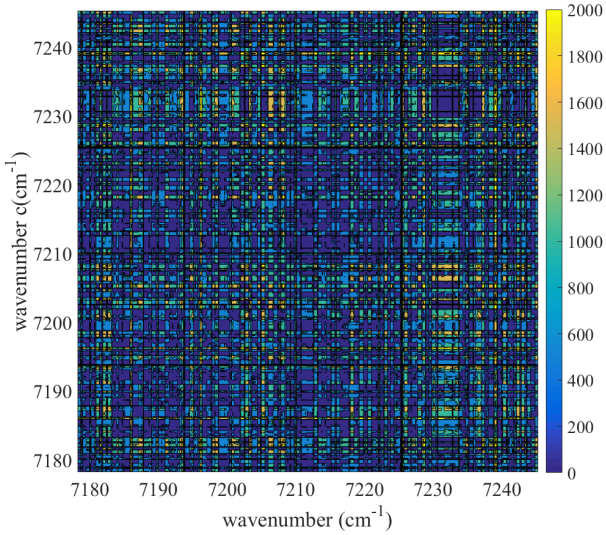

(b)

Figure 4.11: Demonstration of the running value for the aggregate lower state energy as a function of location in the spectrum for a temperature of 2000 K and scan width of 0.5 cm^{-1}. The absorption spectrum at the given temperature, used to visualize the strengths of the transition lines, as well as the running aggregate lower state energy is seen in (a). These running aggregate values are generated into matrices and subtracted, giving (b). The bright regions are areas where the aggregate lower state energies are widely spread indicating a potentially useful pair of aggregate spectra.

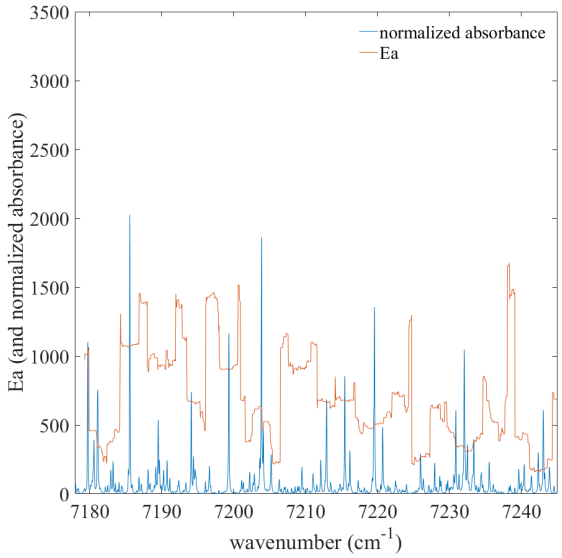

(a)

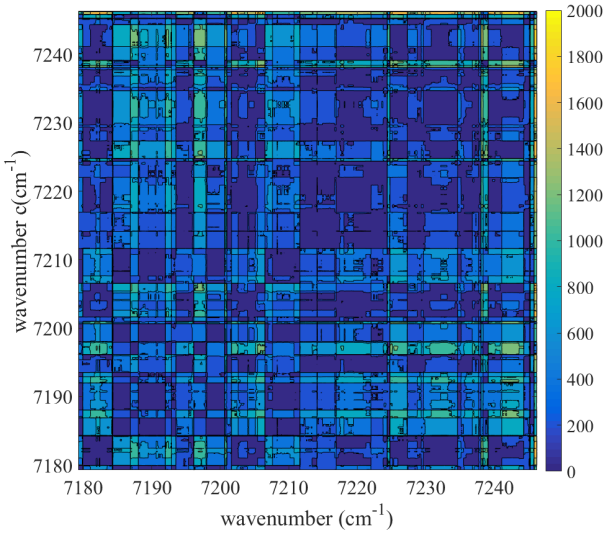

(b)

Figure 4.12: The same setup as Fig. 4.9, but with a window size hat is 5 times larger. It is evident that there is a smoothing effect on the running value of the aggregate lower state energy.

Linecenter [cm^{-1}]	Window Size [cm^{-1}]	E$_a(T)''$ [cm^{-1}]	S$_a$(296) $\frac{cm^{-1}}{molec.cm^{-2}}$
7179.8	0.2	1222	2.3097e-22
7183.3	0.1	1715	7.7240e-24
7185.5	0.4	1046	38.5740e-22
7212.2	0.3	1133	1.0305e-22

Table 4.2: Aggregate clusters chosen for the McKenna. These were used for the relatively large difference in the Lower state energies and for populating the Aggregate Boltzmann Plot with strong, easily measured transitions.

SNR in order to obtain enough lines for a sufficiently averaged measurement.

It is immediately evident that the lines selected for the two different temperature experiments are not the same. The optimization for the line selections resulted in different choices for the centerline frequencies of the aggregate spetral windows. These experiments demonstrate the need to perform this optimization for the different expected temperatures in a laboratory setup. Another option would be to choose aggregate spectral features such that the method is robust over a wide range of temperatures.

CHAPTER V

A Robust Sensing Technique Combining Second Derivative Fitting and the Aggregate Boltzmann Plot Method

While both the second derivative fitting algorithm and the Aggregate Boltzmann plot method have many benefits, there are also several challenges. The second derivative fitting algorithm is dependent on the spectral database having the accurate parameters, but is very accurate for fitting the proper shape of the absorption curve. The Aggregate Boltzmann plot method is insensitive to the spectral database parameters that are often missing, but requires very accurate spectral lineshape measurements. Each of the two techniques have specific error rejection properties that can help overcome common problems associated with TDLAS. This section presents a novel combination of these two techniques, which takes the baseline error rejection benefits from the second derivative fitting algorithm and combines them with the spectral database insensitivity of the Aggregate Boltzmann plot method, and the detriments of neither method, to make a robust sensing technique. This technique is applied to reduce the systematic errors introduced into the inferred properties through the poorly measured calibration measurements of the baseline and the spectral broadening parameters. The result of this is a gain in the accuracy of the mean of the

inferred properties when compared to previous data from White [1] and the expected properties obtained from Cantera simulations.

One of the largest benefits of this technique is the ability to measure large variations in properties in the course of a single data set. Typically, each measurement method is limited to specific applications. The Boltzmann plot method requires isolated spectra, which can change rapidly with fluctuations in the properties of the flow. If the pressure varies, two neighboring spectral absorption lines can transition from isolated to blended in the course of a single measurement. If the temperature increases, then high energy absorption lines can arise and blend with isolated lines. The second derivative method requires accurate knowledge of the flow species and their parameters. If combustion changes over the course of a scan, such as in a combustion engine, during engine unstart, or in a Rotating Detonation Engine (RDE), the flow conditions can rapidly vary in a brief time. This makes accurate reconstruction with the second derivative method challenging, as the exact conditions and species within the flow are unknown. Through combining the second derivative method with the Aggregate Boltzmann plot method, these issues can be conveniently resolved, resulting in a measurement that is not only insensitive to baseline and database errors, but is robust in the sense that rapidly varying properties of the flowfield can be measured swiftly and accurately with a single setup.

5.1 Description of the Algorithm

The algorithm for the novel, robust sensing technique employs both the second derivative method and the Aggregate Boltzmann plot method in order to obtain the benefits from both without the problems associated with either. The full algorithm is seen in Fig. 5.1.

In this algorithm, the first task is to acquire the data by the typical scanned wavelength direct absorption spectroscopy method, which allows for the absorbance

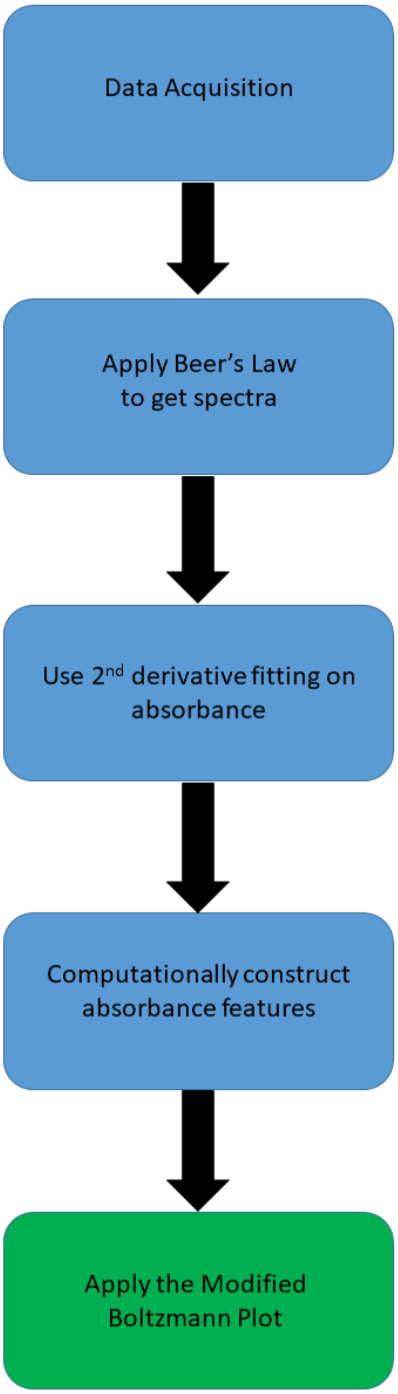

Figure 5.1: Algorithm for the robust sensing method that combines the second derivative fitting and the Aggregate Boltzmann plot method. The resulting method is insensitive to both baseline fitting errors and spectral database errors.

to be measured with either a fitted or measured baseline. These baseline estimates will introduce errors into the measurement whenever Beer's Law is applied. The second step is to use the second derivative fitting in order to obtain an accurate spectral profile. Due to the lack of exhaust species parameters, the reconstructed properties from this method will be inaccurate as described in Sec. 3.4. However, the lineshape produced by the second derivative fitting algorithm will be a faithful approximation of the true absorption lineshape, as this method is intended to reject errors due to the baseline.

The shape can be computationally constructed using the fitting parameters obtained from the second derivative fitting to get an accurate approximation of the actual transitional line shape. This is completed for a number of different transitional lines, which are then taken and used in the Aggregate Boltzmann plot method which is insensitive to the incorrect spectral database parameters. This leads to a robust measurement technique that takes the benefits of both the second derivative fitting algorithm – the baseline noise rejection and the Aggregate Boltzmann plot method – the spectral database error rejection and generates a technique that mitigates the error sources in both constituent techniques by applying them in this particular order. The following section will demonstrate the usefulness of this technique through tabletop low pressure cell experiments and through measurements on a McKenna flat flame burner.

5.2 Low Pressure Cell Validation

This composite technique has been applied to measure values in the low pressure cell for validation purposes. Taking the data used previously and applying the second derivative fitting alone gives fairly accurate information when solved simultaneously across the four lines chosen, as seen in Table 5.1. In this solution, pressure, temperature and mole fraction were solved for simultaneously, where there were no

Linecenter [cm^{-1}]	T_{meas} [K]	T_{calc} [K] @ 99 kPa	T_{calc} [K] @ 30 kPa
L3a (7181 cm^{-1})	294	312	125
L2b (7182.3 cm^{-1})	294	157	226
L2a (7183 cm^{-1})	294	271	345
L1a (7185.5 cm^{-1})	294	257	220
simultaneous solution	294	281	295

Table 5.1: Representative table of the fit properties from the second derivative fitting algorithm in the low pressure cell in two different pressures, 99 kPa and 30 kPa for the lines chosen according to Sec. 4.7.3.

assumptions made about the gas properties in the low pressure cell. On the relatively isolated lines, the errors induced by the properties are able to cancel, allowing for a minimization point far from the ideal solution when the lines are measured individually. When all four aggregate clusters are solved simultaneously, however, the ideal solution is regained. The Aggregate Boltzmann plot method was determined using the poor reconstructed properties for each line, which gives the best fit solution to the individual transitions measured as a demonstration of how the combined second derivative fitting for the shape of the absorbance spectra can be used, even when poor properties are initially obtained from the fitting.

The non-ideal properties are used to computationally construct absorption features with accurate shapes, as determined by the best fit using pressure, temperature and species fraction. A set of these can be seen in Fig. 5.2. Here, the computationally reconstructed absorption features closely match the actual measured curves. The effect of this is that the Aggregate Boltzmann plot method should also match. The Boltzmann plot is seen in Fig. 5.3, where the values given from this plot are 300 K for the 99 kPa case and 299 K for the 30 kPa case. When using the integrated absorbances from the transitions reconstructed with the second derivative properties listed in Table 5.1, these match closely with the actual measured values using the MKS Baratron (Type 626C) and an SK Sato Datalogger, within 2% error for each of the two pressure cases, even though the error in the properties used to reconstruct

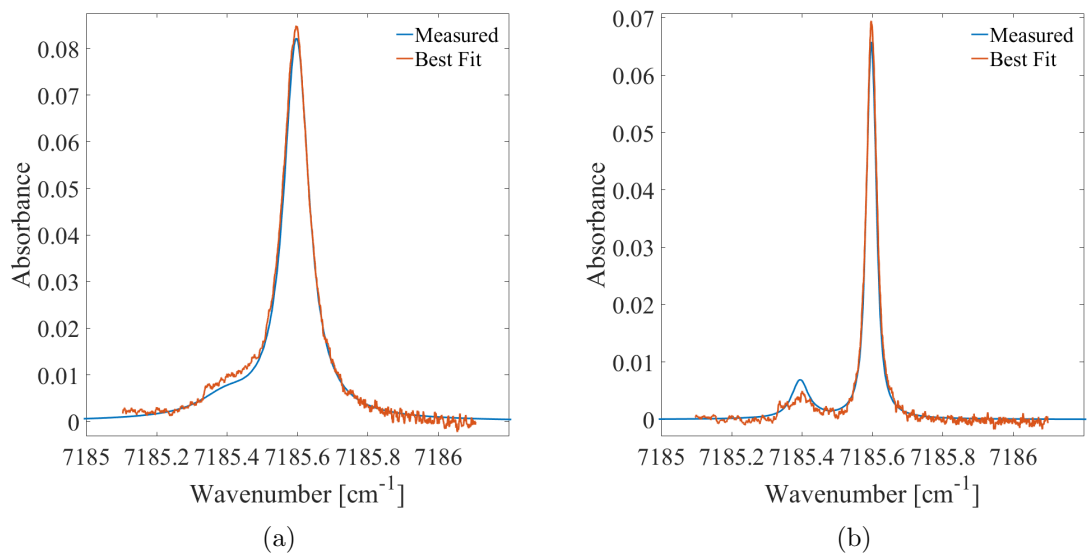

Figure 5.2: Computationally constructed absorbance features created with the reconstructed properties obtained from the second derivative fitting for (a) 99 kPa and (b) 30 kPa for a linecenter frequency of 7185 cm^{-1}. The agreement is quite good despite the poor properties used, leading to an accurate shape.

the spectral transitions were up to 50%. This is due to the close matching of the spectral line shape by the second derivative fitting and the fact that the properties obtained from the Aggregate Boltzmann plot method are only dependent upon the shape of the transitions.

5.3 Improvements over the Individual Methods Over the McKenna Flat Flame Burner

The McKenna burner was again tested for an equivalence ratio of 0.87 for a methane-air flame. A data set was taken over a 0.6 s time frame resulting in 100 measurements for each line. These were passed through a running average of 50 scans resulting in 50 temporal reconstructions for the temperature. In order to demonstrate the effectiveness of the combined method, the data used is processed using both the second derivative method without the database parameter insensitivity of the Ag-

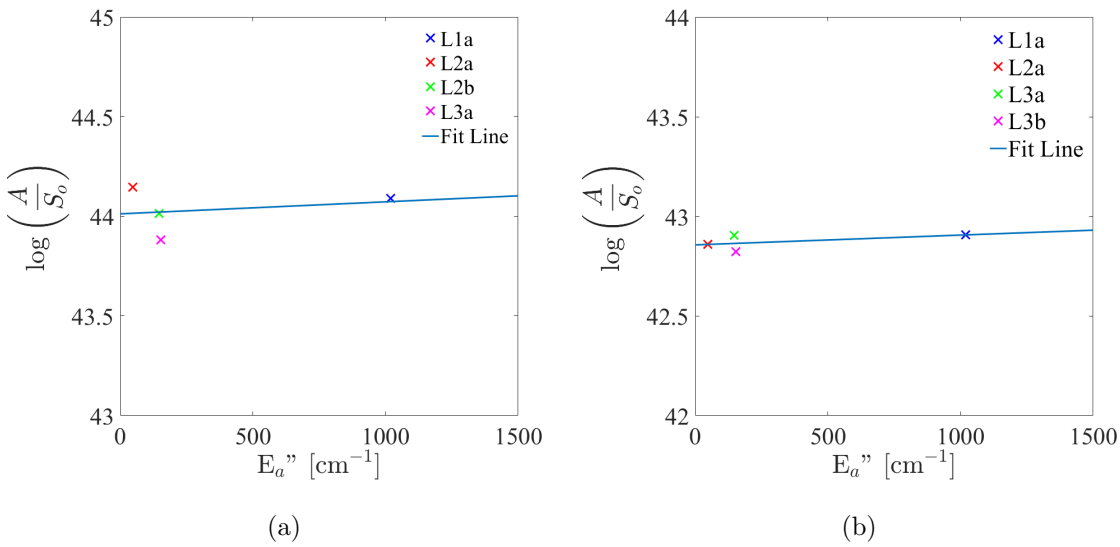

Figure 5.3: The Aggregate Boltzmann Plot calculated with the computationally constructed low pressure cell measurement values for (a) 99 kPa and (b) 30 kPa for a linecenter frequency of 7185 cm^{-1}. It can be seen that the slope is approximately equivalent for the two methods, but due to the different pressures measured, the y-intercept is different between the two plots.

gregate Boltzmann plot method and the Boltzmann plot method with the baseline rejection benefits of the second derivative analysis. An experiment was performed over the McKenna flat flame burner for this purpose. The standard McKenna burner setup for the single line as described in Chapter III is used, but with a MEMS switch used to time multiplex the signals from the three TDLs discussed in Chapter III. The benefit of this switch is that the lines are probed nearly simultaneously, but the drawback of this method is that only three transitions are probed resulting in poorer Aggregate Boltzmann Plot method results. The lines probed for this measurement case are 7183 cm^{-2}, 7199 cm^{-2}, and 7240 cm^{-2}. These three lines were chosen based on the line selection algorithms given in the previous chapters optimizing for one line from each of the ranges of the three lasers used.

The second derivative method gives the values seen in Table 5.2. It can be seen that the variance of the solutions is large across the four different lines tested. This

Linecenter [cm^{-1}]	$T_{expected}$ [K]	T_{meas} [K]	2nd Derivative RMS error [cm^{-2}]
7183	2050	1256	1.74
7199	2050	1787	0.61
7240	2050	1111	1.60

Table 5.2: Table of the fit properties from the second derivative fitting algorithm in the McKenna burner without the benefits of the Aggregate Boltzmann Plot database error rejection. The RMS error is given to demonstrate the accuracy of the fit to the lines.

is due to the improper database values, which are missing the critical parameters for broadening introduced by the exhaust gas species. However, the RMS error between the curve fits is very low, meaning that even though the spectral database contains incorrect parameters, the reconstructed properties are such that the shape of the curve fit is a very close approximation to the actual absorption feature.

The Aggregate Boltzmann plot method is completed across all three lines without the additional benefits of the baseline rejection of the second derivative method. The resulting Boltzmann plot is seen in Fig. 5.4. The reconstructed temperature from this plot gives 1200 K, which is very different than the expected temperature at this location. This is the lower limit of the reconstruction bounds in the MATLAB code used to solve the problem, thus the inferred temperature would have been in even greater error without this analysis limit. The errors arise form the inclusion of the baseline errors in the determination of the integrated aggregate absorbance used to determine the slope of the line. It is important to note that the discrepancy with the accuracy of the inferred temperatures from Chapter IV arises from the difference in the transitions probed, which were optimized for a single transition per laser rather than several transitions per laser as in Chapter IV. This introduction of error causes the measurement to fail. It is clear that the composite Aggregate Boltzmann plot method with second derivative fitting technique has a much better fit to the data points, with an inferred temperature of approximately 2150 K.

The second derivative method was completed, minimizing the errors across the full

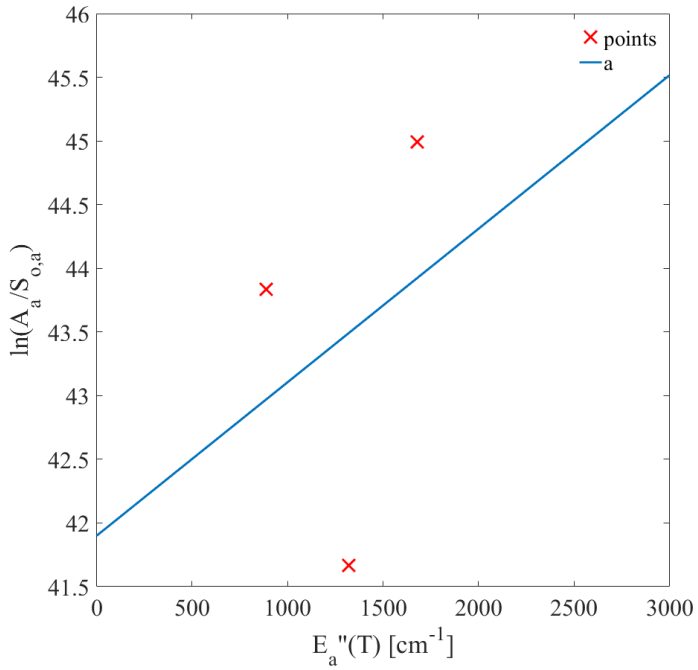

Figure 5.4: The Aggregate Boltzmann Plot given for the lines described in Table 5.2 when used with the raw data rather than using the second derivative fitting to reduce the background and baseline errors. The reconstructed temperature from this plot demonstrates the ineffectiveness of this method to complete measurements in the presence of high background and baseline errors.

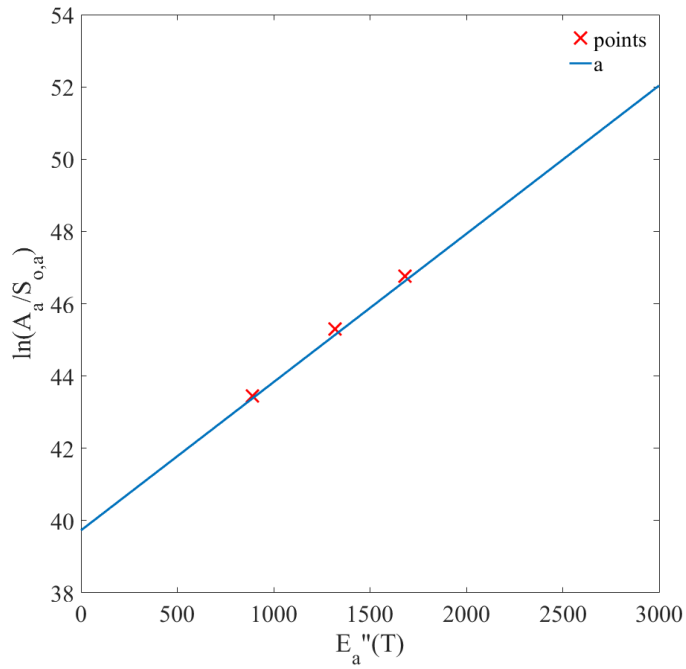

Figure 5.5: The Aggregate Boltzmann Plot given for the lines described in Table 5.2 when used with the accompanying second derivative fitting data. The reconstructed temperature from this plot demonstrates the effectiveness of this method to complete measurements in the presence of high background and baseline errors when coupled with the second derivative fitting.

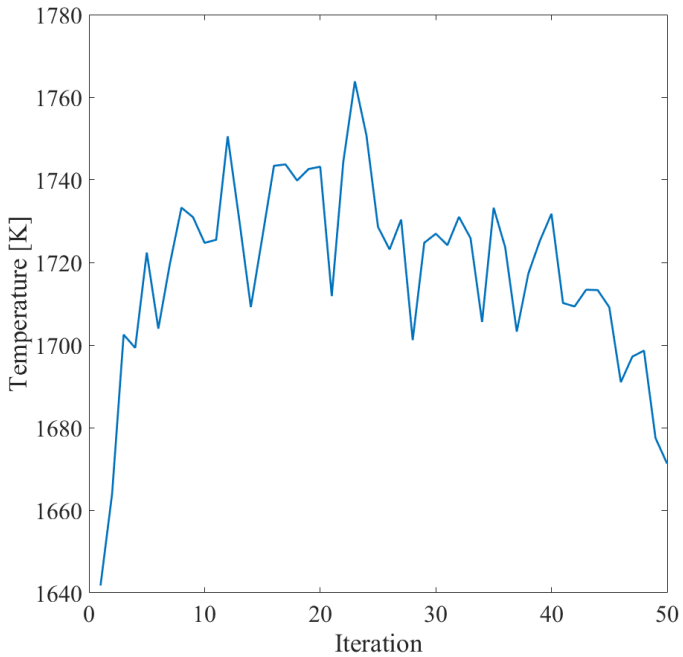

Figure 5.6: The simultaneous solution for the three lines demonstrated in Table 5.2 using the second derivative only. The agreement with the expected value is far better than with the Aggregate Boltzmann Plot alone, due to the excess error introduced by baseline offsets. However, the mean measured temperature has approximately a 15% difference than the expected temperature from White [1] and Cantera due to incorrect HITRAN broadening parameters.

set of lines simultaneously to obtain a best fit temperature to the data set as a whole. Following this approach, the temperature and species fraction were used to obtain best fit second derivatives for the lines individually, which were then used to reconstruct the spectral features for use in the Aggregate Boltzmann plot method. Previous work by White et al. [1] and flames calculations in Cantera suggest a flame temperature of approximately 2050 K for a methane-air flame with an equivalence ratio of 0.87. As can be seen in Figs. 5.6 and 5.7, the measured temperatures across the time frame are fairly constant, but the robust combination of the second derivative fitting and the Aggregate Boltzmann plot method together gives much better agreement with the expected value of the temperature. The data collected had large baseline introduced

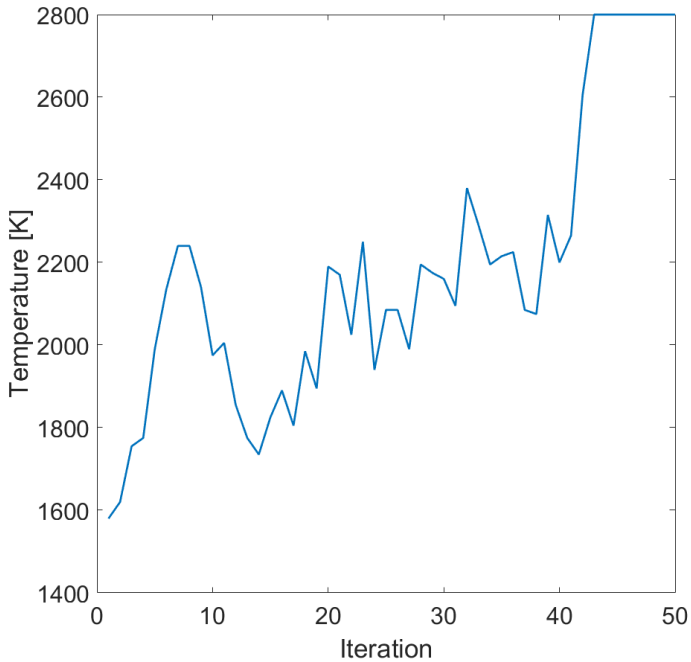

Figure 5.7: The Aggregate Boltzmann Plot temperature solution for the three lines described in Table 5.2 when used with the accompanying second derivative fitting data. The temperatures seen are much closer to the expected values of 2050 K, with the mean temperature within 6% of the expected temperature. The solution can be seen to explode in the final points of the plot, possibly due to increased errors as the optics began to heat up.

errors, resulting in poor temperatures obtained by simply applying the Aggregate Boltzmann plot method on the raw data resulting in reconstructed temperatures of less than 1200 K. The second derivative fitting performed much better resulting in inferred temperatures with a mean of approximately 1750 K, which is within 15% of the expected value from Cantera and White [1], with the systematic errors arising from the poor database parameters.

The errors demonstrated in these two measurement cases reveal the necessity for this combined method for solving for the properties using both the second derivative and the Aggregate Boltzmann plot methods. The combination of these two methods in this order of application allows for the baseline rejection of the second derivative method and the database error rejection of the Aggregate Boltzmann plot method to both be realized. The strengths of both techniques are used and the negatives of both are mitigated, resulting in measurements that are very accurate, with a mean of the reconstructed temperatures of approximately 2150 K, within about 6% of the expected values with a fluctuation of about 10% through the measurement. This robust measurement technique allows for data to be collected in a wide range of cases with insensitivity to background and baseline errors.

5.4 Conclusions

The combined second derivative and Aggregate Boltzmann plot method is presented here. The method is validated in the low pressure cell, with good agreement reached between the measured values within the cell and the inferred values from the combined method. These are comparable to the inferred properties when using purely the second derivative fitting, which is applicable in this case as the spectral database parameters are well known for the gas species in the cell. Data is then taken over a McKenna flat flame burner, and all three techniques, the second derivative fitting, the Aggregate Boltzmann plot method, and the combined algorithm, are tested and

compared. It is seen that the men of the temperatures inferred from second derivative fitting when performed over the three lines probed matches the expected temperature to approximately 15%, while the Aggregate Boltzmann plot method alone is in greater than 50% error for the probed lines when compared to the expected temperatures. By combining the two methods, the average temperature inferred is within 2% of the expected value, with a variation about the mean of approximately 10% over the majority of the test time.

CHAPTER VI

Conclusions and Future Work

6.1 Conclusions

This work explores novel instrumentation and techniques for processing data. This is broken up into the following main contributions: (1) the introduction of the Linear Array Camera for space and time resolved measurements; (2) the novel application of second derivative fitting for suppressing certain measurement errors; (3) the extension of the Boltzmann plot method for use in blended spectra situations, which is more likely to occur in practical situations and thus allows its use over a broader range of flow regimes; and (4) the combination of the second derivative fitting and Aggregate Boltzmann plot method to obtain a robust processing algorithm that contains the baseline insensitivity from the second derivative fitting technique, while remaining insensitive to poor or missing spectral broadening parameters because of the use of the Aggregate Boltzmann plot method and being applicable in elevated pressure and high temperature situations where spectral blending of nearby absorption lines occurs.

6.1.1 The LAC Description and Analysis

The LAC is introduced as a potential instrumentation technique to replace the single beam measurement methods. The two typical methods are either highly resolved in space or time, but not both. In typical applications, high spatial resolution is ac-

quired through a movable laser system which allows for measurements to be taken at varying locations through a system, but at the cost of the time it takes for the translation of the laser stage. High temporal measurements come from passing many beams through a system simultaneously, but comes at the cost of spatial resolution due to the physical size constraints of the pitch and catch optics. The LAC overcomes these issues through the implementation of sheet forming optics and a linear array of pixels with a spatial resolution of 1024 pixels per inch. These pixels can simultaneously sample the laser sheet resulting in high spatial and temporal measurements.

The LAC instrumentation is able to obtain spectral data over the laser sheet scan. This is measured as a spectral image, in which each pixel gives an absorbance profile. These profiles are then used to obtain the flow parameters at very high spatial resolutions. Initial instrumentation setups with the LAC induced large etalon effects. In the presence of these etalon effects, the inferred properties of the flow varied significantly from the externally reference properties. Dependent upon the strength of the etalon signal, the inferred temperature differed by up to 17%, the inferred pressure differed by up to 35%, and the inferred species fraction differed by up to 38% from the referenced quantities. With the implementation of the anamorphic prism pairs, the inferred properties matched much more closely, to within 2% for the inferred temperature, 8% for the inferred pressures, and 4% for the inferred species fraction when compared to the reference measurements. These demonstrate significant improvements over the measurements obtained using the plano-concave and plano-convex lenses.

The LAC was also corrected for structural vibrational issues through post processing realignment of the rising edge of the laser sheet and through expanding the laser sheet thickness. By correcting the image by the rising edge of the laser sheet, the in plane vibrational effects can be corrected without additional changes to the experimental setup. An analytical model was presented in order to help in the design

of the laser sheet thickness in order to mitigate the out of plane vibrational effects in the spectral images. This model agrees well with the measured data. Through the application of the expanded beam, the structural vibrational noise can be effectively mitigated, falling within the inherent noise of the system. The application of these two corrections simultaneously can general spectral images which are effective free from vibrational noise, as seen in Table 2.3.

The current limiting factor on the LAC is beamsteering, which has not been fully overcome. In the presence of density gradients, the path of light is deformed. Traditional single line optics can correct for this through large catch optics and large detector faces. The LAC is limited in both of these categories, making it challenging for the LAC to function in the presence of high density gradients. If the density gradients are a function of truly random fluctuations within the flow field, averaging many spectral images over time can alleviate the sensitivity of the measurement method to beamsteering. This method was tested with limited success, leading to the necessity of a better method for mitigating the beamsteering in the LAC system. Once this has been completed, the LAC will be a more fully robust measurement technique.

6.1.2 Second Derivative Fitting and the Aggregate Boltzmann Plot Method

Currently, one of the most common measurement techniques is Wavelength Modulation Spectroscopy (WMS). It is able to obtain noise and baseline insensitive data for fitting measurements. For this technique to be viable, the sampling rate of a detector system needs to be fairly high. This is not possible in some systems, such as the LAC, which is sampling rate limited to approximately 92 kHz. To combat this limitation, the second derivative fitting scheme is applied to measurement data to recover the baseline insensitivity of the WMS $2f$ method, but applied in wavenumber space on the absorption feature, rather than in Fourier space as the data is taken with

a lock-in amplifier. An error analysis to determine the sensitivity of any derivative spectral fitting technique is provided and the sensitivity of the technique to solutions and error terms is discussed. This is a minimization equation for an arbitrary transition or set of transitions, which computes the error between measured transition and a modeled transition, which includes a baseline error term. This equation minimizes the difference between the spectra, but not necessarily between the true and inferred flow parameters. This equation allows for the determination of the effects of taking different derivative orders in the presence of baseline errors. Over a typical set of measurement values on the 7242.37 cm^{-1} transition, it can be seen that the sensitivity to the solutions terms can increase by a factor of 240, while the dependence on the error terms can decrease by a factor of $2x10^{-4}$ for the second derivative over the spectral fitting scheme. The equation allows for cases to be analyzed for any arbitrary line, baseline error, and expected flow parameter range. This equation does not include the inherent system noise, it only observes the baseline errors. Additionally, it assumes an accurate model for the transitional lineshape. Errors in the model, such as poor or missing broadening parameters, can induce additional errors in the solution.

H_2O measurements are taken in the low pressure cell and above the McKenna flat flame burner to demonstrate the effectiveness of the method. The low pressure cell measurements demonstrate improved accuracy of up to 30% for the measured pressures within the measurement cell. The second derivative fitting method demonstrates a vast improvement over the typical fitting scheme for obtaining the pressure from spectral fitting. Traditionally, pressure is challenging to obtain in this manner, but with the second derivative fitting, the pressure can be accurately obtained, even in the presence of baseline errors, from a spectral fitting method.

The McKenna flat flame burner measurements demonstrate the introduction of errors in the inferred properties due to missing spectral broadening parameters. The methane/air flow exhaust contains a large percentage of collisional molecules that

are not listed in the HITRAN database. While the second derivative fitting scheme accurately matches the spectral profile, the inferred fluid flow properties are poorly fit to the expected data, with approximately a 15% discrepancy between the expected temperature and the average of the inferred temperatures. This represents a major drawback of this fitting scheme, as with any fitting scheme reliant upon accurate spectral models: the database and model must be accurate in the flow regime observed.

This drawback of the missing database parameters can be overcome through the use of the Boltzmann plot method, which uses the integrated area of a spectral absorbance, rather than fitting a direct profile. Because the lineshape function, taken as the Voigt in this work, integrates to unity, the dependence on the spectral broadening parameters drops out of the solution. Two limiting factors of the Boltzmann Plot method are that it relies on having isolated spectra, and that the integrated area, relies on having accurate measurements. The Aggregate Boltzmann Plot method is aimed at correcting the first of these two factors, by re-deriving the Boltzmann Plot method using aggregate spectral quantities instead of isolated spectral quantities. The modified equations as well as sensitivity and error analysis are presented. This work demonstrates the trends of the Aggregate Boltzmann Plot method are similar to the traditional Boltzmann Plot method, resulting in little loss to sensitivities.

Demonstration measurements of H_2O are completed in the low pressure cell and above the McKenna flat flame burner. Good agreement is reached in the low pressure cell between the externally reference temperature and the inferred temperature from the method, demonstrating an uncertainty of less than 1%. Above the McKenna burner, the average of the inferred temperature of the cases is within 5% of the temperature measurements from previous literature [1] and from the Cantera simulation, demonstrating the value of the method when applied to aggregate spectra at high temperatures. It is noted that the standard deviation of the measurements is approximately 90 K, resulting from the low SNR of several of the tested transitions. The

ability of the method to measure blended spectral features allows for the Aggregate Boltzmann Plot to be effective in flow regimes where the Boltzmann Plot was previously limited to few absorption lines, where the interference from nearby transitions was limited. This makes the method useful in cases where the flow conditions vary in pressure and temperature. Though the application of aggregate clusters, as pressure broadening and high temperature line activation cause interference, the Aggregate Boltzmann Plot framework allows for these clusters to be used throughout the test case, where the typical Boltzmann Plot solution would fail. This represents a major extension of the Boltzmann Plot method, which allows for its application in regimes where it was previously challenging, if not impossible, to apply.

6.1.3 The Robust Combination Algorithm of the Second Derivative Fitting Method and the Aggregate Boltzmann Plot Method

In order to overcome the limitations in each of the second derivative fitting method and the Aggregate Boltzmann Plot Method, a robust algorithm is developed, which makes use of the baseline insensitivity and spectral line shape reconstruction accuracy of the second derivative fitting, and the insensitivity of the Aggregate Boltzmann Plot method to missing spectral database broadening parameters. This algorithm first applies the second derivative fitting method to the measured data, obtaining good fits to the data with high baseline insensitivity, but with poorly inferred flow properties. The accurate spectral shapes are then integrated and applied to the Aggregate Boltzmann Plot method, which integrates the reconstructed spectra resulting in insensitivity to the missing database parameters. The resulting novel methodology can be used to generate inferred measurements which are more accurate than both of the individual components of the methodology.

A set of measurement data above the McKenna flat flame burner is taken using a MEMS switch for time multiplexing, resulting in three transitions which are tested

through all three techniques: second derivative spectral fitting, the Aggregate Boltzmann Plot, and the combined measurement algorithm. The inferred flow properties from the combined data show marked improvement over the two individual methods. The pure second derivative fitting demonstrates an accuracy of 15% when comparing the average of the inferred temperatures with the expected temperatures from a 0.87 equivalence ratio methane-air flame. The pure Aggregate Boltzmann Plot method demonstrates a deviation of greater than 40% when comparing the reconstructed temperature to the expected temperature due to low SNR of the measurements. The combined method presents an averaged temperature of approximately 2150 K, within 6% of the expected temperatures from the experiment. This represents a significant benefit when using the two methods in the combined algorithm. It should be noted that for the aggregate lines chosen, the precision is lower in the Aggregate Boltzmann Plot method due to very low SNR of the lines measured. This adds in uncertainty to the inferred values, resulting in a lower precision. This can be improved through the application of the line selection algorithm discussed in order to better optimize the selected transitions.

6.2 Future Work

6.2.1 The LAC

Work remains to be done in to further the contributions of this work. For the LAC, the beamsteering effects must be mitigated. This method is currently viable only for stationary and laminar flows, where the density gradients are constant. Once the density gradients become variable, the LAC fails as an instrumentation technique. The next logical step would then be to apply the LA as a tomographic instrument, with high spatial and temporal resolution. This would allow for the simple acquisition of data, as well as very high accuracy due to the increased resolution of the pixels.

6.2.2 Second Derivative Fitting Method

The second derivative fitting method for baseline insensitivity, first and foremost, relies on accurate database parameters. In order to be full robust as an individual method, these parameters need to obtained. As in previous work, this can be done in the laboratory with the proper care and equipment, but to be easily and readily accessible, these databases must be properly populated. Sensitivity analysis to the missing parameters in various flow regimes could be a potential help to this segment of the work. Additionally, sensitivity analysis to the Savitsky-Golay parameters, such as the window size for the polynomial fitting and the polynomial order, need to be completed. These analyses will allow for higher accuracies to be obtained through the proper optimization of these parameters. Additionally, the error equation presented has currently been analyzed through computational integration of the terms in the equation. If an analogical form of these terms is obtained, the method would be more well defined, and could be applied to any regime and transition line without the need for the computational analysis.

6.2.3 The Aggregate Boltzmann Plot Method

The sensitivity and error analysis of the Aggregate Boltzmann Plot method needs to be expanded. The current analyses are completed for the introduction of errors and lines individually, rather than as a measure of composite error across many lines. By expanding this analysis in this way, better understanding of the sensitivities to errors in a system and the lines probed could be obtained. This would allow for better optimization of the line selection process as well as a better grasp of what the acceptable errors in the integrated areas are.

6.2.4 The combined Algorithm for the Second Derivative Fitting and the Aggregate Boltzmann Plot Methods

A full analysis of the propagation of errors through the systems needs to be completed to extend this contribution. This would allow for a better understanding of the capabilities of this method and the sensitivities to the different types of error that can be introduced through the baselines, missing database parameters, and integrated areas. The systems and lines chosen could, through this analysis, could be chosen to be better suited for various flow regimes and expected errors in the baselines.

Additionally, it would be of great interest to apply this method in a true practical flow such as the MRDE. This would give better insight into the applicability of the methods provided and where further gaps may need to be closed. An experiment such as this would more fully demonstrate the feasibility of the techniques discussed and would be an interesting extension of the work.

APPENDICES

APPENDIX A

LAC Characterization

The LAC was characterized to determine its sensitivity to noise and compare the measured values of the noise with those obtained from the manufacturer. The test setup for the characterization experiments consists of an integrating sphere, the LAC configuration with no focusing optics, and the TDL. The setup for this experiment is seen in Fig. A.1. The laser is tuned to a wavelength with no H2O absorption features, and passed into the integrating sphere. The sphere causes diffuse reflections of the laser beam, and, at the exit plane of the integrating sphere, outputs light of uniform power. The LAC collects this light and generates an image of snapshots of the uniform output light. Statistics are completed on this these snapshots to assess the noise characteristics of the camera. The LAC images acquired from using the TDL and the integrating sphere are seen below in Fig. A.2.

Statistical analysis was completed on images such as these for different gain settings for the camera and at different laser power outputs. The SNR for the different cases were determined through this experiment and plotted. Using the following equations, analytical solutions were obtained for the laser power output and theoretical SNR, which were then compared to the measured values.

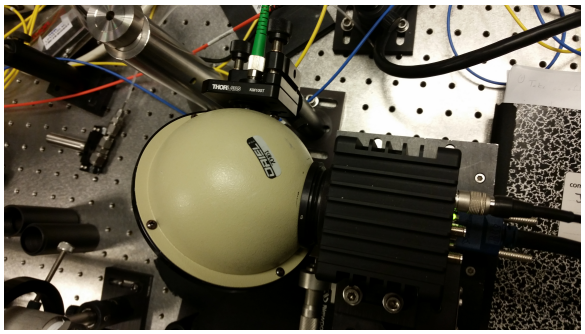

Figure A.1: Experimental setup of the integrating sphere.

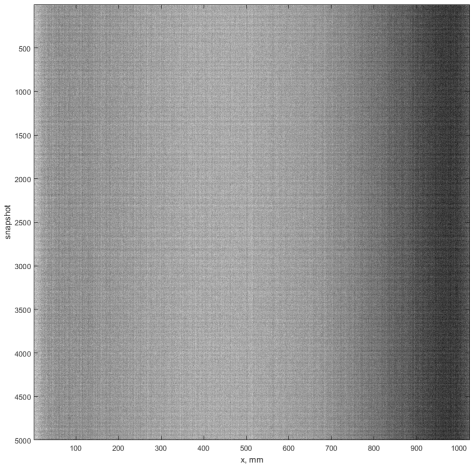

Figure A.2: Example image of a uniform power scan taken with the LAC using the integrating sphere and TDL.

$$\Psi = QE\frac{\lambda}{hc}A_pBP''\Delta t \tag{A.1}$$

$$SNR = \frac{\Psi/G}{QE\sqrt{\frac{QE\Psi}{G^2} + \sigma_{dark}^2 + \sigma_{ro}^2}} \tag{A.2}$$

In Eq. A.1, Ψ refers to the photoelectrons generated by the detector. The QE is the quantum efficiency of the detector, λ is the wavelength of the light, h is Planck's constant, and c is the speed of light. The area of the photodetector face is A_p, B is the pixel fill factor, P" is the power of the laser, and Δt is the acquisition time for the detector. The multiplication of these terms determines how many photoelectrons are generated for each integrated acquisition window.

The SNR of the measurement is obtained from Eq. A.2. Here the SNR refers to the signal-to-noise ratio, which determines how much of the measured data is usable signal, versus how much is noise in the system. This is obtained by dividing the ratio of the photoelectrons generated to the gain, G, by the quantum efficiency multiplied by the sqare root term. This term contains the shot noise, defined as $\frac{QE\Psi}{G^2}$, the dark noise inherent to the detector, and the read out noise.

Plotting both the experimental data and the analytical solutions, it becomes evident that the camera behaves well with respect to noise characteristics over a broad range of gain settings and laser powers in accordance with the manufacturers specifications.

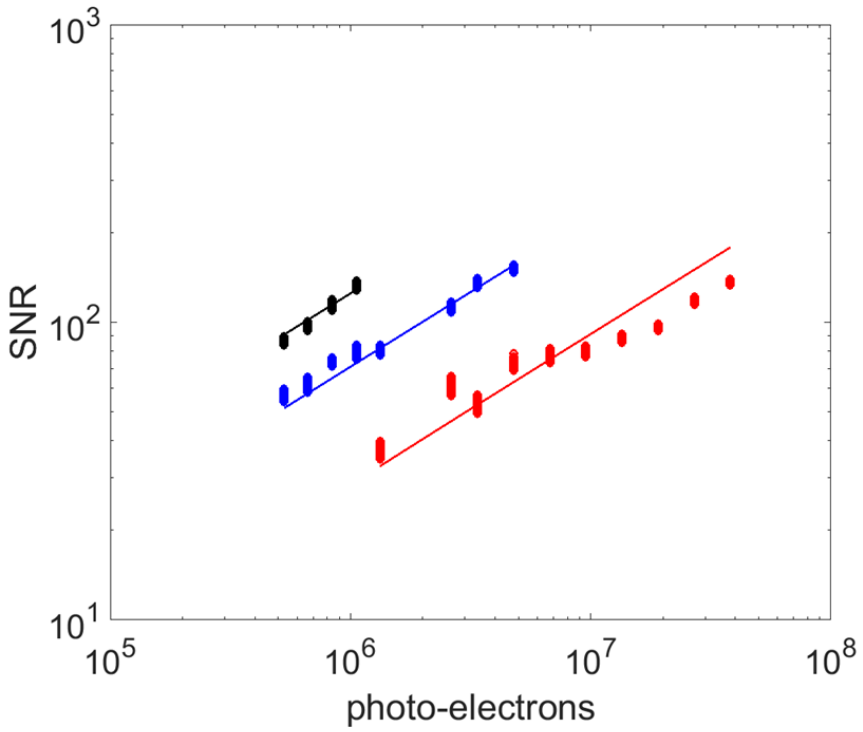

Figure A.3: Comparison plot over three gain settings of the LAC experimental SNR to laser power measurements with the analytical solution to the SNR equation. As can be seen, the measured SNR and the SNR obtained using the manufacturer's specifications are closely matched, thus the LAC behaves well.

APPENDIX B

Computational Calculations of the Second Derivative Fitting Algorithm with Representative Baseline Offset Errors

The error equation was used to simulate solutions over a wide variety of pressures and temperatures. Due to computation constraints, the solutions were determined through brute force calculations, iterating through a preset range of temperatures and pressures and arriving at a solution based on the value which generated the lowest error, rather than implementing an actual minimization scheme. This leads to errors dependent on the resolution of the flow properties iterated over, and is limited by the A line was chosen to observe, and a simulated measurement was created. Several different baseline error offsets were applied to the computed measurement cases and the terms of the error equation were iterated in order to determine the minimization point for the error equation using the built in function for MATLAB, *lsqnonlin*, a nonlinear optimization routine. These forced baseline errors were set up such that they mimicked the actual baseline errors seen in measurements, with small offsets and fitting errors included. This was completed through "fitting" a baseline to a dataset with nonzero wings, which induces a baseline offset error. These

RMS Offset error	T_r [K]	T_m [K]	% error	P_r [atm]	P_m [atm]	% error
0.0534	300	301	0.3	1	1.0177	1.77
0.2066	300	277	7.7	1	1.5	50
0.0534	2100	2158	2.7	2.2	3.3	50
0.2066	2100	1050	50	2.2	3.3	50

Table B.1: Direct fitting results for baselines which result in RMS errors seen in the first column generated by a baseline offset. Note that the bounds of the solution space probed by the MATLAB code would lead to a maximum error of 50%, meaning that the reconstructed values with errors of 50% are actually more erroneous than listed due to the analytical bounds.

RMS Offset Error	T_r [K]	T_m [K]	% error	P_r [atm]	P_m [atm]	% error
0.0534	300	300	0	1	1	0
0.2066	300	300	0	1	1	0
0.0534	2100	2099	0	2.2	2.2	0
0.2066	2100	2100	0	2.2	2.2	0

Table B.2: Second Derivative fitting results for baselines which result in RMS offset errors seen in the first column. In all offset cases and temperature and pressure combinations, the inferred temperature and pressure are alsmost exact.

were additionally exaggerated to observe how a worst case scenario baseline fit can affect the calculated properties using both the direct absorption fitting and the second derivative absorption fitting routines. Using the minimum point obtained from the optimization in MATLAB, the temperatures and pressures were obtained, and the errors between the minimized solutions and the exact property values were calculated. These are tabulated in Table B.1 and B.2. This algorithm is seen in Fig. B.1. It is immediately obvious that the second derivative reconstruction method performs better in the cases listed, which correspond to the plots given in Figs. B.2 and B.3. These simulated cases were performed with errors only being contributed from baseline offsets, not from background noise in the system, which would induce other errors in the reconstructed fluid properties. One of the benefits here, as described previously, is that the error equation is valid for any derivative of the absorbance, allowing for easy comparisons between the zeroth order derivative and the second order derivative methods.

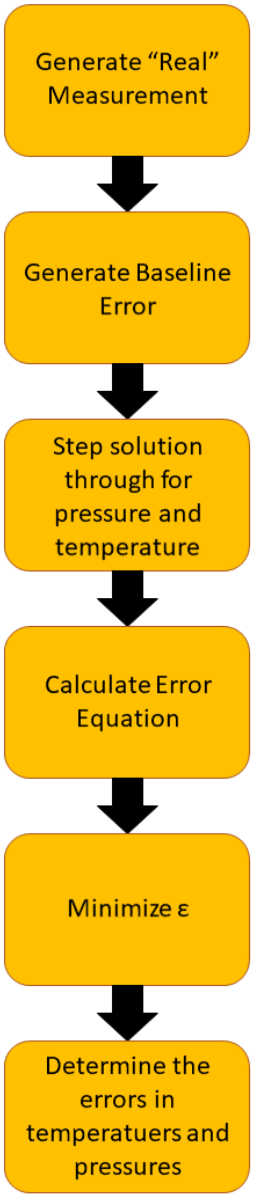

Figure B.1: Algorithm describing the method by which the acceptable errors in the baseline are determined computationally. The algorithm outputs errors in pressure and temperature based on the expected pressure and temperature and the expected baseline errors.

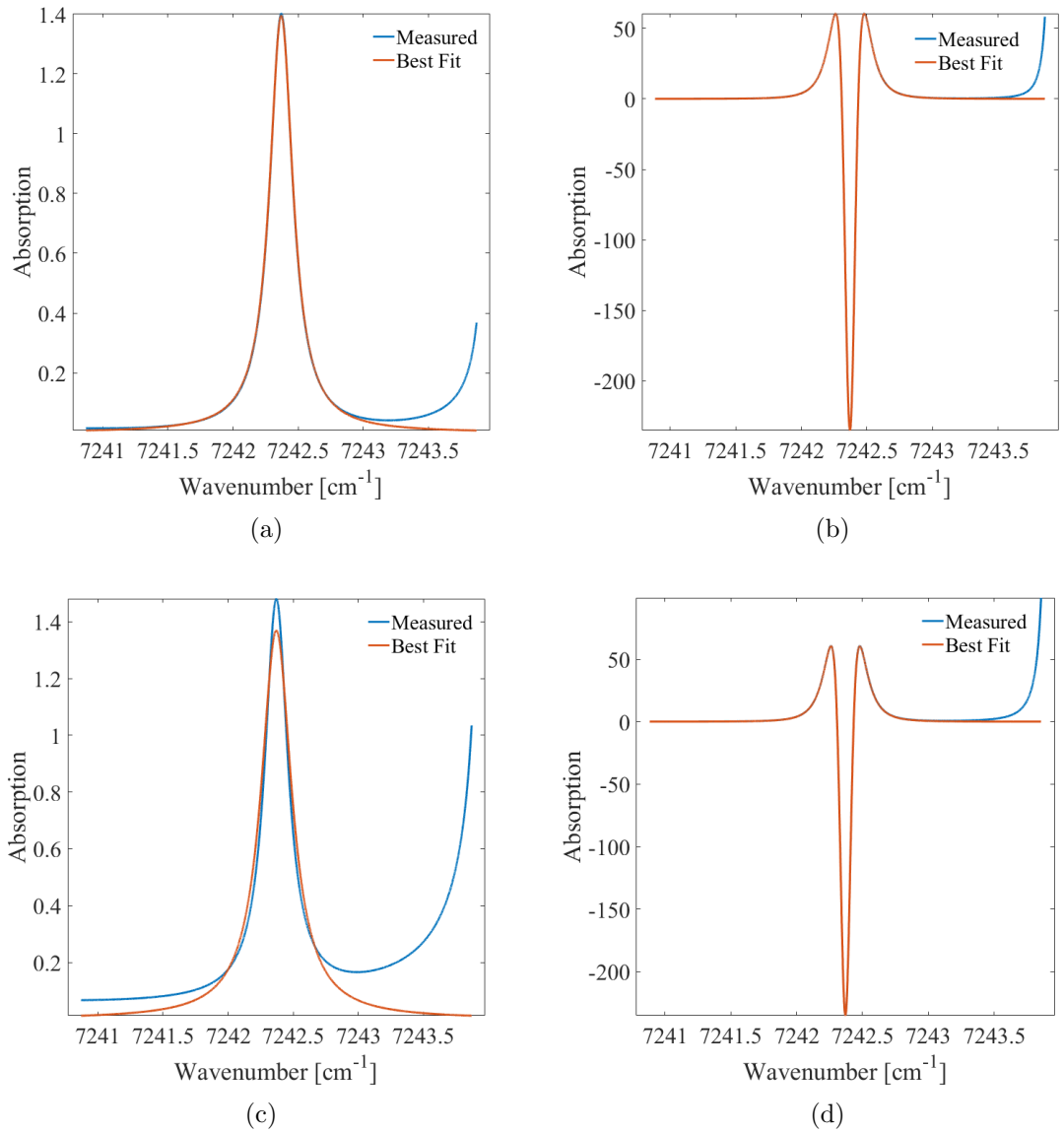

Figure B.2: Data simulated at 300 K and 1 atm for (a) the zeroth order derivative and (b) the second order derivative with RMS offset errors of 0.0534 and (c) the zeroth order derivative and (d) the second order derivative with RMS offset errors of 0.2066.

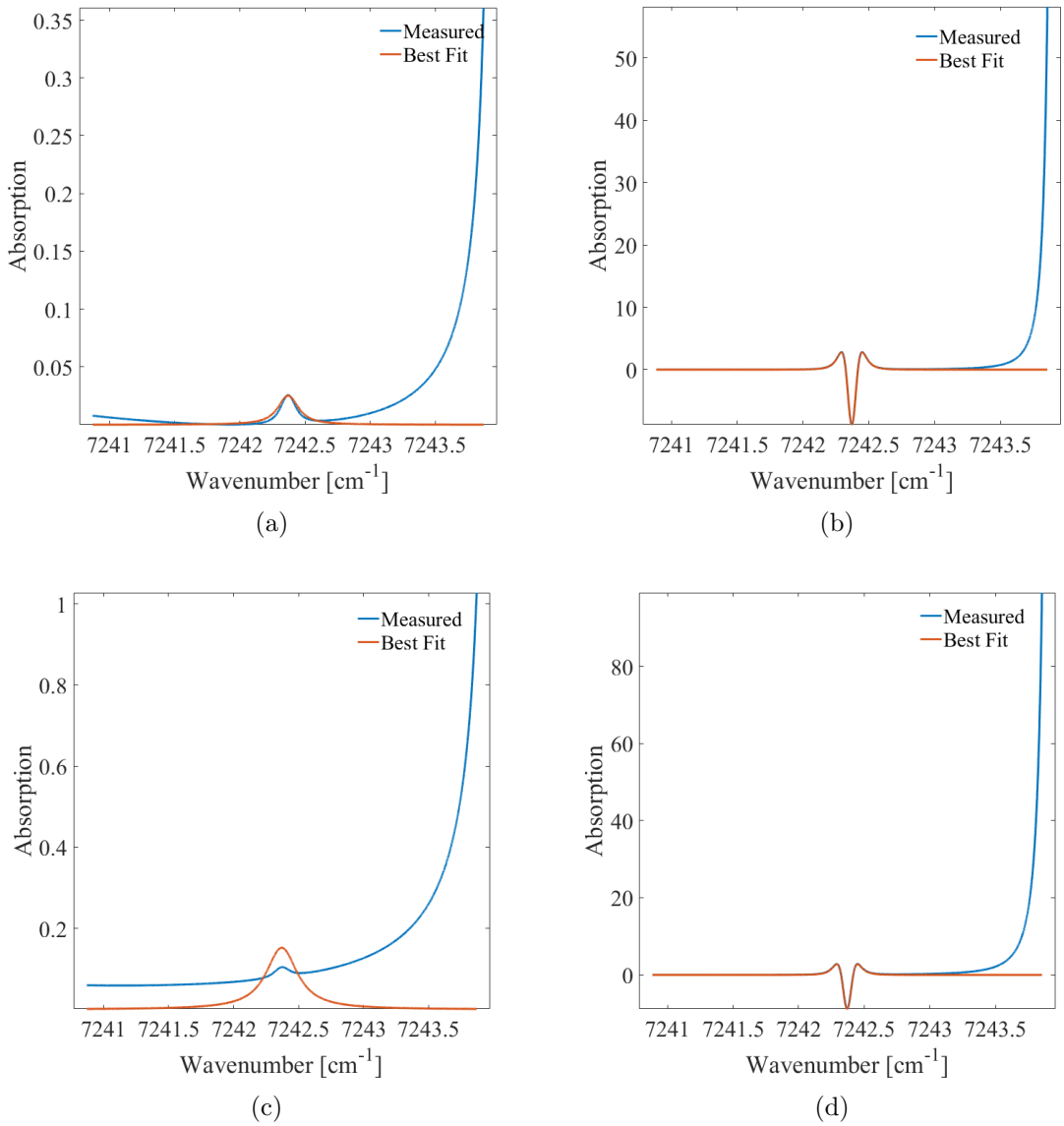

Figure B.3: Data simulated at 2100 K and 2.2 atm for (a) the zeroth order derivative and (b) the second order derivative with RMS offset errors of 0.0534 and (c) the zeroth order derivative and (d) the second order derivative with RMS offset errors of 0.2066.

The offsets were taken to demonstrate the effectiveness of the second derivative method at reconstructing the properties, even in measurements with high offset errors. Experimental measurements performed during the course of this work had baseline offset errors of far less than those listed here. Even in the presence of the much larger offset errors, the second derivative method performed excellently, faithfully inferring accurate temperature and pressure measurements.

BIBLIOGRAPHY

BIBLIOGRAPHY

[1] Logan White and Mirko Gamba. Journal of Quantitative Spectroscopy & Radiative Transfer Underresolved absorption spectroscopy of OH radicals in flames using broadband UV LEDs. *Journal of Quantitative Spectroscopy and Radiative Transfer*, 209:73–90, 2018.

[2] H Richard and M Raffel. Principle and applications of the background oriented schlieren (BOS). *MEASUREMENT SCIENCE AND TECHNOLOGY*, 2001.

[3] R J Adrian. Twenty years of particle image velocimetry. *Experiments in Fluids*, 39:159–169, 2005.

[4] Ronaid K Hanson, Jerry M Seitzman, and Phillip H Paul. Planar Laser-Fluorescence Imaging of Combustion Gases. *Applied Physics B*, 1990.

[5] Noel T. Clemens. *Flow Imaging*. John Wiley & Sons, 2002.

[6] J TROLINGER, M AZZAZY, D MODARRESS, and J CRAIG. Laser Diagnostic Methods/A Summary. *16th Fluid and Plasmadynamics Conference*, C:15–32, 1983.

[7] Makoto Matsui and Kimiya Komurasaki. Laser Absorption Spectroscopy in High Enthalpy Flows. In *38th AIAA Thermophysics Conference*, Toronto, Ontario Canada AIAA, 2005.

[8] Xiang Liu, Jay B. Jeffries, and Ronald K. Hanson. Measurement of Nonuniform Temperature Distributions Using Line-of-Sight Absorption Spectroscopy. *AIAA Journal*, 45(2):411–419, 2007.

[9] Xing Chao, Jay B. Jeffries, and Ronald K. Hanson. Development of laser absorption techniques for real-time, in-situ dual-species monitoring (NO/NH3, CO/O2) in combustion exhaust. *Proceedings of the Combustion Institute*, 34(2):3583–3592, 2013.

[10] Kristin M Busa, Michael S Brown, Mark R Gruber, and Jacob J France. Common-Path Measurement of H2O, CO, and CO2 via TDLAS for Combustion Progress in a Hydrocarbon-Fueled Scramjet. In *AIAA SciTech*, San Diego, California, 2016.

[11] Hira Nasim and Yasir Jamil. Optics & Laser Technology Diode lasers : From laboratory to industry. *Optics and Laser Technology*, 56:211–222, 2014.

[12] M G Allen. Diode laser absorption sensors for gas-dynamic and combustion flows. *Measurement science & technology*, 9:545–562, 1998.

[13] Chang Liu and Lijun Xu. Laser absorption spectroscopy for combustion diagnosis in reactive flows : A review. *Applied Spectroscopy Reviews ISSN:*, 2018.

[14] L. S. Rothman, I. E. Gordon, Y. Babikov, A. Barbe, D. Chris Benner, P. F. Bernath, M. Birk, L. Bizzocchi, V. Boudon, L. R. Brown, A. Campargue, K. Chance, E. A. Cohen, L. H. Coudert, V. M. Devi, B. J. Drouin, A. Fayt, J. M. Flaud, R. R. Gamache, J. J. Harrison, J. M. Hartmann, C. Hill, J. T. Hodges, D. Jacquemart, A. Jolly, J. Lamouroux, R. J. Le Roy, G. Li, D. A. Long, O. M. Lyulin, C. J. Mackie, S. T. Massie, S. Mikhailenko, H. S P Müller, O. V. Naumenko, A. V. Nikitin, J. Orphal, V. Perevalov, A. Perrin, E. R. Polovtseva, C. Richard, M. A H Smith, E. Starikova, K. Sung, S. Tashkun, J. Tennyson, G. C. Toon, Vl G. Tyuterev, and G. Wagner. The HITRAN2012 molecular spectroscopic database. *Journal of Quantitative Spectroscopy and Radiative Transfer*, 130:4–50, 2013.

[15] Bernard L Upschulte and Mark G Allen. DIODE LASER MEASUREMENTS OF LINE STRENGTHS AND SELF-BROADENING PARAMETERS OF WATER VAPOR BETWEEN 300 AND 1000 K NEAR 1 . 31 um. *J. Quant. Spectrosc. Radiat. Transfer*, 59(6), 1998.

[16] P Kauranen and V G Avetisov. Determination of absorption line parameters using two-tone frequency-modulation spectroscopy with diode lasers. *Optics Communications*, 106, 1994.

[17] Corinne Delaye, Jean-michel Hartmann, and Jean Taine. Calculated tabulations of H20 line broadening by H2 0, N2, 02, and CO2 at high temperature. *Applied optics*, 28(23), 1989.

[18] R.R. Gamache, J.-M. Hartmann, and L. Rosenbaum. Collisional Broadening of Water Vapor Lines - I. A survey of Experimental Results. *J. Quant. Spectrosc. Radiat. Transfer*, 52, 1994.

[19] Kendra L Letchworth and D. Chris Benner. Rapid and accurate calculation of the Voigt function. *J. Quant. Spectrosc. Radiat. Transfer*, 107:173–192, 2007.

[20] Joseph H Pierluissi, Peter C Vanderwood, and Richard B Gomez. FAST CALCULATIONAL ALGORITHM FOR THE VOIGT PROFILE. *J. Quant. Spectrosc. Radiat. Transfer*, 18(2):1–4, 1977.

[21] J. Humlicek. Optimized computation of the voigt and complex probability functions. *J. Quant. Spectrosc. Radiat. Transfer*, 27(4):437–444, 1982.

[22] S.R. Drayson. Rapid computation of the voigt profile. *J. Quant. Spectrosc. Radiat. Transfer*, 16, 1976.

[23] J.A.C Weideman. COMPUTATION OF THE COMPLEX ERROR FUNCTION. *SIAM J. NUMER. ANAL.*, 31(5), 1994.

[24] William J Thompson. NUMEROUS NEAT ALGORITHMS FOR THE VOIGT PROFILE FUNCTION. *Computers in Physics*, 7(6), 1993.

[25] Franz Schreier. Optimized implementations of rational approximations for the Voigt and complex error function. *Journal of Quantitative Spectroscopy and Radiative Transfer*, 112(6):1010–1025, 2011.

[26] C.P. Wang. Laser Doppler Velocimetry. *J. Quant. Spectrsc. Radint. Transfer*, 40(3):309–319, 1988.

[27] Michael F Miller, William J Kessler, and Mark G Allen. Diode laser-based air mass flux sensor for subsonic aeropropulsion inlets. *Applied Optics*, 35(24), 1996.

[28] Louis C Philippe and Ronald K Hanson. Laser-absorption mass flux sensor for high-speed airflows. *Optics Letters*, 16(24), 1991.

[29] Robert R Gamache, Richard Lynch, and Stephen P Neshyba. NEW DEVELOPMENTS IN THE THEORY OF PRESSURE- BROADENING AND PRESSURE-SHIFTING OF SPECTRAL LINES OF H20 : THE COMPLEX ROBERT-BONAMY FORMALISM. *J. Quant. Spectrosc. Radiat. Transfer*, 59:319–335, 1998.

[30] Venu Nagali and Ronald K Hanson. Design of a diode-laser sensor to monitor water vapor in high-pressure combustion gases. *Applied optics*, 36(36), 1997.

[31] D S Baer, V Nagali, R K Hanson, and M E Newfield. Scanned- and Fixed-Wavelength Absorption Diagnostics for Combustion Measurements Using Multiplexed Diode Lasers. *AIAA Journal*, 34(3), 1996.

[32] Scott T Sanders, Jeffrey A Baldwin, Thomas P Jenkins, Douglas S Baer, and Ronald K Hanson. DIODE-LASER SENSOR FOR MONITORING MULTIPLE COMBUSTION PARAMETERS IN PULSE DETONATION ENGINES. In *Proceedings of the Combustion Institute*, volume 28, pages 587–594, 2000.

[33] Mack S Brittelle, Jean M Simms, Scott T Sanders, James R Gord, and Sukesh Roy. Fixed-wavelength H 2 O absorption spectroscopy system enhanced by an on-board external-cavity diode laser. *Meas. Sci. Technol.*, 27, 2016.

[34] M P Arroyo and R K Hanson. Absorption measurements of water-vapor concentration, temperature, and line-shape parameters using a tunable InGaAsP diode laser. *Applied optics*, 32(30):6104–6116, 1993.

[35] M P Arroyo, S Langlois, and R K Hanson. Diode-laser absorption technique for simultaneous measurements of multiple gasdynamic parameters in high-speed flows containing water vapor. *Applied optics*, 33(15):3296–307, 1994.

[36] Ian A. Schultz, Christopher S. Goldenstein, R. Mitchell Spearrin, Jay B. Jeffries, Ronald K. Hanson, Robert D. Rockwell, and Christopher P. Goyne. Multispecies Midinfrared Absorption Measurements in a Hydrocarbon-Fueled Scramjet Combustor. *Journal of Propulsion and Power*, 30(6):1595–1604, 2014.

[37] Mark G Alien and William J Kessler. Simultaneous Water Vapor Concentration and Temperature Measurements Using 1 . 31- / xm Diode Lasers. *AIAA Journal*, 34(March):483–488, 1996.

[38] Christopher S Goldenstein, Ian a Schultz, Jay B Jeffries, and Ronald K Hanson. Two-color absorption spectroscopy strategy for measuring the column density and path average temperature of the absorbing species in nonuniform gases. *Applied optics*, 52(33):7950–62, 2013.

[39] R Mitchell Spearrin, Jay B Jeffries, and Ronald K Hanson. Mid-infrared Absorption Sensor for Measurements of CO and CO 2 in Propulsion Flows. In *52nd Aerospace Sciences Meeting*, 2014.

[40] B Scherer, H Hamid, M.L. Homer, and S. Forouhar. Laser spectroscopic gas analyzer for combustion product monitoring in spacecrafts. In *41st International Conference on Environmental Systems*, 2011.

[41] Fei Li, Xilong Yu, Weiwei Cai, and Lin Ma. Uncertainty in velocity measurement based on diode-laser absorption in nonuniform flows. *Applied Optics*, 51(20):4788, 2012.

[42] Andrew D Sappey, Bernard P Masterson, Qingchun Zhao, Eric Huelson, and Kenneth Barlow. TDLAS Measurements of Multiple Species and Temperature of Augmented Aeroengines. In *45th AIAA/ASME/SAE/ASEE Joint Propulsion Conference & Exhibit*, Denver, Co, 2009.

[43] Arthur T Giese and C Stacy French. THE ANALYSIS OF OVERLAPPING SPECTRAL ABSORPTION BANDS BY DERIVATIVE SPECTROPHOTOMETRY. *Applied Spectroscopy*, 9(2), 1955.

[44] W Snelleman, T C Rains, K W Yee, D Cook, and O Menis. Flame Emission Spectrometry with Repetitive Optical Scanning in the Derivative Mode. *ANALYTICAL CHEMISTRY*, 42(3), 1970.

[45] T C O'Haver and G L Green. Numerical Error Analysis of Derivative Spectrometry for the Quantitative Analysis of Mixtures. *Analytical Chemistry*, 48(2), 1976.

[46] Alan R Hawthorne and John H Thorngate. Improving analysis from second-derivative uv-absorption spectrometry. *Applied Optics*, 17(5), 1978.

[47] Mark L Olsen, David L Grieble, and Peter R Girffiths. Second Derivative Tunable Diode Laser Spectrometry for Line Profile Determination I . Theory. *Applied Spectroscopy*, 34(1), 1980.

[48] David L Grieble, Mark L Olson, and Peter R Griffiths. Second Derivative Tunable Diode Laser Spectrometry for Line Profile Determination. II. Experimental Results. *Applied Spectroscopy*, 34(1), 1980.

[49] Nicoletta Sinelli, Sara Limbo, Luisa Torri, Valentina Di, and Ernestina Casiraghi. Evaluation of freshness decay of minced beef stored in high-oxygen modi fi ed atmosphere packaged at different temperatures using NIR and MIR spectroscopy. *MESC*, 86(3):748–752, 2010.

[50] Ciro Balestrieri, Giovanni Colonna, Alfonso Giovane, Gaetano Irace, and Luigi Servillo. Second-Derivative Spectroscopy of Proteins A Method for the Quantitative Determination of Aromatic Amino Acids in Proteins. *Eur. J. Biochem.*, 440:433–440, 1978.

[51] T.C. O'Haver. Derivative and Wavelength Modulation Spectrometry. *ANALYTICAL CHEMISTRY*, 51(1), 1979.

[52] Michelle A Ferree, Robert D Shannon, Michelle A Ferree, and Robert D Shannon. TECHNICAL NOTE EVALUATION OF A SECOND DERIVATIVE UV / VISIBLE SPECTROSCOPY TECHNIQUE FOR NITRATE AND TOTAL NITROGEN ANALYSIS OF WASTEWATER SAMPLES. *Wat. Res.*, 35(1):1–6, 2001.

[53] William G. Crumpton, Thomas M. Isenhar, and Paul D. Mitchell. Nitrate and organic N analyses with second-derivative spectroscopy. *Limnology and Oceanography*, 37(4), 1992.

[54] Michael S. Brown, Dominic L. Barone, William F. Terry, Todd Barhorst, and Skip Williams. Accuracy , Precision , and Scatter in TDLAS Measurements. In *48th AIAA Aerospace Sciences Meeting Including the New Horizons Forum and Aerospace Exposition*, Orlando, Fl, 2010.

[55] Kristin M Busa and Michael S Brown. Measurements. In *54th AIAA Aerospace Sciences Meeting*, San Diego, Ca, 2016.

[56] Chadwick D. Lindstrom, Doug Davis, Skip Williams, and Chung-Jen Tam. Shock-Train Structure Resolved with Absorption Spectroscopy Part 1: System Design and Validation. *AIAA Journal*, 47(10):2379–2390, 2009.

[57] Chadwick D Lindstrom, Doug Davis, Skip Williams, and Chung-jen Tam. Shock-Train Structure Resolved with Absorption Spectroscopy Part 2: Analysis and CFD Comparison. *AIAA Journal*, 47(10), 2009.

[58] Andrew D Sappey, Pat Masterson, Jim Howell, Mike Estes, David Owenby, and Lee Sutherland. Tomographic Reconstruction of Multipath Tunable Diode Laser Spectroscopy Measurements in Turbine Engines. *Journal of Propulsion and Power*, 30(1):3–7, 2014.

[59] F U Khan, N U Rehman, S Naseer, M A Naveed, A Qayyum, N A D Khattak, and M Zakaullah. Diagnostic of 13.56 MHz RF sustained Ar-N2 plasma by optical emission spectroscopy. *THE EUROPEAN PHYSICAL JOURNAL APPLIED PHYSICS*, 11002, 2009.

[60] O Gabriel, S Stepanov, M Pfafferott, and J Meichsner. Time resolved measurements of the CF 2 rotational temperature in pulsed fluorocarbon rf plasmas. *PLASMA SOURCES SCIENCE AND TECHNOLOGY*, 15, 2006.

[61] Jurgen Ropcke, Detlef Loffhagen, Eric VonWahl, Andy C.S. Nave, Stephan Hamann, Jean-Piere H. van Helden, Norbert Lang, and Holger Kersten. On improved understanding of plasma-chemical processes in complex low-temperature plasmas. *THE EUROPEAN PHYSICAL JOURNAL D*, 2018.

[62] Edward C Rea and Ronald K Hanson. combustion. *Applied optics*, 27(21), 1988.

[63] Ronald K Hanson and Jay B Jeffries. Diode Laser Sensors for Ground Testing. In *25th AIAA Aerodynamic Measurement Technology and Ground Testing Conference 5 - 8 June 2006, San Francisco, California*, San Francisco, Ca, 2006.

[64] C. S. Goldenstein, I. A. Schultz, R. M. Spearrin, J. B. Jeffries, and R. K. Hanson. Scanned-wavelength-modulation spectroscopy near 2.5 μm for H2O and temperature in a hydrocarbon-fueled scramjet combustor. *Applied Physics B*, pages 1–11, 2014.

[65] Ian a. Schultz, Christopher S. Goldenstein, Jay B. Jeffries, Ronald K. Hanson, Robert D. Rockwell, and Christopher P. Goyne. Spatially-resolved TDLAS measurements of temperature, H 2 O column density, and velocity in a direct-connect scramjet combustor. In *52nd Aerospace Sciences Meeting*, National Harbor, Maryland, 2014.

[66] Christopher S Goldenstein, Christopher A Almodóvar, Jay B Jeffries, Ronald K Hanson, and Christopher M Brophy. High-bandwidth scanned-wavelength-modulation spectroscopy sensors for temperature and H2O in a rotating detonation engine. *Measurement Science and Technology*, 25(10):105104, 2014.

[67] G B Rieker, H Li, X Liu, J T C Liu, J B Jeffries, R K Hanson, M G Allen, S D Wehe, P A Mulhall, H S Kindle, A Kakuho, K R Sholes, T Matsuura, and S Takatani. Rapid measurements of temperature and H 2 O concentration in IC engines with a spark plug-mounted diode laser sensor. In *Proceedings of the Combustion Institute*, volume 31, pages 3041–3049, 2007.

[68] Hannes Fulge, Stefan Loehle, and Stefanos Fasoulas. Analysis of Wavelength Modulation Spectroscopy for Water Vapour Measurements in Supersonic Combustion. In *11th AIAA/ASME Joint Thermophysics and Heat Transfer Conference*, Atlanta, Ga, 2014.

[69] Andrew Sappey, David Owenby, P VanHoudt, J Hannam, Q Zhao, P McCormick, Bernard Masterson, Mike Estes, Lee Sutherland, Skip Williams, and T Barhorst. Flight-Ready TDLAS Combustion Sensor for Hypersonics. *16th AIAA/DLR/DGLR International Space Planes and Hypersonic Systems and Technologies Conference*, pages AIAA 2009–7234, 2009.

[70] Avishek Guha and Ingmar Schoegl. Tomographic laser absorption spectroscopy using Tikhonov regularization. *Applied optics*, 53(34):8095–8103, 2014.

[71] Andrew W Caswell. *Water Vapor Absorption Thermometry*. Dissertation, University of Wisconsin-Madison, 2009.

[72] B. J. Wheatley, T. J. McIntyre, and D.R. Buttsworth. Tunable Diode Laser Absorption Spectroscopy of Hypersonic Flows. In *19th Australasian Fluid Mechanics Conference*, 2014.

[73] S.D. Wehe, D.S. Baer, and R.K. Hanson. Tunable diode-laser absorption measurements of temperature, velocity, and H2O in hypervelocity flows. In *33rd Joint Propulsion Conference and Exhibit*, Seattle, Wa, 1997.

[74] Solon Karagiannopoulos, Edward Cheadle, Paul Wright, Stylianos Tsekenis, and Hugh Mccann. Multiwavelength diode-laser absorption spectroscopy using external intensity modulation by semiconductor optical amplifiers. *Applied optics*, 51(34):8057–8067, 2012.

[75] Chang Liu, Lijun Xu, Jianliang Chen, Zhang Cao, Yuzhen Lin, and Weiwei Cai. Development of a fan-beam TDLAS-based tomographic sensor for rapid imaging of temperature and gas concentration. *Optics Express*, 23(17):22494, 2015.

[76] O Witzel, A Klein, C Meffert, S Wagner, S Kaiser, C Schulz, and V Ebert. VCSEL-based, high-speed, in situ TDLAS for in-cylinder water vapor measurements in IC engines. *Optics Express*, 21(17), 2013.

[77] C S Goldenstein, R M Spearrin, I A Schultz, J B Jeffries, and R K Hanson. Wavelength-modulation spectroscopy near 1.4 um for measurements of H2O and temperature in high-pressure and -temperature gases. *Measurement Science and Technology*, 25(5):055101, 2014.

[78] A Farooq, J B Jeffries, and R K Hanson. Measurements of CO 2 concentration and temperature at high pressures using 1 f -normalized wavelength modulation spectroscopy with second harmonic detection near $2:7\ \mu$ m. *Applied optics*, 48(35), 2009.

[79] Kyle Owen and Aamir Farooq. A calibration-free ammonia breath sensor using a quantum cascade laser with WMS 2f / 1f. *Appl. Phys. B*, pages 371–383, 2014.

[80] Chunguang Li, Lei Dong, Chuantao Zheng, and Frank K Tittel. Compact TDLAS based optical sensor for ppb-level ethane detection by use of a 3.34 um

room-temperature CW interband cascade laser. *Sensors & Actuators: B. Chemical*, 232:188–194, 2016.

[81] G Durry, J.S. Li, I Vinogradov, A Titov, L Joly, J Cousin, T Decarpenterie, N Amarouche, X Liu, B Parvitte, O Krablev, M Gerasimov, and V Zeninari. Near infrared diode laser spectroscopy of C2H2, H2O, CO2 and their isotopologues and the application to TDLAS, a tunable diode laser spectrometer for the martian PHOBOS-GRUNT space mission. *Appl Phys B*, pages 339–351, 2010.

[82] Aamir Farooq, Jay B Jeffries, and Ronald K Hanson. In situ combustion measurements of H 2 O and temperature near 2 . 5 um using tunable diode laser absorption. *Meas. Sci. Technol.*, 2008.

[83] Kristin M. Busa, James C. McDaniel, Michael S. Brown, and Glenn S. Diskin. Implementation of Maximum-Likelihood Expectation-Maximization Algorithm for Tomographic Reconstruction of TDLAT Measurements. In *52nd Aerospace Sciences Meeting*, National Harbor, Maryland, 2014.

[84] James O Hornkohl, Christian Parigger, and J.W.L. Lewis. TEMPERATURE MEASUREMENTS FROM CN SPECTRA IN A LASER-INDUCED PLASMA. *J. Quant. Spectrosc. Radiat. Transfer*, 46(5):405–411, 1991.